Energy Calibration Method for the KOTO CsI Calorimeter

DISSERTATION
Presented in Partial Fulfilment of the Requirements
for the Degree of Doctor of Science
in the Graduate School of Osaka University

Lee Jong-won
Osaka University

Aug, 2014

Abstract

The KOTO experiment aims to observe the rare decay of long lived neutral kaons, $K_L \to \pi^0\nu\bar{\nu}$, with the sensitivity of the Standard Model prediction. The detectors of the KOTO experiment were constructed at J-PARC. The electromagnetic calorimeter is the only detector to measure energies and hit positions of gamma which are used for the $K_L \to \pi^0\nu\bar{\nu}$ event reconstruction.

To guarantee the performance of the calorimeter, an accurate output monitoring method and a precise energy calibration method are required. I built an output monitoring system using Laser light source, and determined its performance. For the calibration of the calorimeter, the calibration sources are limited to the cosmic ray events and K_L decay events, because there are no other detectors which can measure energy or momentum of particles independently. In addition, the KOTO experiment will run for several years, and thus the calibration has to be done simultaneously with the data taking to secure the reliabilities of data. Because of these restrictions, I developed and studied a new calibration method which uses $K_L \to 3\pi^0$ decay events and occasional absolute energy calibration runs. This method can calibrate the calorimeter with an accuracy less than 1%.

Acknowledgements

This thesis could no be completed without enormous support from many people. I would like to express my appreciation to them on this occasion. First of all, I would like to express my heartfelt gratitude to my supervisor, Prof. Taku Yamanaka, for giving me a great opportunity for the research in high energy physics. He always shows me the attitude and the mindset of researchers by himself. His those words and deeds impressed me deeply. I cannot express all of my gratitudes enough for giving me a lot of support and advice.

I would like to extend my gratitudes to all of the KOTO collaborators. When I joined the KOTO experiment, no detectors for the experiment were prepared; the calorimeter was in FNAL; and there was only a proposal. I was deeply impressed that the proposal became the detector with their enormous efforts and intentions even though there were many obstacles. I had worked on the calorimeter construction and the development of the calibration method of the KOTO experiment. I would like to extend my gratitudes to Prof. N. Sasao, Prof. J. Comport, Prof. T. Inagaki, Prof. S. Suzuki, Prof, M. Cambell, Prof. Y. W. Wah, Prof. T. Shinkawa, Prof. T. Komatsubara, Prof. G. Y. Lim, Prof, T. Nomura, Prof. Tajima, Prof. H. Nanjo, Prof. H. Watanabe and Prof. T. Matsumura for giving me invaluable supports and advices on analysis. I also want to express sincere gratitude to Prof. N. Nguyen for his advices about Laser system.

I am deeply thankful to Prof. M. Togawa, and Dr. Y. Ri. They led the calorimeter construction at the J-PARC. Without them, the calorimeter cannot be built with such a completeness. I am also grateful to Dr. E. Iwai, T. Shimogawa, Mr. K. Sato and Dr. K. Shiomi for their instructions and advices on the analysis. I would like to thank Dr. T. Masuda, Mr. H. Yoshimoto, Mr, N. Kawasaki, Mr, Y. Maeda, Mr. D. Naito, Mrs. R. Murayama, Ms. Y. Yanagida, Mr. Y. Nakaya, Mr. Y. Sugiyama, and Mr. S. Banno for their great works on the calorimeter construction and the beam test.

I also would like thank all of members of the Yamanaka group at Osaka University. I want to express hearty gratitude to Prof. K. Hanagaki for his advices. I owe special thanks to Dr. H. Hirose for his kindness and friendship. I would like to express my gratitude to Mr. T. Takagi, Mr. W. Oakamura, Mr. J. Uchida, Mr. M. Endo, Mr. J. J. Teoh, Mr. S. Higashino, N. Ishijima, Y. Takashima, Mr. R. Tsuji, Mr. Y. Arai. Ms. M. Isoe, for their kindness and harmonious relationships. I am deeply thankful to the secretaries of the group, Ms. M. Kawaguchi, Ms. A. Kamei, and Mrs. K. Kawahara for their help. I want to express my appreciation to the collaborators once again.

Finally, I would like to express my appreciation to my parents, Lee Byoung-hwa, and Kim Sun-jin for their supports, endurance, and trust.

I remember what I said in the graduation ceremony of the Japanese language course in the Osaka University (2003.3). I said, "In the future, I may hang on the way or wander, but I will advance towards the goal steadly". It became true.

Lee Jong-won

Gimhae, R.O.Korea.
July 2014.

Contents

List of Figures

List of Tables

Chapter 1

Introduction

1.1 CP Violation

1.1.1 CP Violation

A broken symmetry between matter and antimatter, CP Violation, is one of the important subjects in particle physics. In Quantum Field Theory (QFT), there are three fundamental symmetries, charge conjugation (C), parity (P) and Time reversal (T). However, the CP-symmetry, the combination of the C and P symmetries, is broken. It is confirmed by cosmological observations, and results of particles physics experiments, as described bellow.

The amounts of matter and antimatter were balanced in the early Universe, but the current Universe is matter dominant with few anti-matter. The ratio of broken symmetry between matter and antimatter can be expressed by the baryon-to-entropy ratio, the ratio between the net number of baryons and the number of gammas, $(n_B - n_{\bar{B}})/n_\gamma$. The current value of the ratio was derived from the cosmic microwave background measurements, and the value is $\sim 10^{-10}$ [1]. To explain why the ratio is not zero, baryogenesis which assumes different production ratio between baryons and antibaryons is needed. A.D. Sakharov proposed following three fundamental conditions:

- baryon number violation,
- loss of thermal equilibrium, and
- C violation and CP violation

for the baryogenesis, known as "Sakharov Conditions" [2].

Of those conditions, the CP violation is observed in weak interactions in particle physics. The CP violating decay was first observed by V.Fitch and J. Cornin *et al.* [3]. They observed that the CP odd state particle, K_L, decayed into two charged pions which are in a CP even state. Currently, it is known that CP violation occurs via a nonzero imaginary phase in the CKM matrix which describes amplitudes in flavor changes of quarks in the standard model. The standard model has 3 types of interactions, electromagnetic, weak, and strong nuclear interaction. Only weak interaction violates CP in the standard model. The estimated baryon-to-entropy ratio from the standard model physics is $\sim 10^{-20}$, and it is largely different from the cosmological observations. To explain this difference, new physics beyond the standard model is required.

1.1.2 CKM matrix

There are six kinds of quarks, up, down, strange, charm, top and bottom. They can be classified by three generations and two types of charges. Currently, we know that the flavor of quarks can change to other types via weak interaction in the standard model physics. The interaction amplitudes between different generations are suppressed. The CKM matrix expresses the interaction amplitudes between different flavors of quarks. From a unitarity requirement, there are four degrees of freedom in the matrix components. They are expressed with three real angles, θ_{12}, θ_{13}, θ_{23}, and one imaginary phase, δ_{13}. The CKM matrix can be written as

$$V = \begin{pmatrix} V_{ud} & V_{us} & V_{ub} \\ V_{cd} & V_{cs} & V_{cb} \\ V_{td} & V_{ts} & V_{tb} \end{pmatrix} = \begin{pmatrix} c_{12}c_{13} & s_{12}c_{13} & s_{13}e^{-i\delta_{13}} \\ -s_{12}c_{23} - c_{12}s_{23}s_{13}e^{i\delta_{13}} & c_{12}c_{23} - s_{12}s_{23}s_{13}e^{i\delta_{13}} & s_{23}c_{13} \\ s_{12}s_{23} - c_{12}c_{23}s_{13}e^{i\delta_{13}} & -c_{12}s_{23} - s_{12}c_{23}s_{13}e^{i\delta_{13}} & c_{23}c_{13} \end{pmatrix}, \tag{1.1}$$

where $c_{ij} = \cos\theta_{ij}$, and $s_{ij} = \sin\theta_{ij}$. L.Wolfenstein parameterised the matrix [4] by setting $\lambda = s_{12}$, $A\lambda^2 = s_{23}$, $A\lambda^3(\rho - i\eta) = s_{13}e^{i\delta}$, as:

$$V = \begin{pmatrix} 1 - \frac{\lambda^2}{2} & \lambda & A\lambda^3(\rho - i\eta) \\ -\lambda & 1 - \lambda^2/2 & A\lambda^2 \\ A\lambda^3(1 - \rho - i\eta) & -A\lambda^2 & 1 \end{pmatrix} + \mathcal{O}(\lambda^4). \tag{1.2}$$

The unitarity of the CKM matrix requires $V_{ud}V_{ub}^* + V_{cd}V_{cb}^* + V_{td}V_{tb}^* = 0$. This condition makes a triangle on the $\rho - \eta$ plane. This triangle, known as "Unitarity triangle", is used to represent the CKM matrix components. The currently known values of ρ and η are 0.121 ± 0.02 and 0.349 ± 0.012, respectively [5].

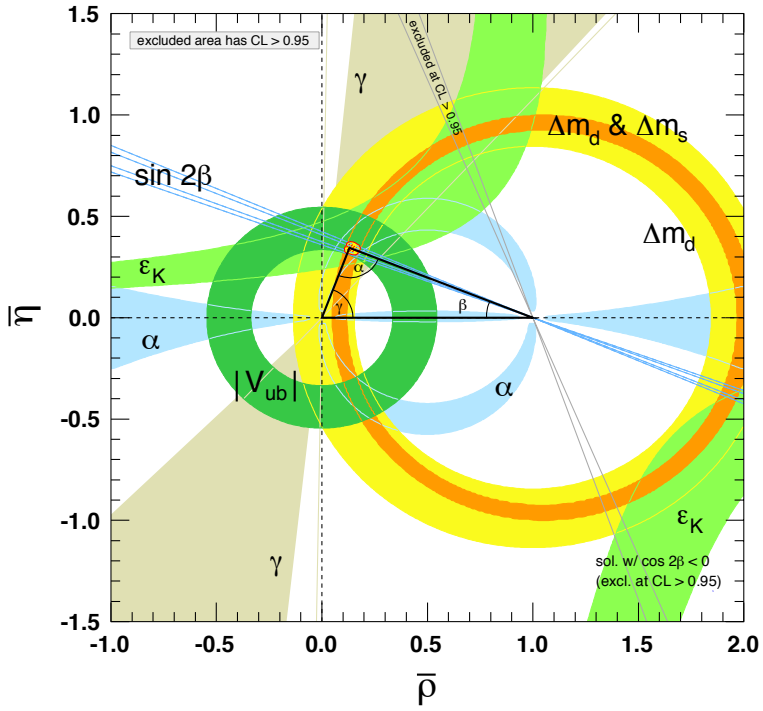

Figure 1.1: Current CKM unitarity triangle [5]

CP violation in particle interactions occurs by the nonzero imaginary component, δ_{13} or η. It, however, cannot explain the amount of matter in the Universe as mentioned.

If a new physics exists, it may affect the branching ratio of particles. In case of suppressed decay modes in the standard model, the branching ratio can be large enough to be detected by experiments. Therefore, the KOTO experiment aims to detect the $K_L \to \pi^0\nu\bar{\nu}$ decay event, one of rare decay modes of K_L, to search for such new physics.

1.1.3 $K_L \to \pi^0\nu\bar{\nu}$ decay

The $K_L \to \pi^0\nu\bar{\nu}$ decay mode has three characteristics.

- The branching ratio is suppressed in the Standard Model.
- The branching ratio can be largely changed by new physics.
- The branching ratio is proportional to the square of CP violation parameter η, and has small theoretical ambiguity.

Properties of K_L particle

The K_L particle is one of states of neutral kaons. There are two mass eigenstates of neutral kaon, $|K_L\rangle$ and $|K_S\rangle$. They are mixed states of $|K^0\rangle$ and $|\bar{K_0}\rangle$ which consist of d-quark and s-quark. CP eigen states, *i.e.* a CP-odd state and a CP-even state, of neutral kaon are written as

$$|K_1\rangle = \frac{1}{\sqrt{2}}(|K_0\rangle + |\bar{K_0}\rangle), \mathrm{CP-even\ state} \tag{1.3}$$

$$|K_2\rangle = \frac{1}{\sqrt{2}}(|K_0\rangle - |\bar{K_0}\rangle), \mathrm{CP-odd\ state.} \tag{1.4}$$

The $|K_L\rangle$ and $|K_S\rangle$ can be written with $|K_1\rangle$ and $|K_2\rangle$ as,

$$|K_L\rangle = \frac{1}{\sqrt{1+|\bar{\epsilon}|^2}}(|K_2\rangle + \bar{\epsilon}|K_1\rangle) \tag{1.5}$$

$$|K_S\rangle = \frac{1}{\sqrt{1+|\bar{\epsilon}|^2}}(|K_1\rangle + \bar{\epsilon}|K_2\rangle). \tag{1.6}$$

The $|\bar{\epsilon}|$ indicates the CP asymmetry component of neutral kaons. If CP symmetry is conserved, the $|\bar{\epsilon}|$ must be zero, but the current value of $|\bar{\epsilon}|$ is $(2.2228 \pm 0.011) \times 10^{-3}$ [5]. It means that K_L is a mixed-CP state dominated by a CP-odd state, but has a small component of a CP-even state.

This characteristic makes that K_L decays generally into CP-odd states. Decaying into CP-even states is suppressed as marked as [CPV] in Table 1.1. This makes that K_L decays mainly into a 3π state, and K_S decays mainly into a 2π state. This feature causes large difference in lifetime between K_L (5.116×10^{-8} sec) and K_S (0.8954×10^{-10} sec) [5].

$K_L \to \pi^0\nu\bar{\nu}$ decays in the Standard Model

In the standard model physics, the $K_L \to \pi^0\nu\bar{\nu}$ decay mode occurs via a Z-penguin diagram and a W-box diagram which are shown in Fig. 1.2. These diagrams are highly suppressed by the GIM mechanism. The state of neutral kaon, $|K^0\rangle$, consists of strange quark and anti-bottom quark. Therefore, the $K_L \to \pi^0\nu\bar{\nu}$ decay diagram contains flavor changes $s \to X \to d$

Table 1.1: Decay modes of K_L [5]

Decay mode	branching ratio(Γ_i/Γ)
$\pi^{\pm}e^{\mp}\nu_e$ $[K^0_{e3}]$	$(40.55 \pm 0.11)\%$
$\pi^{\pm}\mu^{\mp}\nu_\mu$ $[K^0_{\mu 3}]$	$(27.04 \pm 0.07)\%$
$\pi^+\pi^-\pi^0$	$(12.54 \pm 0.05)\%$
$\pi^+\pi^-$[CPV]	$(1.967 \pm 0.010) \times 10^{-3}$
$3\pi^0$	$(19.52 \pm 0.12)\%$
$2\pi^0$[CPV]	$(8.64 \pm 0.06) \times 10^{-4}$
2γ	$(5.47 \pm 0.04) \times 10^{-4}$
$\pi^0\nu\bar{\nu}$	$< 2.6 \times 10^{-8}$ (90%CL)

$(X = u, c, t)$, and $\bar{s} \to X \to \bar{d}$ $(X = \bar{u}, \bar{c}, \bar{t})$. Each quark has a different contribution on the $K_L \to \pi^0\nu\bar{\nu}$ decay amplitude,

$$A(s \to d\nu\bar{\nu}) = \sum_{q=u,c,t} V^*_{qs}V_{qd}A_q \begin{cases} \mathcal{O}(\lambda^5 m_t^2) + i\mathcal{O}(\lambda^5 m_t^2)|_{q=t} \\ \mathcal{O}(\lambda m_c^2) + i\mathcal{O}(\lambda^5 m_c^2)|_{q=c} \\ \mathcal{O}(\lambda\Lambda^2_{QCD})|_{q=u} \end{cases} \tag{1.7}$$

The decay amplitude of $K_L \to \pi^0\nu\bar{\nu}$ decay mode is the sum of contributions from $K^0 \to \pi^0\nu\bar{\nu}$ and $\bar{K^0} \to \pi^0\nu\bar{\nu}$. A contribution from a real part of amplitude is canceled, and only an imaginary part component contributes to the $K_L \to \pi^0\nu\bar{\nu}$ decay. Because the mass of the top quark is 100 times larger than the charm quark mass, $K_L \to \pi^0\nu\bar{\nu}$ decay mode is dominated by imaginary component of top quark mediated diagram.

The branching ratio of $K_L \to \pi^0\nu\bar{\nu}$ decay is written as

$$BR(K_L \to \pi^0\nu\bar{\nu}) = \kappa_L \left(\frac{Im\lambda_t}{\lambda^5}X_t\right)^2, \tag{1.8}$$

where $\kappa_L = (2.231 \pm 0.013) \times 10^{-10} \left[\frac{\lambda}{0.2248}\right]^8$ and $X_t = 1.469 \pm 0.017 \pm 0.002$. The $Im\lambda_t$ is proportional to the η of CKM matrix as shown in Eq. 1.8. The theoretical calculation result of this branching ratio is BR($K_L \to \pi^0\nu\bar{\nu}$)= $(2.43^{+0.40}_{-0.37} \pm 0.06) \times 10^{-11}$ [6].

If the measured branching ratio of $K_L \to \pi^0\nu\bar{\nu}$ decay is inconsistent with the branching ratio which is predicted from the η derived from B meson decays, it means that the $K_L \to \pi^0\nu\bar{\nu}$ decay mode is affected by the new physics.

New physics in the $K \to \pi\nu\bar{\nu}$ decay

The $K_L \to \pi^0\nu\bar{\nu}$ decay mode and its iso-symmetrical partner, the $K^+ \to \pi^+\nu\bar{\nu}$ decay mode, are sensitive to new physics by their small theoretical ambiguities and their small branching ratios. The branching ratio of $K \to \pi\nu\bar{\nu}$ decay is sensitive to all diagrams from new physics, and the branching ratio of the $K_L \to \pi^0\nu\bar{\nu}$ decay is sensitive to CP violating decay diagrams. With this feature, the ratio of two branching ratios changes by new physics models [9] as shown in Fig. 1.3.

In case of SM4 which assumes four generations of quarks, there can be two other imaginary phases in its extended CKM matrix. The model predicts that the branching ratio of the $K_L \to \pi^0\nu\bar{\nu}$ decay to be in the green area shown in Fig. 1.3. In case of MFV, Minimal Flavor Violation, which assumes no CP violation in new physics, the contribution of the new physics to both branching ratios is given by a function of new physics effect. Therefore the branching ratios have a clean correlation as shown in an orange line in Fig. 1.3.

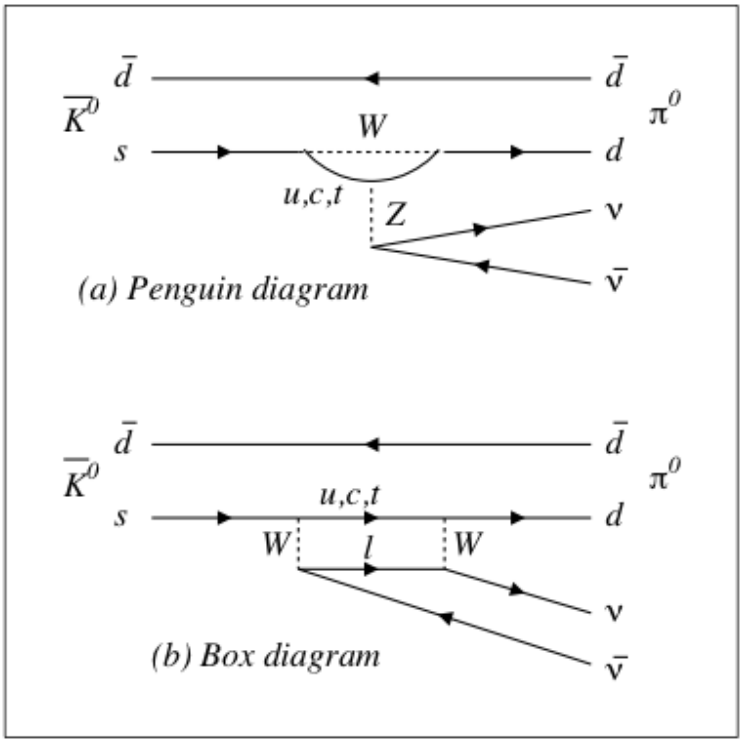

Figure 1.2: Feynman diagrams of $K_L \to \pi^0\nu\bar{\nu}$ decay

1.1.4 History of $K_L \to \pi^0\nu\bar{\nu}$ branching ratio measurement

An upper limit on the branching ratio of the $K_L \to \pi^0\nu\bar{\nu}$ decay mode is $< 2.6 \times 10^{-8}$ (90% CL) [8] as set by KEK E391a experiment. The branching ratio of $K^+ \to \pi^+\nu\bar{\nu}$ was measured to be $(1.7^{+1.15}_{-1.05}) \times 10^{-10}$ [10], and it gives an upper limit on the $K_L \to \pi^0\nu\bar{\nu}$ branching ratio, 1.46×10^{-9} [7], which is called the Grosman-Nir bound. The history of $K_L \to \pi^0\nu\bar{\nu}$ branching ratio is shown in Fig. 1.4.

1.2 Concept of the KOTO experiment

The KOTO experiment aims to search for $K_L \to \pi^0\nu\bar{\nu}$ decay event. In this section, I will explain the concept of the KOTO experiment.

The decay products of $K_L \to \pi^0\nu\bar{\nu}$ decay mode are all neutral particles. Two of them are gammas, which are decay products of π^0. They are detectable particles and their energy and hit position can be measured. The other two are neutrinos, and they cannot detected by the detector. The KOTO experiment uses information of only 2 gammas for the event reconstruction.

There are two types of background events for $K_L \to \pi^0\nu\bar{\nu}$ decay. One comes from beam line particles. Another comes from other K_L decay modes. The background events from beam line particles are mainly generated by the interactions between beam particles, mainly neutrons, and detectors. The main source of the K_L origin background events comes from $K_L \to 2\pi^0$ decay mode when the KOTO detector misses gammas or misidentifies two gammas as one gamma from the $K_L \to 2\pi^0$ decay events. To reduce the background caused by missing gammas, there are detectors surrounding the designed decay volume as shown in Fig. 1.5. In addition, to reduce

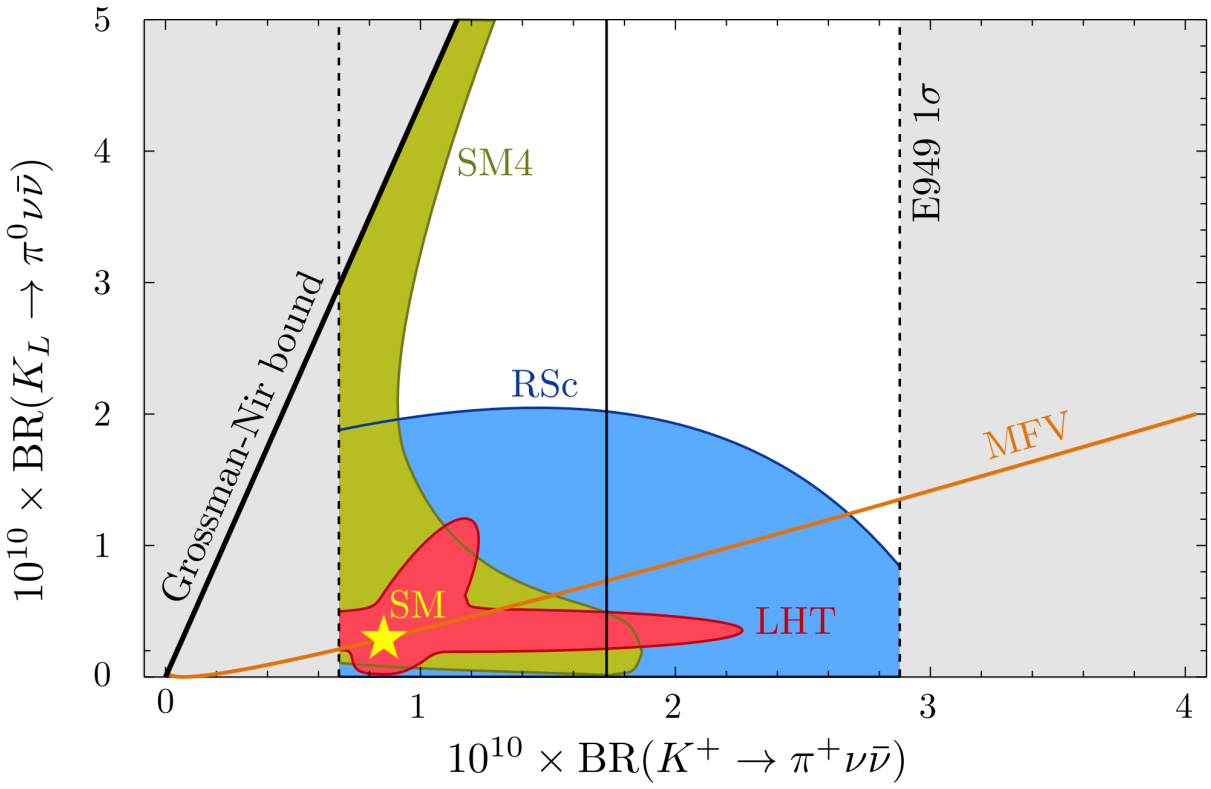

Figure 1.3: The effect of new physics models on the $K_L \to \pi^0\nu\bar{\nu}$ branching ratio [9]. The vertical axis and horizontal axis represent the branching ratio of $K_L \to \pi^0\nu\bar{\nu}$ and $K^+ \to \pi^+\nu\bar{\nu}$, respectively. The upper limit on the ratio between branching ratios of $K_L \to \pi^0\nu\bar{\nu}$ decay mode and $K^+ \to \pi^0\nu\bar{\nu}$ is given by a constraint called Grosman-Nir bound [11] which comes from the iso-spin symmetry. Each label means each new physics model. SM:Standard Model, SM4:Standard Model with a sequential 4th generation (excluded by Higgs physics), LHT:Little Higgs Model with T-parity, MFV: Minimal Flavor Violation Model,, RSc: Randall-Sundrum model.

the missing gamma which passes through the beam hole of the calorimeter, the beamline for the experiment is designed to have small width and height.

The background events from other K_L decay modes are reduced by the following schemes.

- measure gamma energy and position with accuracy.
- count the number of detected particles.
- veto charged particles.

To measure gamma energy and hit position, the calorimeter made of Caesium Iodide (CsI) crystals is used in the KOTO experiment. These measured values are used for event reconstruction.

The number of detected particles is one of important properties of $K_L \to \pi^0\nu\bar{\nu}$ decay mode. The decay mode has only two gammas in the final state. All other decay modes, except $K_L \to 2\gamma$, have charged particles or more than two gammas in the final state. If the detector

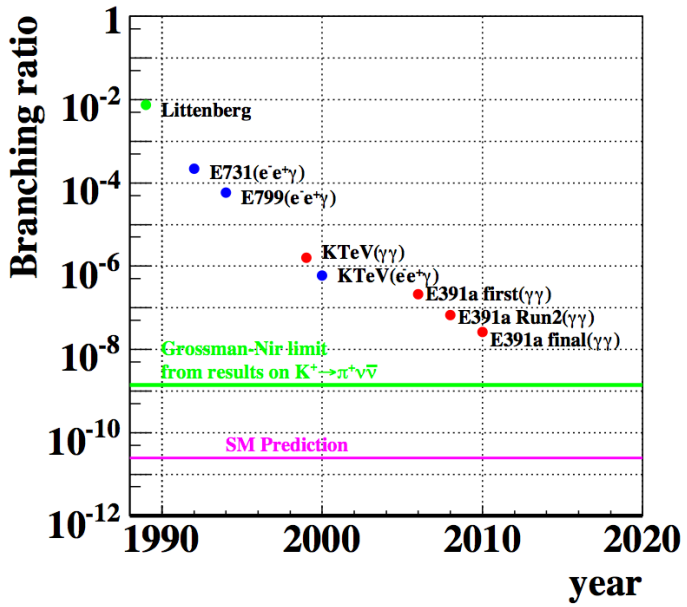

Figure 1.4: History of the 90% CL upper limit of Br($K_L \to \pi^0\nu\bar{\nu}$). The pink line shows standard model prediction. The green line shows the Grossman-Nir limit set from $K^+ \to \pi^+\nu\bar{\nu}$ decay.

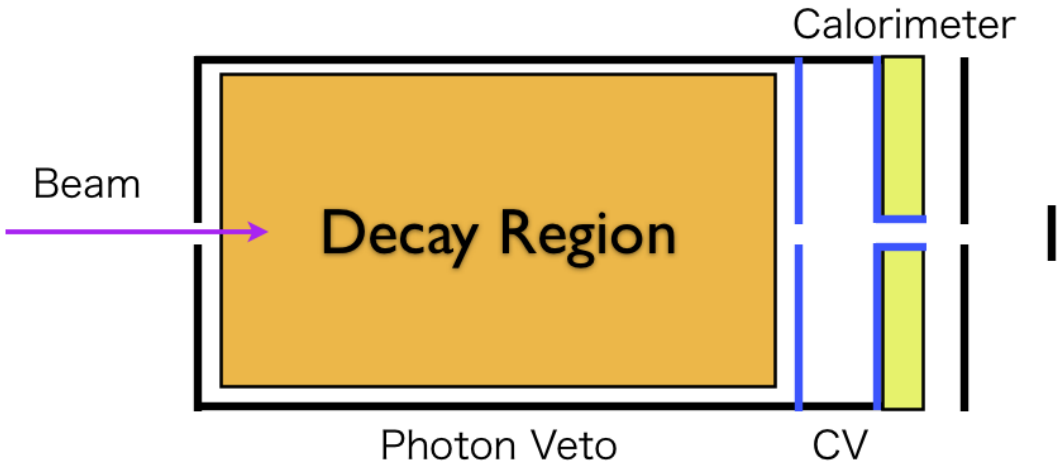

Figure 1.5: Schematic view of KOTO experiment.

is designed to detect all particles except neutrinos, these backgrounds can be easily reduced. In the KOTO experiment, the decay volume is surrounded by high sensitive gamma detectors. The background events from $K_L \to 2\gamma$ decay mode can be suppressed by requiring that the 2γ system has a finite transverse momentum.

To veto charged particles, a thin scintillator, hodoscope, is placed just upstream of the calorimeter. Background events from charged decay modes such as, $K_L \to \pi^{\pm}e^{\mp}\nu_e$, $K_L \to \pi^{\pm}\mu^{\mp}\mu_\mu$ and $K_L \to \pi^+\pi^-\pi^0$, are rejected by this detector.

With this detector setup, the KOTO experiment proposes to observe $K_L \to \pi^0\nu\bar{\nu}$ decay events for the first time. The detection power of an experiment for $K_L \to \pi^0\nu\bar{\nu}$ decay is represented by a parameter called Single Event Sensitivity (S.E.S) which is defined as

$$\text{S.E.S.} = 1/(\text{N}_{\text{K}_\text{L}} \times \text{decay probability} \times \text{acceptance}). \tag{1.9}$$

The KOTO experiment aims the S.E.S. of 8×10^{-12} [7] for the $K_L \to \pi^0\nu\bar{\nu}$ decay. With this S.E.S., two or three $K_L \to \pi^0\nu\bar{\nu}$ decay events from the standard model are expected to be detected in this experiment.

1.3 Calibration of KOTO CsI calorimeter

1.3.1 Introduction

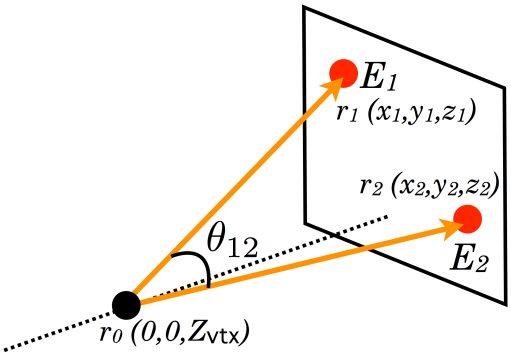

Figure 1.6: A schematic view of π^0 reconstruction. The dotted line represents the center of the K_L beam.

In the experiment, the π^0 from $K_L \to \pi^0\nu\bar{\nu}$ decay is reconstructed by the following method. At first, events with two gammas on the calorimeter are selected. The events are also required that there are no hits in other detectors. The π^0 decay position is reconstructed on the center of the K_L beam where it satisfies

$$M_{\pi^0}^2 = 2E_1E_2(1 - \cos\theta_{12}), \tag{1.10}$$

where θ_{12} is the interior angle between two gamma directions as shown in Fig. 1.6. The π^0 decay position, z_{π^0}, and the transverse momentum of π^0, P_t, which are used to determine $K_L \to \pi^0\nu\bar{\nu}$ decay events, are affected by gamma energy measurement. The region which is defined by $2000\ mm < z_{\pi^0} < 5000\ mm$ and $130\ MeV < P_t < 250\ MeV$, is called as signal region.

The calorimeter consists of 2716 pieces of CsI crystals stacked in a cylindrical support structure as shown in Fig. 1.7. A gamma injected to the calorimeter generates an electromagnetic

shower. The scintillation light generated by $e^{\pm}$ in the shower is guided to PMT which is attached to the crystal, and converted to electronic signal. The waveform of the signal are digitized by flash ADCs. A crystal and a PMT are paired and constitute a CsI module. The variation of

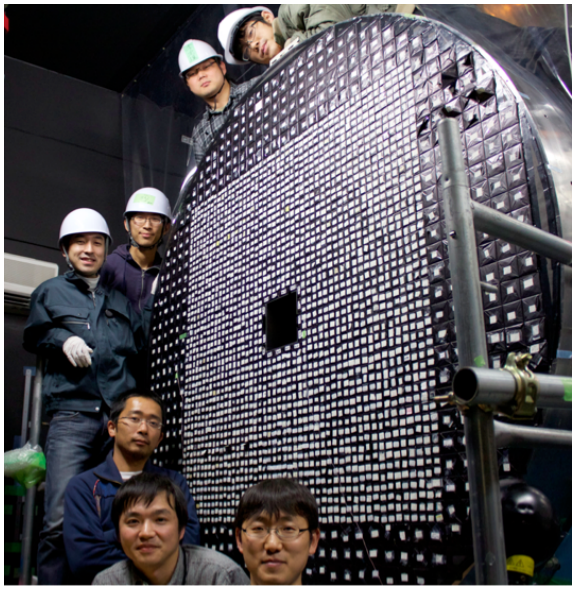

Figure 1.7: Front view of the calorimeter. In the center of calorimeter, there are beam exist.

light yields of crystals and the gains of PMTs causes the output variation of modules. The variation can be reduced by choosing an appropriate parings between crystals and PMTs. The output variation, however, still exists after pairings. This remaining variation is evaluated by energy calibration.

1.3.2 Requirements on the energy calibration method

The $K_L \to \pi^0\nu\bar{\nu}$ decay mode is a rare decay mode, and only several events are expected in the KOTO experiment. If the energy calibration of the calorimeter is done with a poor accuracy, there will be many modules which are largely mis-calibrated. If a gamma from π^0 decay hits a mis-calibrated module, the measured gamma energy is different from its true energy. In the reconstruction of the π^0, the mis-measured gamma energy shifts the reconstructed π^0 vertex and its transverse momentum. If a beam particle interacts with a detector which is placed upstream of the decay volume and generates a π^0, and if its gamma hits a mis-calibrated module, the π^0 can be reconstructed inside the signal region. These backgrounds events cannot be distinguished from the signal event when the number of such events are limited to several events. These events can be reduced by having an accurate energy calibration. I set the required accuracy on the energy calibration to 1%. With this accuracy, the energy shift caused by the mis-calibration is smaller than the typical energy resolution for gamma (2% for 1 GeV).

To monitor the changes of the calibration constants, the signal outputs of modules should be monitored with high rate, and the calibration data should be collected simultaneously with physics data. There are two subjects on the monitoring. The outputs of modules can be changed temporarily by hardware origin problems. If the electric discharge occurs, the gain of PMT shifts temporarily. If the PMT gain is not monitored with high rate, those gain shifts cannot be detected, and they can be the source of accidental background event. The other subject is a long term gradual change of the output of module. The light yields of

the CsI crystals are affected by the temperature, and the output of module can be changed by aging of the calorimeter components. To monitor those changes during the physics data taking, the calibration data should be collected simultaneously with physics data. If the changes are larger than the calibration accuracy, the calibration should be done multiple times. To prevent the lack of events for the calibration accuracy, the calibration data should be taken with adaptive rate, which is enough for the calibration accuracy and has low trigger occupancy. To decide the rate, the relation between the calibration accuracy and the size of calibration data should be determined. In addition, the output of a module is shifted when the component is damaged and fails to recover, or when the arrangement of the calorimeter components are changed by accidentally. Even though the outputs of the modules are monitored, the responses of calorimeter modules are different between the calibration light and the light from the gamma shower. In this case, the calibration is required for each state.

Also, the nonlinearity of the signal height has to be determined during physics data. If a nonlinearity exists, the measured gamma energy is shifted from the true gamma energy. To derive nonlinearity including the calibration constant, the other detector which can measure the energies or the momenta of particles is required in general. However, because there are no other detectors to measure the energy in the KOTO experiment, the nonlinearity and the the calibration constants should be measured with the calorimeter itself.

1.3.3 Energy calibration method for the CsI calorimeter

I have developed the energy calibration method for the calorimeter. It consists of:

- initial calibration using cosmic ray events,
- accurate calibration using $K_L \to 3\pi^0$ decay events, and
- energy scale calibration using π^0 decay events in special run,

with the output monitoring systems, and temperature monitor. There are several restrictions and subjects to the energy calibration.

The calibration sources are limited to cosmic ray events and the K_L decay events, because there are no other detectors which can measure energy or momentum of particles independently in the experiment. Also, the K_L decay events should be fully reconstructed using the measured parameters of the calorimeter. Because of these restrictions and requirements in previous section, a calibration method using $K_L \to 3\pi^0$ decay events on the calorimeter were developed. Because the $K_L \to 3\pi^0$ decay mode is one of main decay modes of K_L, the $K_L \to 3\pi^0$ decay events can be collected easily, and can be taken with no detector setup change. With the calorimeter, all of the decay products of $K_L \to 3\pi^0$, 6 gamma, are detected and their hit positions and energies can be measured.

In addition, because there are no other decay modes which are detected as 6 gamma event on the calorimeter, the collected calibration data is clean. With this characteristics, the calibration method can calibrate the calorimeter simultaneously during the data taking. The method uses Lagrangian multipliers with constraints on the $K_L \to 3\pi^0$ kinematic conditions. Because the method is complex and consists of multiple layers of analytic processes, its performances and limits have to be surveyed in detail.

The method using $K_L \to 3\pi^0$ decay requires an initial calibration with an accuracy less than 5%, because the initial output variation affects the calibration accuracy of the method. The cosmic ray events are selected to use to the initial calibration. For the calibration using cosmic ray events, an analysis frame is required, and its performances have to be determined.

The method also requires an energy scale calibration. The calibration using $K_L \to 3\pi^0$ decay is insensitive to the energy scale of the calorimeter. A special run is thus required for the energy scale calibration. For the accurate energy scale calibration, the ambiguities of the energy scale calibration have to be surveyed, and the calibration result is needed to be confirmed by other method.

The nonlinearities between the digitized PMT signals and the energy deposit on the CsI modules have to be determined. The nonlinearity was measured in the past test experiments which examined the performance of the calorimeter. It, however, was found that the nonlinearity can be changed by setup. The nonlinearity affects the measured gamma energy, and it changes the reconstructed π^0 position of two gamma events. A nonlinearity derivation method was thus required for the calorimeter.

With those requirements, I tested and established the energy calibration method, and proved its ability witch calibrate the calorimeter with an accuracy under 1%.

1.3.4 Outline of the thesis

In this thesis, I will explain the calibration method and its performance of the calorimeter. Chapter 2 explains the J-PARC facilities and KOTO detectors. Chapter 3 explains the data conversion method. Chapter 4-6 explains the sub-calibration methods and their performances. Chapter 7 explains the effect of energy calibration on the parameter distributions. Chapter 8 explains the effect of energy calibration on the parameter distributions. Chapter 9 summarizes the result of this thesis.

Chapter 2

J-PARC Facility and Detector

In this chapter, I will explain the J-PARC Facility, and apparatus of the KOTO experiment. In addition, I will explain the setup of the beam test we did to test energy calibration methods.

2.1 J-PARC Facility

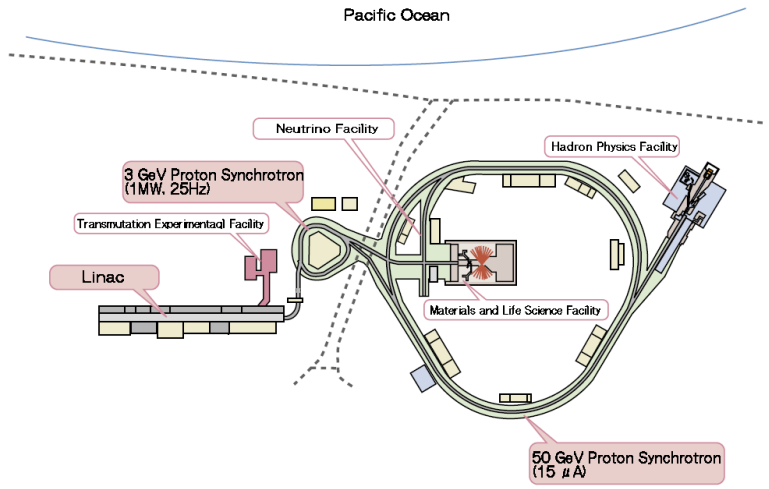

Figure 2.1: An overview of the J-PARC Facility [12].

The Japan Proton Accelerator Research Complex (J-PARC) is a high-intensity proton accelerator facility. This facility was built for many experiments in a wide range of fields using protons, neutrons, neutrinos, and various mesons. As shown in Fig 2.1, the J-PARC accelerator complex consists of three stages of accelerators: 400-MeV Linear Accelerator, 3-GeV Rapid-Cycling Synchrotron, and 30-GeV Main Ring. There are three experimental areas using the proton beam, Material and life science experiment facility, Neutrino experimental facility, and Hadron hall. The KOTO experiment is placed in the Hadron hall.

The accelerated primary proton beam is slowly extracted from the Main Ring, and transported to the Hadron hall every 3-6 seconds. The proton beam bombards a production target (T1 target) which is made of either nickel, platinum, or gold in the Hadron hall. The secondary particles, such as kaons and pions are produced at the target and enter KOTO KL beam line.

The designed beam intensity for the Hadron hall is 300 kW for the slow extraction. The value is equivalent to 2×10^{14} protons on target (P.O.T.) per 3 s spill. The detail specifications of the accelerators are listed in Table 2.1. When I took data in 2012, the beam repetition period was 6 seconds and the beam power was 3 kW.

Table 2.1: Design values of beam parameters for J-PARC proton accelerator

Beam Parameters	
Linac	
Ions	Negative Hydrogen
Energy for RCS injection	400 MeV
Peak Current	50 mA
Average Beam Current	15mA×500μs
Beam Pulse Length	100μ s
Repetition Rate	50 Hz
RCS	
Extraction Beam Energy	3GeV
Repetition	25Hz
Average Beam Current	333 μA
Extraction Scheme	Fast
MR	
Extraction Beam Energy	30 GeV
Average Beam Current	15μA
Repetition	0.2Hz-0.7Hz
Extraction Scheme	Fast/Slow

2.2 KOTO experiment

2.2.1 KL beamline

The plan view of KL beamline is shown in Fig. 2.2.

The K_L beam line is extracted at 16° from the primary proton beamline. Two collimators are placed to form a rectangular KL beam and to suppress beam halo. The beam solid angle is 7.8 μsr, and the width of the beam is 10 cm at the exit of the 20 m beamline. The beam flux was measured in the past beam tests [15] for 2 types of production target materials, nickel and platinum. The results were $1.94\times10^7 K_L$ for Ni Target and $4.19\times10^7 K_L$ for Pt target for 2×10^{14} P.O.T. at the exit of the KL beamline. A 7-cm-thick lead block is placed upstream of collimators to reduce the number of gammas in the beamline. Hyperons produced at the production target decay in the 20-m-long beamline and are eliminated. Electrons and other charged particles in the beam are swept out by a dipole magnet placed between the two collimators. With this feature, neutrons, K_L and decay products of K_L remains in the KL beam.

2.2.2 Overview of the KOTO detector

The plan view of the KOTO detector is shown in Fig. 2.3. In the experiment, π^0s that decayed in the region 3∼5 m downstream of beam exit were used for the analysis.

The region is called as decay volume. The decay volume is surrounded by hermetic veto detectors and the CsI calorimeter. The CsI calorimeter is placed downstream of the decay

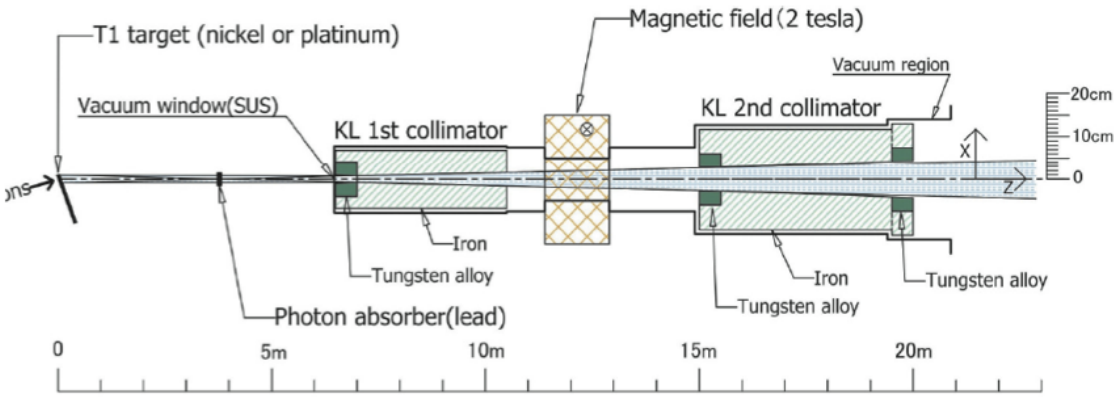

Figure 2.2: Plan view of KL Beam line. Two collimators are mounted on movable stages to adjust beam direction. The magnet is placed between the two collimators to sweep out charged particles in the beam line. A gamma absorber is placed upstream of the first collimator. The tungsten alloy is used at the upstream and down stream edges of the collimators to reduce beam halo produced at those edges.

volume to detect two gammas from $K_L \to \pi^0\nu\bar{\nu}$ decay. Other detectors are placed around the decay volume or in the downstream of the calorimeter to veto extra gammas and charged particles. In the following subsections, I will explain features of each detector.

2.2.3 CsI calorimeter

Features of CsI calorimeter

In the KOTO experiment, an electromagnetic calorimeter is used to measure the energies and hit positions of gammas. The calorimeter consists of CsI crystals stacked inside a cylinder as shown in Fig. 2.4. The geometry of the calorimeter is 2 m in diameter and 0.5 m in length. The calorimeter has a 15 cm square beam hole at the center to let the K_L beam pass through.

The calorimeter consists of three parts, crystals, PMTs, and power supplies. The CsI crystals and PMTs were originally used for the Fermilab KTeV experiment. The calorimeter was disassembled and shipped to Osaka University. The properties, light yields, and gains of all of crystals and PMTs were measured at Osaka. I decided pairings of the crystals and PMTs based on the measurement result.

Two types of pure CsI crystals are used in the calorimeter. They have different sizes; one is $2.5 \times 2.5 \times 50\text{cm}^3$ ("small crystal") and the other is $5 \times 5 \times 50\text{cm}^3$ ("large crystal"). The numbers of small and large crystals are 2240 and 476, respectively. The length of the crystal (50 cm) is equivalent to 27 radiation lengths (X_0) and it is long enough to measure the total energy of gamma shower in the range of 1MeV-3GeV. The sizes of these crystals are smaller than the Moliere radius of CsI crystal (3.8 cm), and thus enables us to identify two gammas as close as $\sim$ 5 cm by analyzing the shower shape. Because the centeral region of the calorimeter requires a better position resolution than outer region, the small crystals cover the central 1.2 m$\times$1.2 m region and the large crystals surrounded the small crystals, as shown in Fig. 2.4,

Two types of PMTs were prepared for the two types of CsI crystals. On the small crystals, 3/4 inch Hamamatsu R5364 were attached, and on the large crystals, 1.5 inch Hamamatsu R5330 were attached. They are called "small PMTs" and "large PMTs", respectively. The mean of PMT gains are 5000 and 8000 for small PMTs and large PMTs, respectively. In front

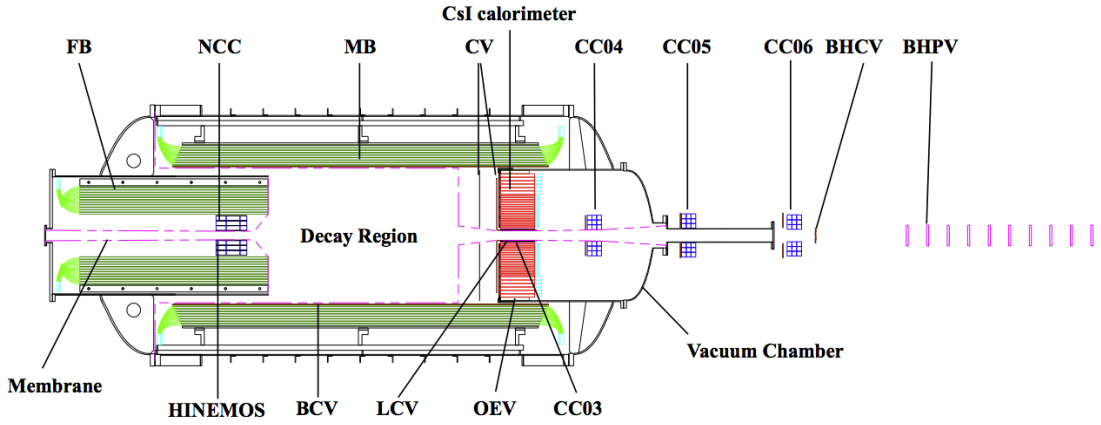

Figure 2.3: Plane view of Detector setup. The decay volume is in the middle of a vacuum chamber. Particle detectors surround the decay volume. The calorimeter is placed downstream of decay volume, and it is used to detect gammas from K_L decays. Other detectors are used to detect other particles and additional gammas.

of each PMT, a UV transmitting filter (FGUV11) was attached to filter slow components of CsI scintillation light by cutting off wavelength larger than 400 nm. To compensate for the low gain, three types of preamplifiers, whose multiplication factors were different, were attached to PMTs depending on their gains. Silicone cookies were used to optically connect the PMTs and the crystals. The connection is sustained by pushing the PMTs towards the crystals with a pair of spring-attached hooks.

For PMT bases, Cocktcroft-Walton bases (CW bases) were developed to operate them in vacuum. A nominal base with voltage-dividing resistors generates about 700 mW of heat. The KOTO CsI calorimeter needs 2716 pieces of bases, and it is difficult to cool about 2 kW of heat in vacuum. The temperatures of PMTs and preamplifiers should be kept low to reduce their failure risks. The temperatures of CsI crystals should also be kept low, because the light yield of crystals decreases at higher temperature. The CW bases, thus, are used for the calorimeter to reduce heat generation. The CW base uses the Cocktcroft-Walton circuit to generate high DC voltage from a low AC voltage. In case of our CW base, it generates up to 2000V with 5V supply voltage, and generates only 60 mW of heat per module.

Adjustment of outputs with pairing PMTs and crystals

The sum of pulse heights of all channels is used to trigger events with a large total energy deposit in the calorimeter. Thus, the ratio between the energy deposit and the pulse height of a CsI module is required to be uniform across the calorimeter.

For each CsI crystal, the light yield and its position dependence along the crystal length were measured using a ^{137}Cs RI source. The light yield affects the detection probability and energy resolution of gamma. The position dependence of light yield also affects the energy resolution for gammas. The position dependence of light yield in a crystal was adjusted by using different kinds of Al mylars to wrap the crystals at the KTeV experiment. It was confirmed that the position dependence of light yield was within $\pm 5\%$ of its mean value in each crystal.

For the PMTs, the signal height linearities and gains were measured. The measurement was done with a laser calibration system which was used in the gain monitoring system described in Section 2.4. The nonlinearities of PMTs were confirmed to be less than 2% for the pulse height

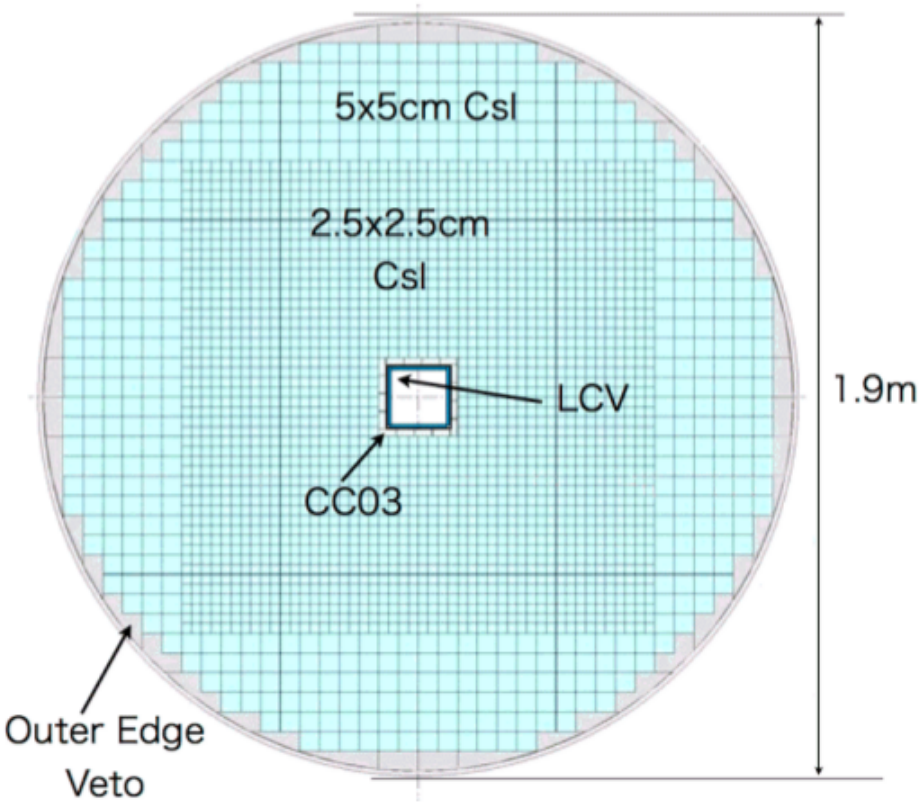

Figure 2.4: Geometry of CsI calorimeter and neighbouring VETO detectors. The CC03 is placed around the beam hole. The LCV is attached on the inner beam hole surface of CC03. Outer edge veto is placed between the CsI crystals and cylindrical support structure.

less than 2 V corresponding to 10∼20 GeV.

After the measurements, I mated low-light-yield crystals with high-gain PMTs and vice versa to minimize the variations of the energy to pulse height ratios. In addition, I adjusted the high voltage for each PMT between 1200 V and 1750 V to tune the ratios to within ±3%.

2.2.4 Other Veto detectors

Front Barrel and Neutron Collar Counter

The Front Barrel (FB) and the Neutron Collar Counter (NCC) shown in Fig. 2.3 are placed in the upstream section of the detector system to detect gammas hitting upstream of the decay volume. The FB is a 2.5 m-long of cylindrical shaped detector, and it consists of 16 modules. Each modules is made of alternating lead and plastic scintillator plates. The total thickness is 410 mm, and it equals 16 X_0 in the radial direction.

The NCC is placed inside the FB, and is made of pure CsI crystals. The NCC has additional purpose to measure halo neutron flux and its energy spectrum. Each module of the NCC is segmented into three sections along the beam direction and they are readout individually. With this configuration, the NCC can distinguish between gammas and neutrons.

Main Barrel and Barrel Charged Veto

The Main Barrel (MB) is placed in the middle section. It consists of 32 modules, and each module is made of 44 layers of lead and plastic plates. The length and the thickness of a module are 5.5 m and 350 mm, respectively. The thickness is equal to 14 X_0. The MB wraps the decay volume and is used to detect extra particles from $K_L \to 2\pi^0$, $K_L \to 3\pi^0$, $K_L \to \pi^+\pi^-\pi^0$, and other K_L decay modes. Barrel Charged Veto is placed on the inner surface of each MB module to identify charged particles. It consists of one layer of 5 mm thick plastic scintillators.

Charged Veto

The Charged Veto (CV) is placed upstream of the calorimeter to cover the surface of the calorimeter. It is used to identify charged particles and measure their hit positions. It consists of 2 planes, Front CV and Rear CV. The Front CV is located 25 cm upstream of the CsI calorimeter and the Rear CV is located 5 cm upstream of the calorimeter. Each plane of CV consists of 3mm-thick scintillators.

CC03, Linar Charged Veto, Outer Edge Veto

The Collar Counter #3 (CC03), Linar Charged Veto (LCV), Outer Edge Veto (OEV) are placed in the same section with the calorimeter. Their locations are shown in Fig. 2.4.

To detect gammas hitting near the beam hole, the CC03 is placed around the beam hole of the calorimeter. The CC03 consists of 16 pieces of pure CsI crystals. The dimension of each crystals is $45.5 \times 18 \times 500\text{mm}^3$.

The LCV covers the surface of the CC03 facing the beam. The LCV detects charged particles which enter the calorimeter from the beam hole. It consists of 4 planes of 3 mm-thick plastic scintillator.

The OEV fills the gap between the calorimeter and the endcap cylinder, to detect gammas that enter the gap. It consists of 44 modules of different shapes. The OEV is a sampling calorimeter consisting of lead and scintillator plates.

CC04, CC05, CC06

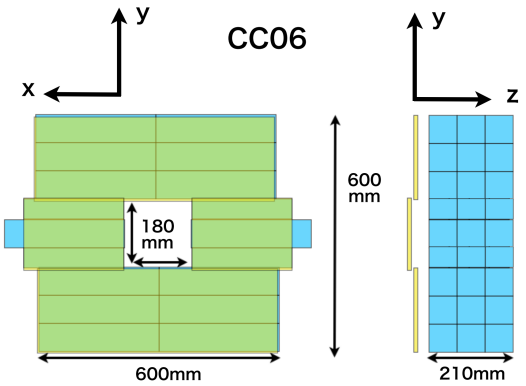

Figure 2.5: Structure of CC06. The CsI crystals (sky blue in the figure) are used to detect gammas. The plastic scintillators (green and yellow in the figure) are located upstream of the CsI crystals to identify charged particles.

Other collar counters, CC04, CC05 and CC06, are placed downstream of the calorimeter to detect gammas passing through the beam hole of the calorimeter. They have similar structures as shown in Fig. 2.5. Pure CsI crystals are stacked in three layers around the beam. The beam hole sizes are 170 mm square for CC04, 210 mm square for CC05, and 180 mm square for CC06.

Beam Hole gamma Veto (BHPV)

The Beam Hole gamma Veto (BHPV) is placed at the most downstream of other KOTO detectors to detect gammas which escape from the beam hole of the calorimeter. The BHPV detector consists of 25 Cherenkov counters. Each module has a lead plate and a block of aerogel. The lead plate converts gammas into electron-positron pairs which emit Cherenkov light in the aerogel. The Cherenkov light is guided to PMTs by mirrors and Winston cones.

2.2.5 Signal readout method and data acquisition system

Signal readout

The total K_L decay rate is 3×10^6 decays per second in the vacuum region in case of full beam intensity (2×10^{14} P.O.T.). To handle multiple hits under the high decay rate, a waveform readout was adopted for all the detectors. Signals from all the detector channels are digitized with Flash ADC (FADC) boards. Data sampling rate is 125 MHz for the calorimeter and most of other detectors. For BHPV, the sampling rate is 500 MHz. Bessel low pass filters are installed on the 125 MHZ FADC boards to widen the signal width to 50 ns. With this scheme, the waveform is measured at around 16 points to achieve a good timing resolution; without it, the number of sampling points is 3 for a 22 ns-wide raw signal pulse.

DAQ system

The data acquisition (DAQ) system of the experiment consists three levels of trigger systems. Each FADC board receives 16 analog inputs and sends a local sum of the signals to Level 1 (L1) trigger boards every 8 ns. A master control board for a DAQ system, called MACTRIS, communicates with the L1 trigger boards and issues L1 triggers based on those local sums. The trigger is distributed to all the FADC boards. Each board has a memory to store the digitized waveform for 4 μs. When it receives a L1 trigger, it sends the saved waveform to a L2 trigger board. The timing and the number of sampling points can be adjusted. For the calibration test, the number of sampling points was set to 48. For physics runs it will be set to 64.

The Level 2 (L2) trigger board has two 2 GB-sized memories to buffer data and to send data to a PC farm. The data stored on one memory is sent to the PC farm while other memory receives data from FADCs. Two memories interchange their roles every beam spill. With this scheme, the DAQ system can take data continuously. The Level 3 (L3) trigger system on the PC farm builds events and selects data to be sent to a data storage at KEK. The maximum DAQ rate is limited by the size of L2 memory, 2GB/spill, and the data transfer speed from L3 to KEK storage, 2GB/s. Each run holds 80 k events.

Trigger scheme

The trigger control board, MACTRIS, selects events for data taking with the following several schemes. There are two representative trigger schemes.

One of them is a total energy scheme (E_T trigger scheme). It uses the sum of pulse heights from the calorimeter to make a trigger decision. If the sum of all the channels exceeds a given

threshold, MACTRIS issues a L1 trigger. For this trigger scheme to work properly, the energy deposit / signal height ratio of all the calorimeter modules need to be uniform.

Another scheme is called section counting trigger scheme. The calorimeter is segmented to several sections, 10 for the runs used in this thesis, and the sum of pulse heights in each section is calculated. If the sum exceeds a given threshold, the section is treated as a "hit section". If the number of hit sections is larger than a predefined number, the MACTRIS issues a L1 trigger.

The section counting scheme is more efficient than the E_T trigger scheme to collect events from $K_L \to n\gamma$ (n $\geqslant$ 4) decays. This trigger scheme can reduce the trigger rates due to $K_L \to \pi^{\pm}\mu^{\mp}\nu_{\mu}$ and $K_L \to \pi^{\pm}e^{\mp}\nu_e$ decay modes which have less than four detectable particles. The trigger rate due to $K_L \to 2\pi^0$ and $K_L \to 3\pi^0$ decays with missing gammas are also reduced by this scheme. This scheme was used for this thesis.

2.3 Setup for beam test

To test the calibration method, a special setup was used. The detector setup was different from the physics run setup. The calorimeter was placed in the air, and upstream and downstream detectors had not been installed yet. In addition, a dipole magnet called KURAMA, and drift chambers were placed upstream of the calorimeter to commission the calorimeter.

2.3.1 Geometry

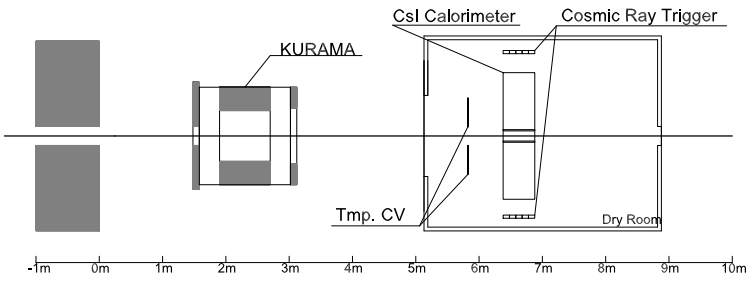

Figure 2.6: Schematic view of the experiment setup.

The arrangement of the experiment is shown in Fig. 2.6. CsI crystal is hygroscope, and if the crystal is exposed in high humidity, the surface of the crystal is clouded and the light yield of the crystal is reduced. The calorimeter was thus placed in a dry room where the relative humidity was kept under 20%. Cosmic ray trigger scintillators were placed above and underneath the calorimeter. In upstream of the calorimeter, an array of plastics scintillators (shown as "Tmp. CV" in Fig. 2.6), instead of the CV, was installed to veto charged particles.

2.3.2 CsI Calorimeter

In the beam test, all the small CsI modules and half of the large CsI modules, which were placed left and right sides of the small modules, were used. A half of silicone cookies for small CsI modules were damaged by a previous calorimeter test. The light transparencies for UV of those silicone cookies were reduced by a half. The PMTs for the large modules in the top and bottom regions of the calorimeter were not turned on at the beam test. The channels used in this beam

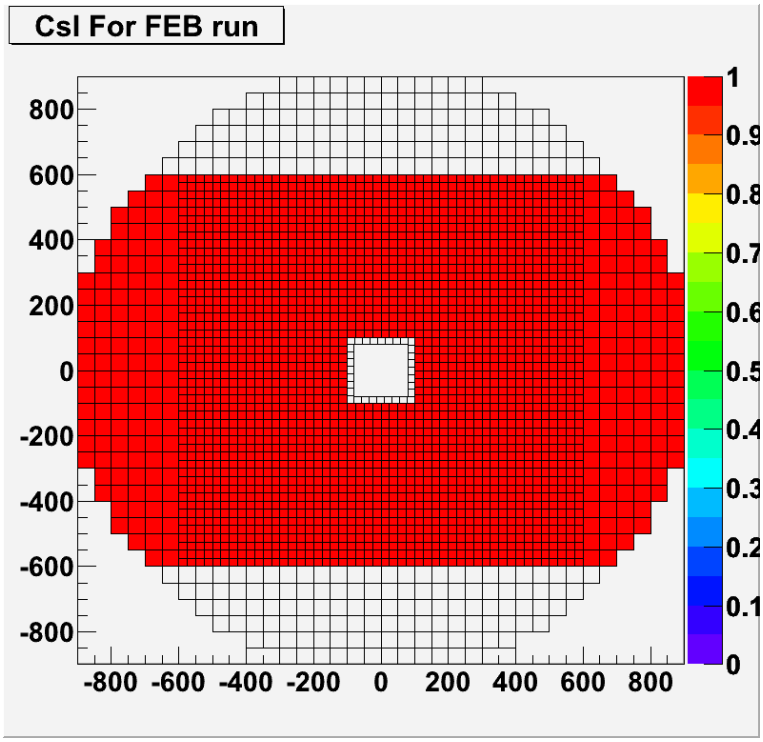

Figure 2.7: Channels in CsI Calorimeter read out for calibration method test are shown in red.

test are shown in Fig. 2.7. The channel assignment of crates and L1 sections are shown in Fig. 2.8.

2.3.3 Cosmic ray trigger scintillator

I used cosmic rays for the initial calibration of the calorimeter. Two cosmic ray trigger counters were used to trigger cosmic ray events. Each plane was segmented into five sections along the beam direction. The size of each section was 10 cm in beam direction, and 2 m in the other direction to cover the calorimeter. The signals were read out via two PMTs attached at each end of the scintillator.

2.3.4 Temporary Charged Veto

Different charged veto (Tmp. CV) was placed upstream of the calorimeter, as shown in Fig. 2.9. One CV module consisted of 4-6 pieces of $120 \times 5 \times 1\text{cm}^3$-sized plastic scintillator bars. Each bar was read out by a wavelength shifting fiber and a PMT. It was used to veto charged K_L decays.

2.3.5 Spectrometer

The spectrometer was placed upstream of the calorimeter. It consisted of a dipole magnet and 4 planes of wire chambers. It was used for testing the performance of the calorimeter with $K_L \to \pi^{\pm} e^{\mp} \nu_e$ decay events. The test is not directly related to this thesis, but I will refer the test several times as Ke3 run or Ke3 calibration in this thesis. The detail of the test is written in Appendix A.

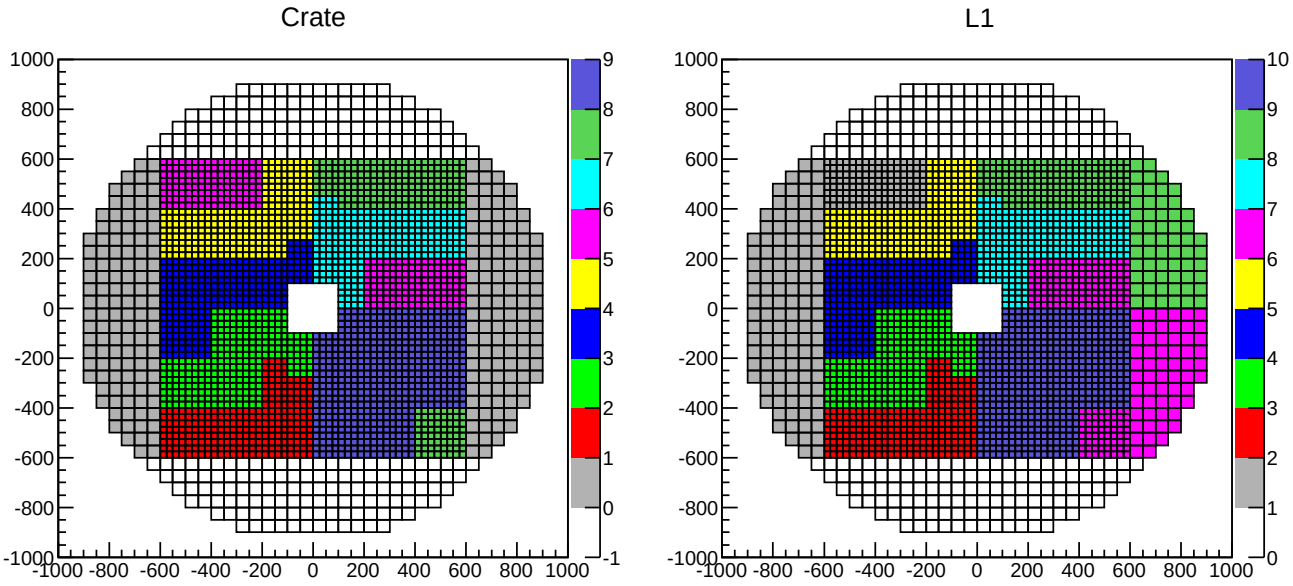

Figure 2.8: Channel assignments of VME crates (left) and L1 sections (right).

2.4 Status monitoring system

2.4.1 Laser gain monitoring system

The output of PMT may be changed by temperature, optical connections with crystals or other reasons. A monitoring system utilizing a Laser was prepared for detecting such behaviors of the calorimeter PMTs. The monitoring system was used in the KTeV experiment. I refreshed the system and reformed it for the KOTO experiment.

A Nd:Yag Laser (λ = 355 nm) is used as a UV light source. The light from the laser is distributed to four optical fibres by an optical system shown in Fig. 2.10. The fibers deliver light to four light distribution devices shown in Fig. 2.11. The light distribution device has a spherical shape and 750 thin fibres are attached on the surface of the device. In the light distribution devices, the injected UV light shines a liquid scintillator which is placed at the center. The liquid is 9-Methylcarbazole ethanol solvent and emits scintillation light with λ =365 nm and 385 nm. The scintillation light is captured by the thin fibers. The other end of each fiber is attached to the back of a CsI crystal to supply calibration light to each PMT. The repetition rate was set to 5 Hz for the runs. Each light distribution device supplies 1/4 of all channels of the calorimeter. The intensity of supplied light is monitored with two PIN diodes which were attached at the side of the light distribution system.

2.4.2 Temperature monitoring system

Thermocouples are installed to measure temperatures of each detector. Temperature affects the PMT gains, and the light yield of crystals and scintillators. For example, the light yield of CsI crystal decrease by 1.4%/°C [13]. The experiment area is air-conditioned and expected to have small temperature fluctuation less than $1°C$. The PMTs and their preamps, however, are main heat sources and affect the temperature of CsI crystals. After PMTs and preamps are turned on, the temperature of CsI crystal rises until a temperature distribution reaches a

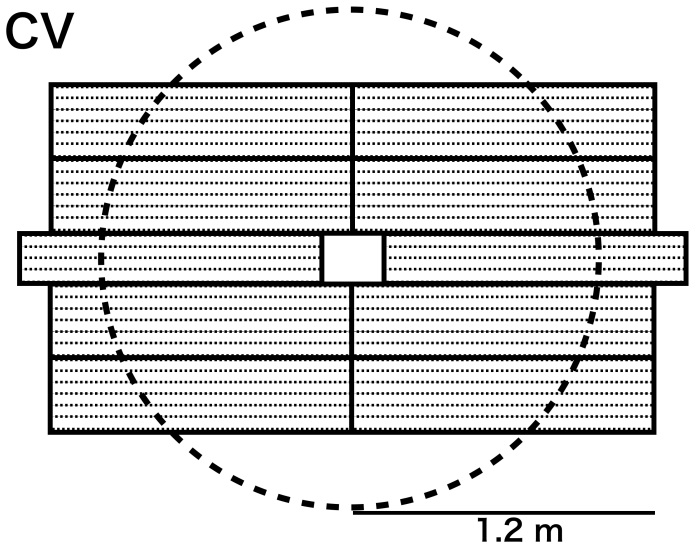

Figure 2.9: Front view of temporary charged veto. Dotted circle represents the outline of the CsI calorimeter.

thermal equilibrium. To monitor the temperature of the calorimeter, I attached 48 channels of thermo-couplers on the front and back of the calorimeter.

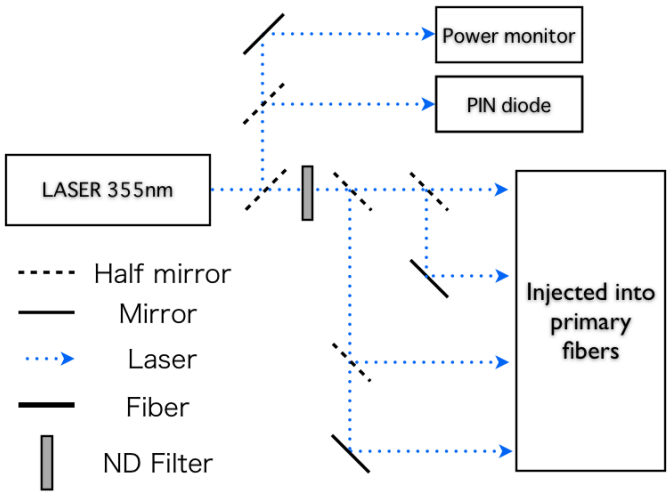

Figure 2.10: Schematic view of upstream part of Laser gain monitoring system. The Laser beam is divided with mirrors and injected into four primary fibers. The light intensity can be adjusted with a neutral density (ND) filter.

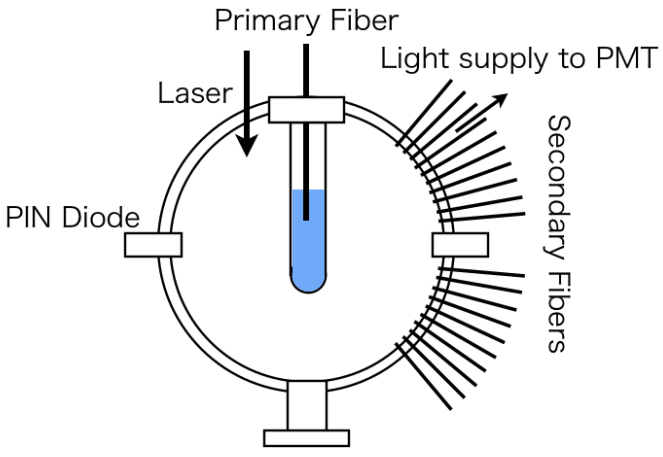

Figure 2.11: Schematic view of light distribution device of Laser gain monitoring system. The light is injected into scintillator placed at the center of light distribution device. The light from scintillator is distributed to PMTs through thin fibers pointing the center.

Chapter 3

Data conversion

3.1 Waveform analysis

3.1.1 Conversion of waveform to energy and timing

In this section, I will explain the methods to convert the waveform recored by FADC to energy and timing of the pulse. The data consisted ADC counts of 48 sampling points in time per module. A waveform sample is shown in Fig. 3.1.

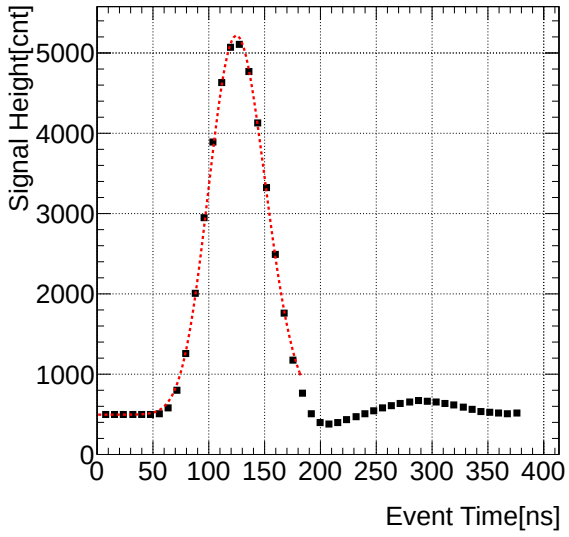

Figure 3.1: The raw data recorded by FADC. Points are recored every 8 ns.

Waveforms from the calorimeter were fitted with templates. The templates were made in the following way.

- Fit pulse with asymmetry gaussian function and extract pulse height and peak timing.
- Normalize the pulse shapes with the pulse height, and shift the pulse in time to align the peak timing.
- Collect normalized and shifted waveforms, and calculate mean values of the collected pulse shape with a 1 ns interval.

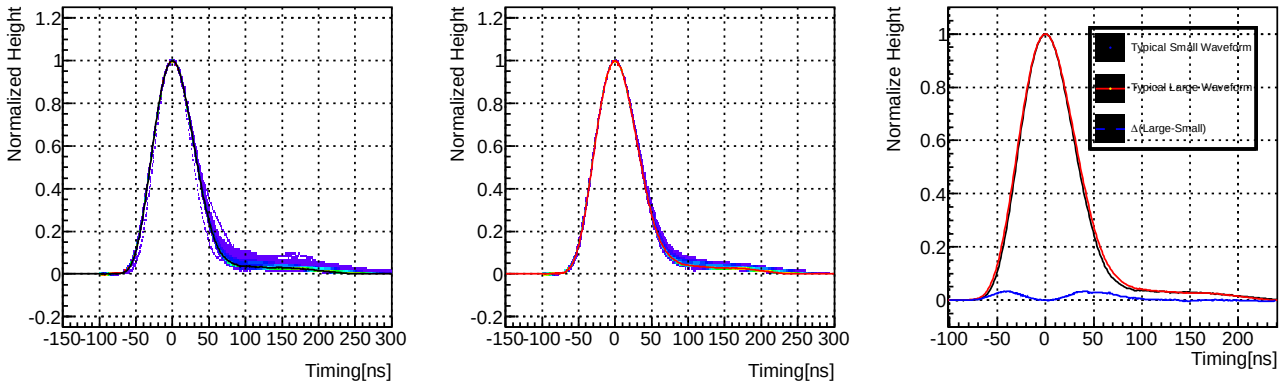

Figure 3.2: The templates of small modules (left) and large modules (middle) are shown. In the right figure, the typical waveform of small modules (left, black line) and large modules (center, red line) and their difference (right, blue line) are shown. The difference of templates widens at the tail region (50 ns in the figure). The waveform of large module is slightly wider than small module.

- Interpolate between the 1 ns-interval points to define a template shape.

The asymmetric gaussian function is defined as:

$$y = h \times \exp\left\{-\frac{(x-t)^2}{2\sigma^2(x)}\right\} + g \tag{3.1}$$

$$\sigma(x) = p_0 + p_1 \times (x - t). \tag{3.2}$$

The fit parameters h, t, and g are pulse height, pulse peak timing, and pedestal, respectively. The fit parameters p_0 and p_1 are the width of signal and asymmetric parameter, respectively.

The waveform varied between modules, and depended on the pulse height. The template was thus made for each module of the calorimeter. I used $K_L \to 3\pi^0$ decays for making templates, but the deposit energy spectrum of each CsI module was correlated with the position of each module. In case of outer modules of the calorimeter, the number of events in high energy region was not enough to make templates. With this reason, I made a template for each module using pulses whose heights are in 200 ∼400 ADC counts (20-40 MeV) in the waveform fitting.

3.1.2 Properties of waveforms

Channel dependence of waveforms

Various templates are shown in Fig. 3.2. To quantify channel dependence of the waveform, I defined "Difference of waveform", Δ, using 13 points with 8 ns interval around the peak time of template as:

$$\Delta = \frac{1}{13}\sum_{i=-6}^{6}\left|\frac{f(8i+t_{peak}) - g(8i+t_{peak})}{g(8i+t_{peak})}\right| \times 100[\%], \tag{3.3}$$

where $f(x)$ represents a template of a module and $g(x)$ represents a standard template for large or small module. Figure 3.3 shows the variation of templates. The Δ distribution has a peak at $\sim 0.5\%$, and has a tail on the high side. The applied voltages and light yields of modules had a position dependent pattern, but the Δ had no apparent dependence on the module position.

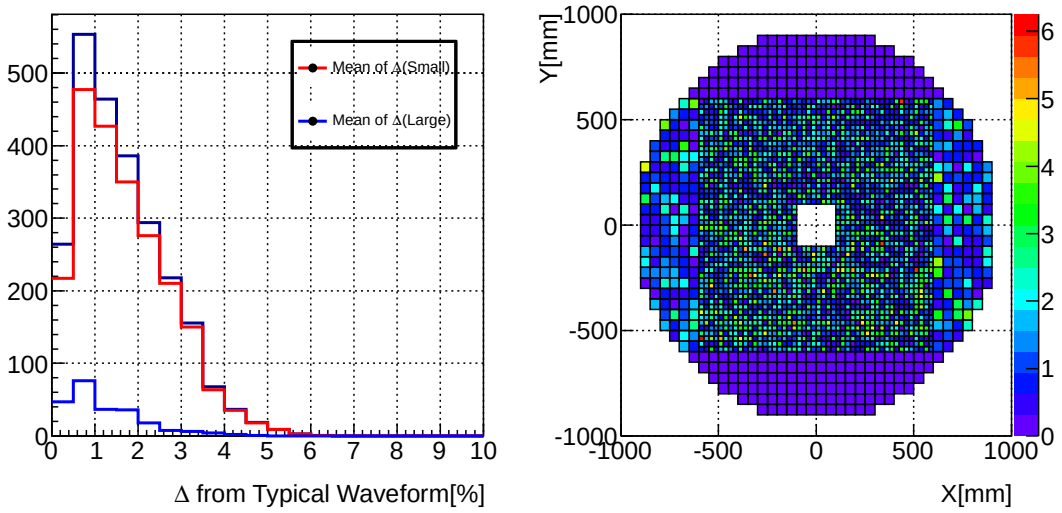

Figure 3.3: [Left]The distributions of Δ. Red line shows the Δ distribution of small modules, and blue line shows that of larger modules. [Right]XY distribution of Δ. Two channels which had apparently different waveform are not included.

The shape of waveform thus mainly depends on modules, and less on applied voltage or light yield of each module.

Light source dependence

The templates were different between calibration Laser events and $3\pi^0$ decay events as shown in Fig. 3.4. The templates of Laser events has undershoots in tail region and narrower width than the templates of gamma events. This is because the original pulse shapes are different between the two, and the Bessel filter in the FADC is tuned for the waveforms of gamma event.

Height dependences of waveforms

Nonlinearities on the pulse height was reported by a previous research [16]. The nonlinearity is represented by a ratio of pulse height recorded by FADC and input signal height. The ratio was smaller for larger input signal as shown in Fig. 3.5. In this thesis, this result was used to correct for the nonlinearity.

To check the nonlinearity of each channel, the laser monitoring system was used. The system can change its light intensity by 3 orders of magnitude, and can scan output of each module from a few MeV to several GeV equivalent. Using the Laser monitoring system, the waveform at each light intensity was measured. The waveform widened and delayed at the high light intensity as shown in Fig. 3.6.

As shown in Fig. 3.5, Laser monitoring system revealed that the FADCs in one VME crate(#7) has different nonlinearity curves from others. In Chapter 7, I will discuss how to measure the nonlinearities of CsI modules.

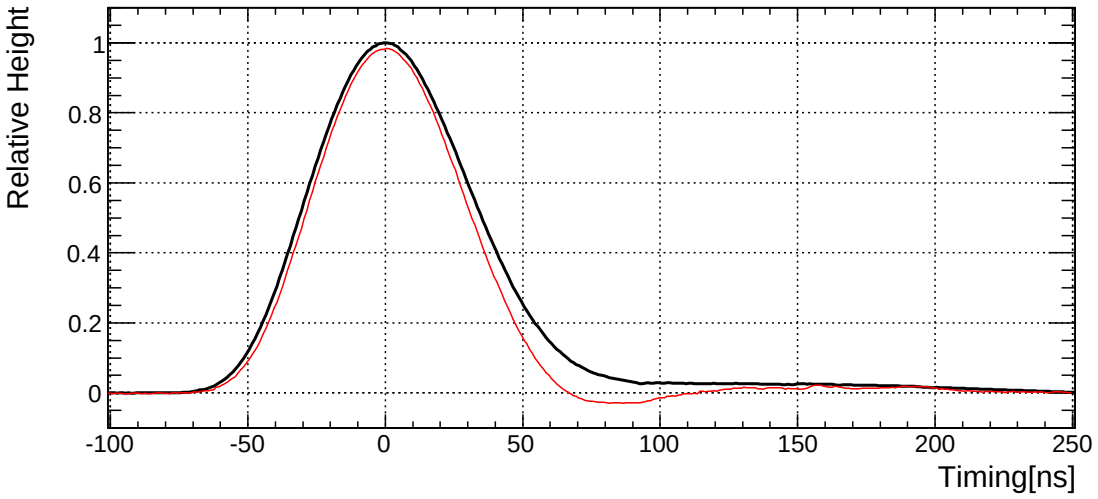

Figure 3.4: The template pulse shapes are shown for Laser events (red) and gamma shower events (black).

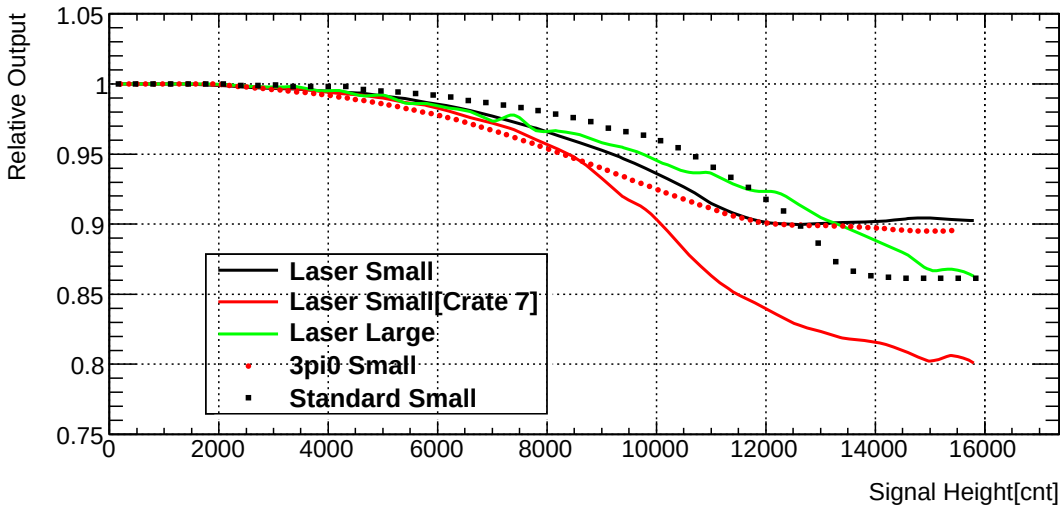

Figure 3.5: Output nonlinearities measured with various measurements. The nonlinearity which was measured in the previous test [16] is shown by dotted black line "Standard Small". The nonlinearities which was measured using the Laser system are shown by solid lines. In the previous test the nonlinearities did not depend on the crystal size. The nonlinearities using the laser system, however, shows a crystal size dependence.

3.2 Temperature Effect Correction

The light yield of CsI crystal has a temperature dependence. The correlation constant is known as $(-1.4 \pm 0.1)\%/^{\circ}\mathrm{C}$ [13]. The correlation constant was derived from the beam data and cosmic ray event to confirm the value. There were three types of data to measure the correction constant, cosmic ray data, data for energy scale calibration, and Ke3 calibration data. The temperature of the upstream surface of the calorimeter was used as a representative temperature.

All cosmic ray data were combined into several periods by run numbers, to measure temporal changes of the cosmic ray output of all CsI channels. The average of the cosmic ray outputs of all CsI channels was set as a representative cosmic ray output for the period. The average temperature for the period was set as a representative temperature. The result is shown in Fig. 3.7. The temperature dependence of light yield was derived by fitting the graph. The dependence measured with the cosmic ray events was $(-1.36 \pm 0.03)\%/^{\circ}\mathrm{C}$.

The dependence also can be derived by using the peak of reconstructed π^0 mass distributions from the data taken for energy scale calibration mentioned in Sec. 1.3. The π^0 mass and average temperature was measured for each run. The dependence was measured to be $(-1.4 \pm 0.3)\%/^{\circ}\mathrm{C}$.

In the analysis of the Ke3 calibration data, an energy of electron was measured by the calorimeter, and the momentum of electron was measured by the spectrometer. By using the ratio between the two measured parameters, E_e/p_e, the temperature dependence was measured to be $(-1.48 \pm 0.03)\%/^{\circ}\mathrm{C}$ [17].

The acquired three temperature correlation and the known value were consistent to within 6%. In this thesis, we adopted $-1.48\%/^{\circ}\mathrm{C}$ for the temperature dependence correction to compare the calibration result with the Ke3 calibration result. For the correction, the average temperature in each run was used.

3.3 Energy conversion

The height of waveform, h, from a calorimeter module, whose ID is i, is converted to energy as:

$$E = C_{tot}(i) \times C_{temp} \times h/\delta(h), \tag{3.4}$$

where C_{tot} is the calibration constant, C_{temp} is temperature correction constant for a run, $\delta(h)$ is a nonlinearity correction function. The C_{tot} consists of the calibration results of

- initial calibration using cosmic ray event,
- 3pi0 calibration using $K_L \to 3\pi^0$ decay events, and
- energy scale calibration with special setup.

The C_{tot} for a calorimeter module, $C_{tot}(i)$, is written as:

$$C_{tot}(i) = C_{init}(i) \times C_{3\pi^0}(i) \times \Delta_E. \tag{3.5}$$

Here, C_{init} is the calibration result of the initial calibration. Its unit is MeV / ADC count. $C_{3\pi^0}$ is the calibration result of the 3pi0 calibration. Δ_E is the calibration result of energy scale calibration, and it is referred as energy scale in this thesis. $C_{3\pi^0}$ and Δ_E are dimensionless values.

For the data which is used in the 3pi0 calibration, only C_{init} in the C_{tot} is applied on the energy conversion. For the data which is used in the energy scale calibration, C_{init} and $C_{3\pi^0}$ were applied.

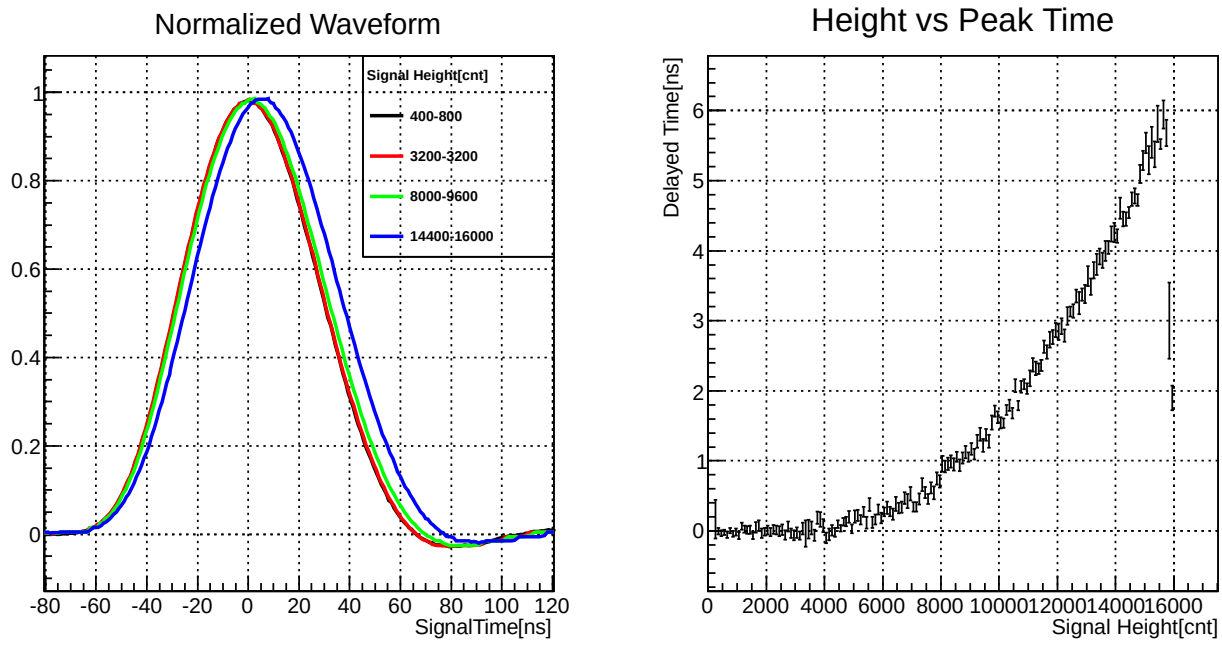

Figure 3.6: Changes of waveforms for various pulse heights. The changes of waveform of Laser event for different pulse height regions (left) and the correlation between timing delay and the pulse height (right) are shown.

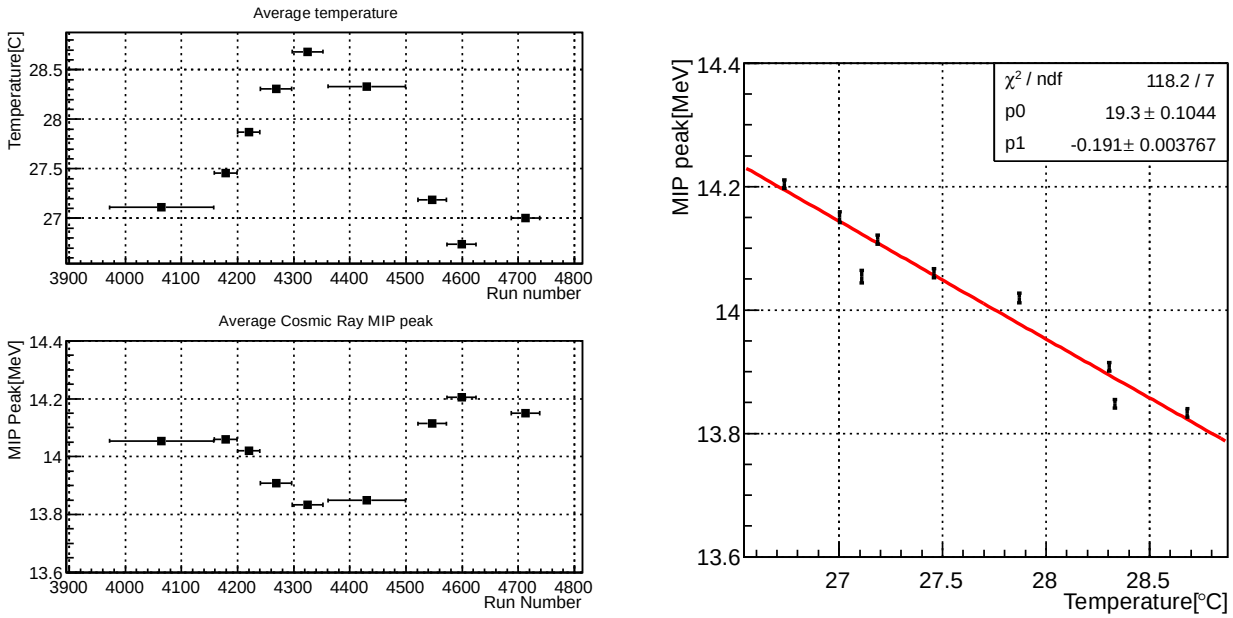

Figure 3.7: The temperature dependence of the representative cosmic ray outputs during data taking. [Left, Top]The surface temperature of the calorimeter *vs* run numbers. [Left, Bottom]The average MIP *vs* run numbers. [Right] The correlation of the representative cosmic ray outputs and temperature. The slope of fitted line was (-0.191 ± 0.004) MeV/°C.

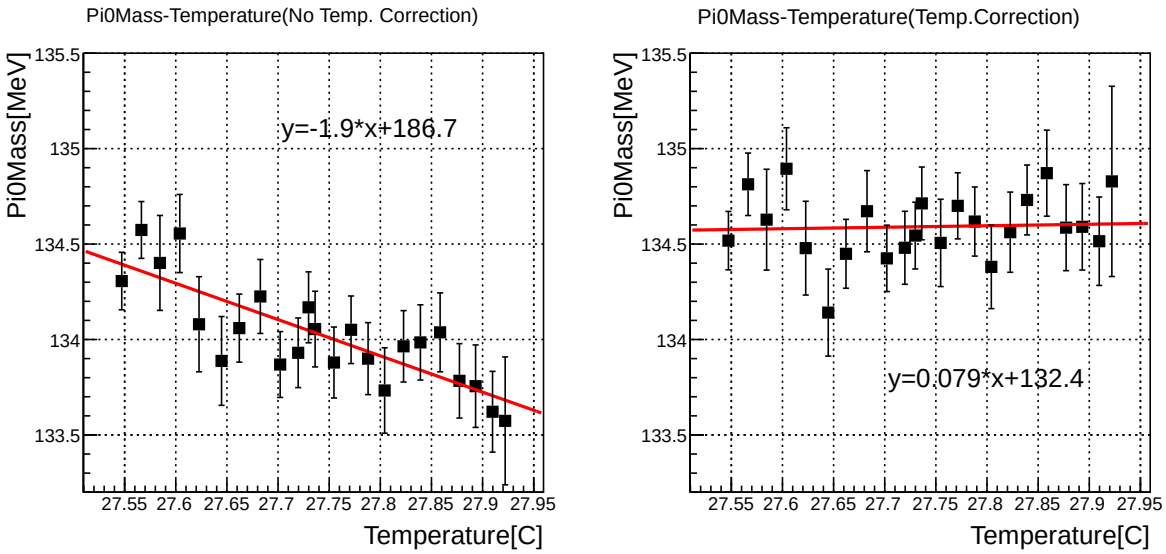

Figure 3.8: Correlation between reconstructed π^0 mass peak value and the calorimeter surface temperature for before (left), and after (right) applying temperature correction of $(-1.48 \pm 0.03)\%/^{\circ}\mathrm{C}$. The red lines show fitted linear function.

3.4 PMT gain stability

The laser events collected at 5 Hz were used to monitor the stability of the PMT gains. The gain stability was defined by ratio between signal heights of a CsI channel and a reference CsI channel (module number 22). The ratio was collected each run, and its mean was used to represent the PMT gain in the run. To reduce the effect of nonlinearity, I selected channels whose pulse heights were within 2000-10000 counts, and its signal height nonlinearity was corrected. The ratio of each channel was normalized with the ratio from the run 4221. I confirmed that the temporal PMT gain variations were less than 0.5% on average, and 0.3% in RMS, as shown in Fig. 3.10.

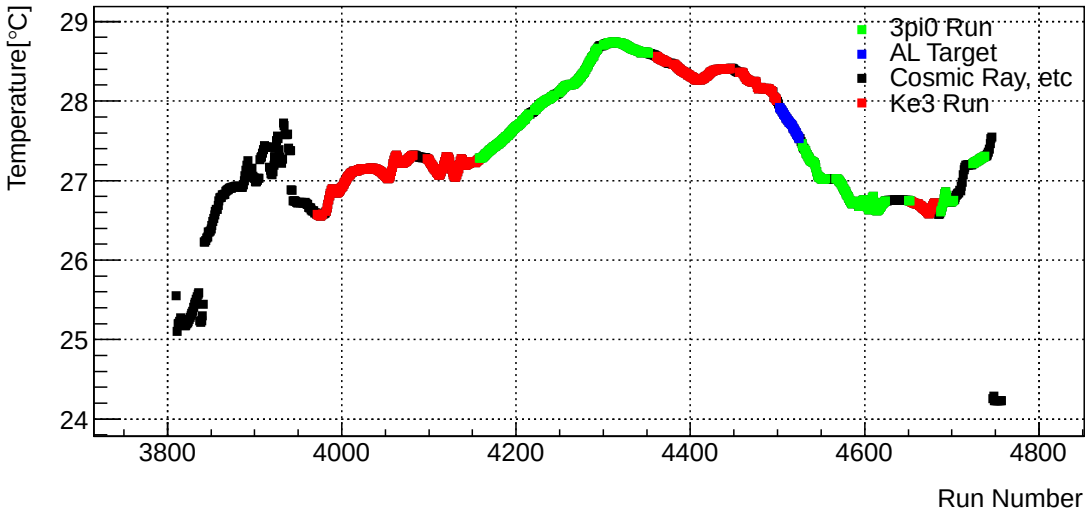

Figure 3.9: Temperature at the surface of the calorimeter during the data taking. Each color represents each type of run, 3pi0 (green), Ke3 (red), Special run with Al target (blue), and cosmic ray (black). The change in temperature was less than $\pm 1.2°C$ during 3pi0 Runs.

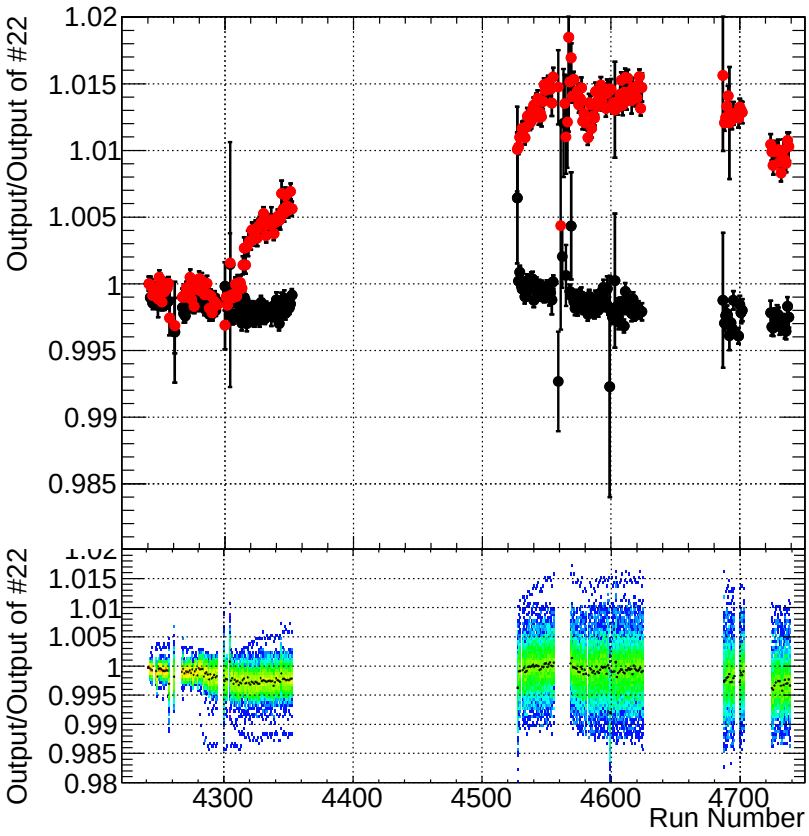

Figure 3.10: Temporal variations of pulse height ratio of the Laser event output. [TOP]Temporal variations of typical stable channel (black dots), and unstable channel (red dots). [Bottom]Temporal variations of multiple channels. Black dots represents mean value of the pulse height ratios.

Chapter 4

Initial calibration using cosmic ray events

4.1 Cosmic ray events

To keep the accuracy of the 3pi0 calibration, the calorimeter is needed to be calibrated roughly before applying the 3pi0 calibration. If the calibration is roughly calibrated with an accuracy less then 5%, the accuracy of the 3pi0 calibration is not affected by it. Cosmic ray events were used in the initial calibration to secure the initial calibration accuracy to less than 5%.

The initial calibration constants to convert ADC counts to the energies of the modules were derived from the cosmic ray events. The energy deposit of a cosmic ray is 14 MeV for a small crystal, and 28 MeV for a large crystal when it penetrates the crystal vertically. The energy deposit is calculated from $dE/dx|_{min}$=1.243 MeV/gcm^2, the density of CsI (ρ = 4.510g/cm^3), and path length within the CsI crystal for every event.

The calibration method using cosmic rays has following merits. Because the method does not require proton beam, the calibration time is not bound to the beam operation time. It can also calibrate all the channels of the calorimeter simultaneously.

There are also demerits. The first demerit is that the dE/dx of the cosmic ray depends on the energy of the cosmic ray particle. The energy of cosmic ray should be larger than 1 GeV to penetrate 2 m of CsI crystals. The dE/dx of muon increases with energy larger than 300 MeV. As the muon passes through the calorimeter, the muon loses its energy, and the energy deposit decreases. The energy deposit, calculated in the first paragraph, is not accurate. I, however, did not consider the position dependence in the initial calibration. The dependence was confirmed with the final calibration result. Another demerit using cosmic ray in the calibration is the position dependence of the light yield in the CsI crystal. The light yield depends on the hit position in a crystal as shown in Fig. 4.1. The energy deposition process between cosmic rays and the gammas from K_L decays are different. Gammas generate electromagnetic showers and deposit energy near the front surface of the calorimeter, but cosmic rays deposits energy at where it pass through. This difference gives different effective light yields for cosmic ray events and for gamma events.

4.2 Data taking

The setup for the cosmic ray trigger is shown in Chapter 2. I required the coincidence of two signals from the top and bottom cosmic ray trigger scintillators. The cosmic ray event data was collected with the beam event data simultaneously. Table 4.1 shows the number of cosmic ray

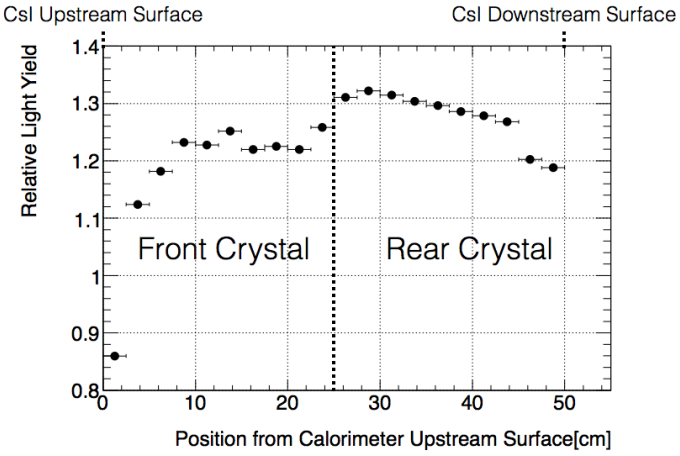

Figure 4.1: A Sample light yield distribution in the crystal ID 2511. Many crystals are made of two 25-cm-long crystals. It causes a large light yield change at the 25 cm from the CsI upstream surface. This was measured using RI source.

Table 4.1: List of cosmic ray data set.

Run Number	Data type	Total number of events
3893-3898	NA	241k
3972-4157	Ke3	270k
4161-4229	$3\pi^0$	109k
4241-4352	$3\pi^0$	259k
4361-4682	Ke3	229k
4527-4624	$3\pi^0$	222k
4687-4738	$3\pi^0$	48k

events collected during the beam time.

4.3 Cosmic ray event analysis

The incident position of a cosmic ray in a crystal is calculated from the position of triggered scintillators. In each event, I used the signals whose pulse heights were larger than 30 ADC counts in the calorimeter module; equivalent to 3 MeV. With this low threshold, accidental events, and noise were mixed in the cosmic ray events. To reduce the noise and to improve tracking accuracy, I used two tracking algorithms, the Hough transformation and the χ^2 minimization. The Hough transformation is one of line-seeking algorithms. The method converts the x and y position of CsI modules which have signals to $\rho(= x\cos\theta + y\sin\theta, -1000 < \rho < 1000$ mm) for various $\theta(0 \leqslant \theta < \pi)$. If a straight track exists, there is a peak in the $\rho-\theta$ distribution as shown in Fig. 4.2. The track is reconstructed from the ρ and θ values of the peak. The method is less sensitive to noise, but has a limited tracking precision. After Hough transformation, I removed noise hits farther than 5 cm from the track. After removing noise hits, I reanalysed the event with a pseudo-χ^2 minimization to improve tracking precision. The pseudo-χ^2 minimization

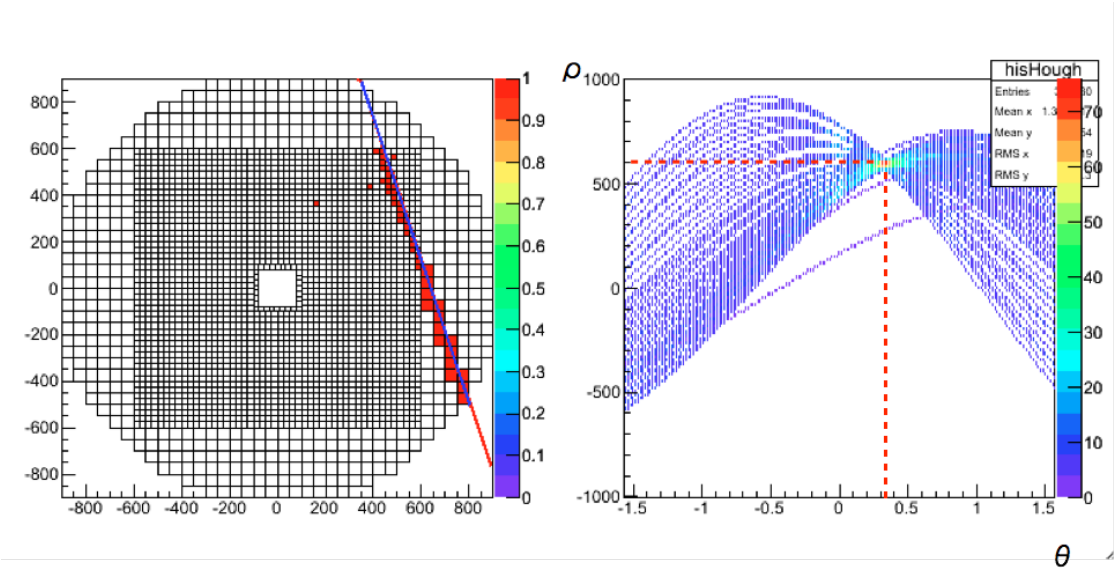

Figure 4.2: Sample of cosmic ray event before noise cut (left), and the fitting cosmic ray events using Hough transformation (right). A crossing of two dashed red line is the peak of $\rho - \theta$ distribution, and derived line is shown in the left figure as a blue line.

method uses χ^2 defined as:

$$\chi^2 = \sum_i \frac{d_i^2}{w_i^2}, \text{with} \tag{4.1}$$

$$d_i = \mathrm{x_i}\cos(\theta) + \mathrm{y_i}\sin(\theta) - \rho, \tag{4.2}$$

where i is the calorimeter module index, and w_i is the width of the module. The ρ and the θ, where χ^2 is minimized, represents the track of the cosmic ray. An example of pseudo-χ^2 minimization is shown in Fig. 4.3, and the distribution of derived ρ and θ are shown in Fig. 4.5.

After tracking, the output of each channel is normalized by the path length in the crystal and collected for each channel. The output distribution of each channel was fitted with Landau function as shown in Fig. 4.4. The peak values of the fitted Landau function and the peak of the output distributions were different by 4%, and the distribution of the difference was 1% in RMS, but this difference was not considered in the initial calibration. The ratio between the most probable value of the fitted Landau function and expected MIP energy deposit, *i.e.* 14 MeV for small and 28 MeV for large module, was set as the initial calibration constant, $\mathbf{C}^{init}$.

In the initial calibration, the initial calibration constants were aligned by changing the high voltage. The result is shown in Fig. 4.6. For most of the modules, the output of each module for the cosmic ray events was aligned to 14 MeV / 1500 ADC counts with a 3% precision. For half of the small modules whose silicone cookies were damaged, their HV were set to the applicable maximum voltage of 1750 V, to increase output. Therefore the output of cosmic ray events were not aligned, and they had wide range of values with peak at 14 MeV / 1000 ADC counts.

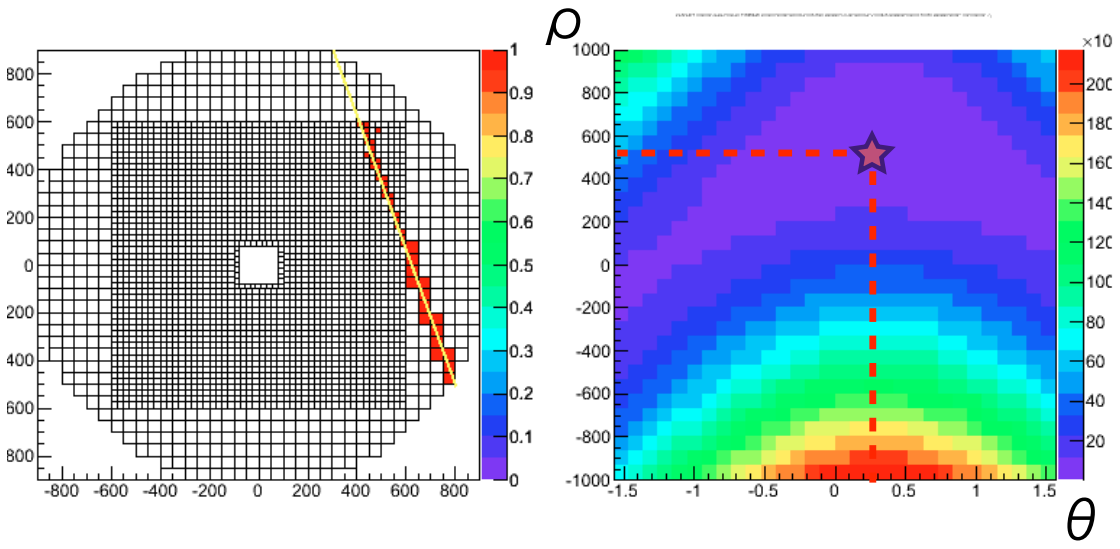

Figure 4.3: Sample of cosmic ray event (left) and the distributions of χ^2 defined in Eq. 4.1(right). The star mark in the right figure shows where χ^2 is minimum, and derived line is shown in the left figure as yellow line.

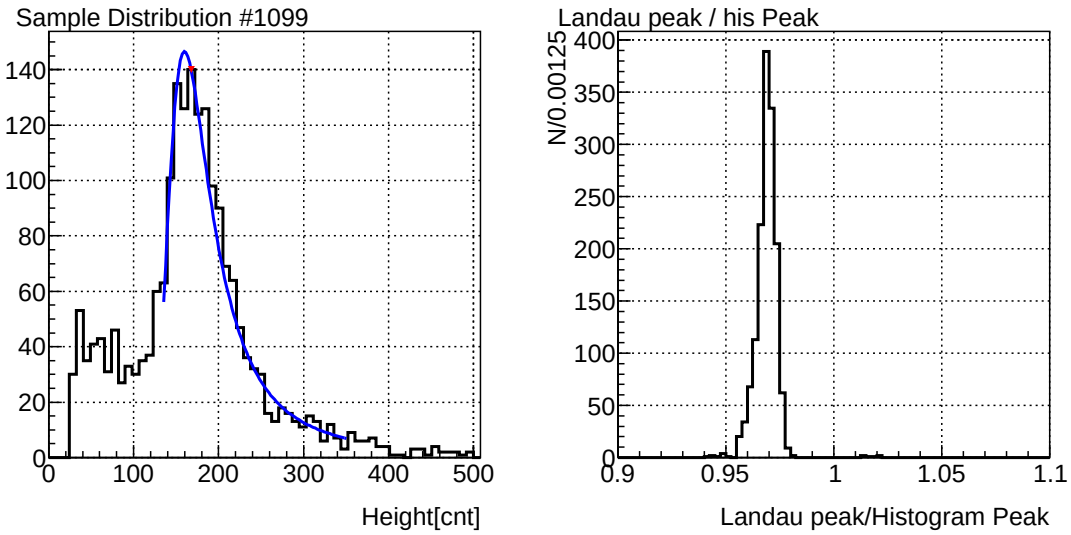

Figure 4.4: Sample of energy deposit distribution (left) and the ratio between fitted Landau peaks and peak of energy deposit distribution (right).

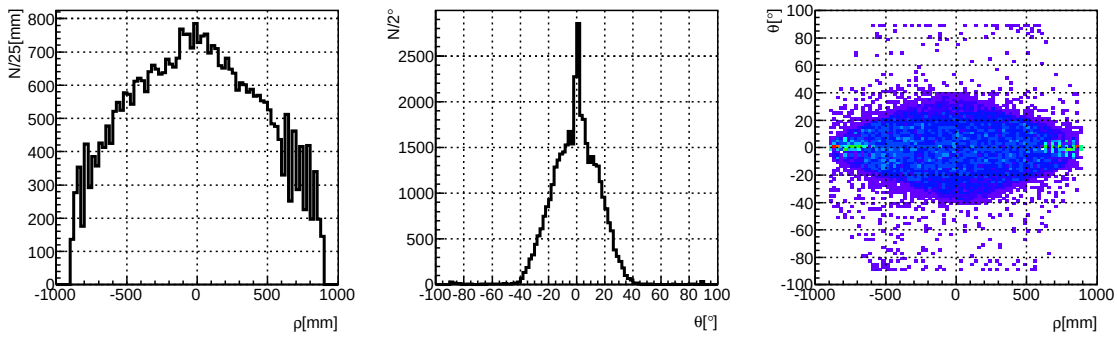

Figure 4.5: $\rho-\theta$ distributions of cosmic ray events. [Left]:Distribution of ρ from χ^2 minimization. [Middle]:θ distributions. [Right]:2D-distribution of ρ and θ.

4.4 Result

The initial calibration method for the calorimeter was established. Using two types of line-seeking algorithm, the correct cosmic ray events were collected. The initial calibration constants were derived by fitting the distribution of energy deposit with Landau function. I succeeded in calibrating all module of the calorimeter, with 241k cosmic ray events.

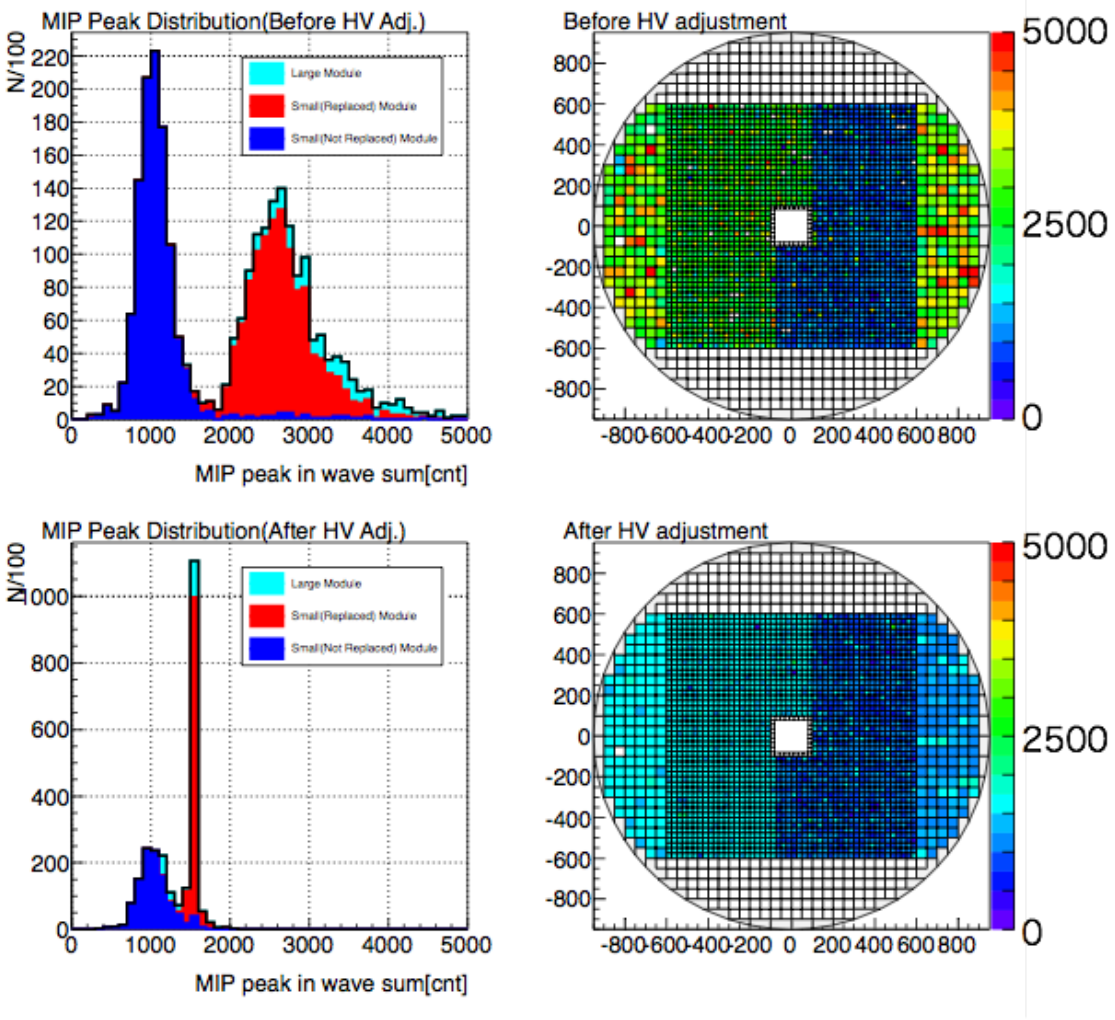

Figure 4.6: The result of cosmic ray calibration and HV adjustment. [Top left]The distribution of the peaks of fitted functions before HV adjustment. HV of all channels were set to 1750 V. The x-axis value was converted from the FADC count sum of the waveform. [Top right]The xy-distribution of peaks of MIP's energy deposit. The outputs of the modules with damaged silicone cookies are half of others. [Bottom left]The distribution of the peaks of fitted functions after HV adjustment. [Bottom right]The xy-distribution of peaks of MIP's energy deposit after HV adjustment.

Chapter 5

3pi0 calibration

5.1 Outline of the relative calibration method with $K_L \to 3\pi^0$ decay mode

To secure the performance of the calorimeter, a calibration method whose calibration accuracy is less than 1% is required. Also, the method is required to be done simultaneously with data taking. To achieve the goals, I studied a calibration method using $K_L \to 3\pi^0$ decay events.

A $K_L \to 3\pi^0$ decay event is detected as a 6 gamma event on the calorimeter. No other K_L decay modes have 6 gammas in the final state. The method uses Lagrange multiplier with kinematic parameters which are measured by the calorimeter. $K_L \to 3\pi^0$ decay events have 2 degrees of freedom that allows to calculate the energy with energies and position of other five gammas. The calibration constant is derived by using the fitted gamma energies and the initial energies of all calibration data.

To apply this method in the energy calibration, I studied its performance and features using Monte Carlo (MC) simulation data. In particular, the statistical effect on the calibration accuracy was surveyed to determine required statistics for the calibration.

The 3pi0 calibration consists of two processes, one is at the event level, and the other is at the data set level. The process at the event level is based on a kinematic fitting method using Lagrange multipliers. The process at data set level determines the calibration constant for each module by collecting the result of the event-level process. I will explain the features of the calibration method in the following sections.

5.2 Data

5.2.1 Beam event data

The section counting method described in the Section 2.2 was used to collect $K_L \to 3\pi^0$ events. The data was taken under several conditions. The summary of the beam event data used to collect the $K_L \to 3\pi^0$ events is listed in Table 5.1.

5.2.2 Monte Carlo simulation data

The MC simulation data was prepared to test the 3pi0 calibration, and to compare distributions with the beam data. A total of 2×10^{10} MC $K_L \to 3\pi^0$ decay events were generated. In the MC data, the section counting method was simulated by converting the deposit energy to pulse height using the calibration constants obtained with the initial calibration method.

Table 5.1: Data used to collect $K_L \to 3\pi^0$events. The Acpt. Ratio. shows the trigger acceptance ratio, which is (the number of accepted triggers)/(the number of requested triggers). In the trigger condition, the preset energy threshold on the L1 section, required number of hit sections in the trigger decision, and veto condition are listed. [A]:Data are used in the 3pi0 calibration test. [B]:Data used to compare the beam events and the MC events.

L1 section trigger	Charged Veto	Run Number	Beam Power	P.O.T.	Acpt.Ratio
200MeV×4section	On [A]	4161-4229	3kW	4.01E16	0.31
200MeV×4section	On [A]	4221-4227	5kW	4.79E15	0.24
150MeV×5section	On [A]	4241-4352	3kW	9.24E16	0.53
150MeV×5section	On [A]	4527-4624	3kW	7.78E16	0.52
150MeV×5section	Off [B]	4672-4738	3kW	1.75E16	0.32

5.3 $K_L \to 3\pi^0$ decay event reconstruction

In this section, I will explain the method to reconstruct $K_L \to 3\pi^0$ decay events, which is used in the calibration. The $K_L \to 3\pi^0$ reconstruction method consists of 3 steps, for gamma, π^0, and K_L. The reconstruction method for π^0 was described in the Chapter 1. Here, I will explain the method for gamma and K_L.

5.3.1 γ reconstruction

In the $K_L \to 3\pi^0$ reconstruction, the signals of the CsI modules whose deposit energies were over 3 MeV were used in the analysis. The selected signals were clustered by the scheme shown in Fig. 5.1.

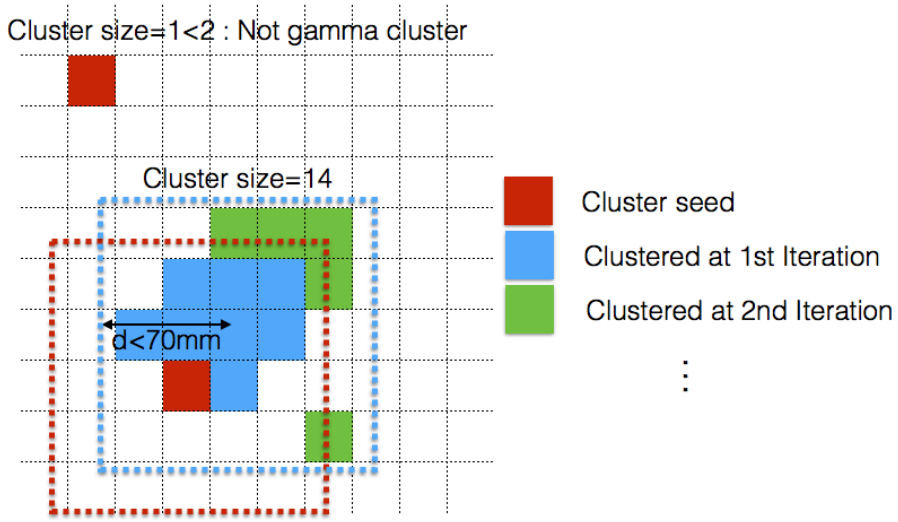

Figure 5.1: Clustering method. 1. Set a channel as a cluster seed (red in the figure). 2. Find channels (shown in blue) in the set range (red dotted square). 3. For each clustered channel, find channels (shown in green) in the set range (blue dotted square). 4. Repeat the steps 2-3 until other channels cannot be added as a clustered channel. After clustering, clusters whose sizes are larger than 1 are defined as "clusters".

The energy and position of each cluster were derived from the following equations,

$$E_{cl} = \sum_{i=0}^{i<clustersize} e_i, \tag{5.1}$$

$$x_{cl} = \frac{\sum_{i=0}^{i<clustersize} e_i x_i}{\sum e_i}, \tag{5.2}$$

$$y_{cl} = \frac{\sum_{i=0}^{i<clustersize} e_i y_i}{\sum e_i}, \tag{5.3}$$

where e_i, x_i, and y_i are the energy, x, and y positions of the i-th crystal, respectively.

The energy of cluster, E_{cl}, is different from the initial gamma energy because the modules with energy deposits less than energy threshold, $E_{th} = 3$ MeV, were ignored in the clustering. The E_{cl} was converted to gamma energy, E_γ, by

$$E_\gamma = f(E_{th}, E_{cl}, w_s, w_l) \times E_{cl}, \tag{5.4}$$

where w_s (w_l) is the fraction of energy that small (large) crystals have in E_{cl}. The energy correction function is given as [18]:

$$\begin{aligned} f(E_{th}, E_{cl}, w_s, w_l) =& 1 + w_s \times \Big(p_0 + \frac{p_1}{\sqrt{E_{cl}/1000}} - p_2 \times \log\left(E/1000\right)\Big) \\ &+ w_l \times \Big(p_3 + \frac{p_4}{\sqrt{E_{cl}/1000}} - p_5 \times \log\left(E/1000\right)\Big). \end{aligned} \tag{5.5}$$

where E and E_{cl} are in MeV. Here, $p_0 = 0.0135769$, $p_1 = 0.0516771$, $p_2 = 0.00738265$, $p_3 = -0.0200259$, $p_4 = 0.0532812$, and $p_5 = -0.00951445$, are used.

The position was corrected by the average energy deposit depth of the gamma shower, L_γ, and incident angle of the gamma, θ_γ. The L_γ is derived from another MC, and written as

$$L_\gamma = X_0 \times (p_0 + p_1 \times \log\left(E_\gamma/1000\right)). \tag{5.6}$$

Here, $X_0 = 18.5$, $p_0 = 6.49003$, and $p_1 = 0.99254$.

The position of gamma was corrected by,

$$x_\gamma = x_{cl} - L_\gamma \times \sin\theta_\gamma \times x_{cl}/\sqrt{x_{cl}^2 + y_{cl}^2}, \tag{5.7}$$

$$y_\gamma = y_{cl} - L_\gamma \times \sin\theta_\gamma \times y_{cl}/\sqrt{x_{cl}^2 + y_{cl}^2}. \tag{5.8}$$

The θ_γ is calculated in the π^0 reconstruction with the reconstructed π^0 position and x_{cl} and y_{cl}.

5.3.2 K_L resonctruction

The gammas were paired and reconstructed as π^0s as mentioned in the Section 1.3. As a result, the π^0 z vertex, vz_{π^0}, and its error, σz_{π^0}, were derived. The K_L vertex was reconstructed with informations of gammas and reconstructed π^0 as:

$$z_{K_L} = \frac{\sum_{i=0}^{i<N_{\pi^0}} vz_{i\pi^0}/\sigma^2 z_{i\pi^0}}{\sum_{i=0}^{i<N_{\pi^0}} 1/\sigma^2 z_{i\pi^0}}, \tag{5.9}$$

$$x_{K_L} = \frac{z_{K_L} - z_T}{z_{CsI} - z_T} \sum_{i=0}^{i<6} (E_{\gamma i} x_{\gamma i}) / \sum_{i=0}^{i=6} E_{\gamma i}, \tag{5.10}$$

$$y_{K_L} = \frac{z_{K_L} - z_T}{z_{CsI} - z_T} \sum_{i=0}^{i<6} (E_{\gamma i} y_{\gamma i}) / \sum_{i=0}^{i=6} E_{\gamma i}. \tag{5.11}$$

Here, z_T and z_{CsI} are the z positions of the production target and the calorimeter, respectively.

In case of 6 gamma events, there are 10 combinations to make three gamma pairs. The reconstructed K_Ls are qualified with $\chi^2_{K_L}$, which is defined as:

$$\chi^2_{K_L} = \sum_{i=0}^{i<3} (v z_{i\pi^0} - z_{K_L})^2 / \sigma^2_{z_{i\pi^0}}. \tag{5.12}$$

The combination which had minimum $\chi^2_{K_L}$ was selected as the correct combination.

5.4 Relative calibration method

5.4.1 Data selections for the relative calibration

In the energy calibration, I applied cut conditions listed in Table 5.2.

Table 5.2: Cut conditions on K_L for energy calibration.

Cut parameter	Cut value
K_L χ^2_z	< 10
Rec. KL z position	$2000 < z_{K_L} < 5000$ mm
$\lvert M_{K_L rec.} - M_{K_L PDG} \rvert$	< 10 MeV/c^2
$\lvert M_{\pi^0 rec.} - M_{\pi^0 PDG} \rvert$	< 6 MeV/c^2
Distance between gamma	> 150 mm
Gamma energy	> 100 MeV

5.4.2 Event level process

In the 3pi0 calibration, the kinematic fitting method was used [14]. In this method, one of six gammas is selected as a calibration target. The kinematic fitting method aims to determine the K_L decay position, and then to derive the energy of the selected gamma. The method uses 17 measured parameters, *i.e.* six x and y positions, and energies of five gammas which were measured by the calorimeter. The six kinematic conditions on the $K_L \to 3\pi^0$ decay, which are described later, are also used in the fitting. The energy of the selected gamma and the K_L vertex were set to be unknown, and they were derived by fitting. In the fitting, the measured parameters were allowed to change within their resolutions. The derived gamma energy was used to calculate the calibration constant, as described below.

The measured parameters and unknown values were set to vectors, $\mathbf{a_0}$ and $\mathbf{v_0}$, respectively, as:

$$\mathbf{a_0} = (x_{\gamma 1}, y_{\gamma 1}, E_{\gamma 1}, x_{\gamma 2}, y_{\gamma 2}, E_{\gamma 2}, \cdots, x_{\gamma 6}, y_{\gamma 6}), \tag{5.13}$$

$$\mathbf{v_0} = (x_{K_L}, y_{K_L}, z_{K_L}, E_{\gamma 6}). \tag{5.14}$$

Here, $x_{\gamma i}$, $y_{\gamma i}$, and $E_{\gamma i}$ are the x and y positions, and the energy of the i-th gamma, respectively. The momentum of the i-th gamma is defined as:

$$\mathbf{p}_i = \frac{\mathbf{x}_i - \mathbf{v_{K_L}}}{|\mathbf{x}_i - \mathbf{v_{K_L}}|} E_i, \tag{5.15}$$

where $\mathbf{x}_i = (x_i, y_i, z_{CsI})$, and $\mathbf{v_{K_L}} = (x_{K_L}, y_{K_L}, z_{K_L})$.

There are the six constraints on the $K_L \to 3\pi^0$ decay.

- Reconstructed π^0 mass

$$(E_{\gamma 1} + E_{\gamma 2})^2 - (\mathbf{p_1} + \mathbf{p_2})^2 - M_{\pi^0}^2 = 0 \tag{5.16}$$

$$(E_{\gamma 3} + E_{\gamma 4})^2 - (\mathbf{p_3} + \mathbf{p_4})^2 - M_{\pi^0}^2 = 0 \tag{5.17}$$

$$(E_{\gamma 5} + E_{\gamma 6})^2 - (\mathbf{p_5} + \mathbf{p_6})^2 - M_{\pi^0}^2 = 0 \tag{5.18}$$

- Reconstructed K_L mass

$$(\sum_i E_{\gamma i})^2 - (\sum_i \mathbf{p}_i)^2 - M_{K_L}^2 = 0 \tag{5.19}$$

- Center of energy

$$\sum x_i \cdot E_{\gamma i} - x_{K_L} \frac{z_{K_L} - z_T}{z_{CsI} - z_T} \cdot \sum E_{\gamma i} = 0 \tag{5.20}$$

$$\sum y_i \cdot E_{\gamma i} - y_{K_L} \frac{z_{K_L} - z_T}{z_{CsI} - z_T} \cdot \sum E_{\gamma i} = 0 \tag{5.21}$$

The equations from Eq. (5.16) to Eq. (5.21) were set as elements of vector $\mathbf{h} := (h_1, h_2, \cdots, h_6)$. With $\mathbf{a_0}$, $\mathbf{v_0}$, and $\mathbf{h}$, the following two matrices can be defined,

$$D = \frac{\partial \mathbf{h}}{\partial \mathbf{a}}|_{\mathbf{a}=\mathbf{a}_0} \tag{5.22}$$

$$E = \frac{\partial \mathbf{h}}{\partial \mathbf{v}}|_{\mathbf{v}=\mathbf{v}_0}. \tag{5.23}$$

In common case, the constraints $\mathbf{h}$ are not satisfied with the measured $\mathbf{a}_0$ and $\mathbf{v}_0$. *i.e.* $\mathbf{h}|_{\mathbf{a}=\mathbf{a}_0,\mathbf{v}=\mathbf{v}_0} \neq 0$. The fitting method aims to find the most adaptable $\mathbf{v}$ which satisfies the following equation,

$$\mathbf{h}|_{\mathbf{a}=\mathbf{a}_0,\mathbf{v}=\mathbf{v}_0} + D(\mathbf{a} - \mathbf{a}_0) + E(\mathbf{v} - \mathbf{v}_0) \approx \mathbf{0}. \tag{5.24}$$

The χ^2 defined as:

$$\chi^2 = (\mathbf{a} - \mathbf{a}_0)^t V_{\mathbf{a}_0}^{-1} (\mathbf{a} - \mathbf{a}_0) + 2\lambda^t (\mathbf{h} + D(\mathbf{a} - \mathbf{a}_0) + E(\mathbf{v} - \mathbf{v}_0)) \tag{5.25}$$

was used to evaluate the quality of the fitting. Here, λ is a vector of Lagrange multipliers, and the matrix V_{a_0} is defined as:

$$V_{a_0} = \begin{pmatrix} \sigma_{x_1}^2 & 0 & 0 & \cdots \\ 0 & \sigma_{y_1}^2 & 0 & \\ 0 & 0 & \sigma_{E_1}^2 & \\ \vdots & & & \ddots \end{pmatrix}. \tag{5.26}$$

Then, the $\mathbf{v}$ is calculated by following equations. Here, V_D and V_E are defined as $V_D = (DV_{\mathbf{a}_0}D^t)^{-1}$, and $V_E = (E^t V_D E)^{-1}$.

$$\lambda_0 = V_D(D(\mathbf{a} - \mathbf{a}_0) + \mathbf{h}) \tag{5.27}$$

$$\mathbf{v} = \mathbf{v}_0 - V_E E^t \lambda_0 \tag{5.28}$$

$$\lambda = \lambda_0 + V_D E(\mathbf{v} - \mathbf{v}_0) \tag{5.29}$$

$$\mathbf{a} = \mathbf{a}_0 - V_{\mathbf{a}_0} D^t \lambda \tag{5.30}$$

In the method, the process from Eq. (5.22) to Eq. (5.30) were repeated to find the minimum χ^2 by updating variables $\mathbf{a}_0$ and $\mathbf{v_0}$ by $\mathbf{a}$ and $\mathbf{v}$, respectively. The $\mathbf{v}$, where χ^2 is minimum, was selected as the fitting result. The 4th element of $\mathbf{v}$ gives the fitted energy of the selected gamma, and the ratio

$$\zeta = \mathbf{v}|_{min\chi^2}(4)/\mathbf{v_{0\ initial}}(4) \tag{5.31}$$

is used to derive calibration constants.

This method was applied to all 6 gammas in the $K_L \to 3\pi^0$ decay. At each end of the fitting for the selected gamma, the variables and the matrixes were refreshed before fitting the next selected gamma in the event.

5.4.3 Test of the event level process

In the event level process, the values of the measured parameters, $\mathbf{a_0}$, were updated. To determine their changes in the iteration, a following parameter was defined:

$$\Delta_{\mathbf{a}} = (\mathbf{a} - \mathbf{a_0})/\sigma_{\mathbf{a_0}}, \tag{5.32}$$

where, $\mathbf{a_0}$ is initial value of measured parameter as previous subsection, $\mathbf{a}$ is updated value in the event level process, and $\sigma_{\mathbf{a_0}}$ is the energy or position resolution of each parameter. The Δ distribution for each parameter is shown in Fig. 5.2. In the result, the changes of measured parameters are limited, but the selected gamma energy changes significantly.

To confirm that the calibration result converged to an ideal value, I tested the calibration method by changing the energy of a selected gamma within $\pm 10\%$. The energies of other gamma were not changed. The result is shown in Fig. 5.3. The fitting results converged to a value within 1% in RMS. I confirmed that the effect of the selected gamma energy is small on the fitting result. The fitting results, however, did not converge into the expected value, 1.

If a gamma energy is displaced from its true value by the energy resolution, then it affects the fitting result. I thus consider that this effect shifts the converged value away from 1. The effect is reduced by taking the average of fitting results from multiple events in the data set level process.

5.4.4 Data set level process

Data used for the test

To evaluate the features of the calibration method, I prepared MC data with various calibration constants. The calibration constants for each module was defined randomly with a gaussian with a width of 3% in σ. Each output of a CsI module was divided by its calibration constant.

Derivation of calibration constants

The calibration constant cannot be determined precisely with a single event alone. In the data set level process, the fitting method was applied to all the $K_L \to 3\pi^0$ events in the data set. The fitting results were acquired from each gamma of the $K_L \to 3\pi^0$ decays.

The fitting result should be 1, if all the modules were calibrated correctly. If some modules in the gamma cluster are mis-calibrated, ζ deviates from 1. The effect of mis-calibrated module to ζ is proportional to the deposit energy in the module on average. The module which has the largest energy deposit in the cluster has half of the cluster energy on average. I used the fitting result, ζ, as the energy correction scale factor for the module with the largest energy deposit.

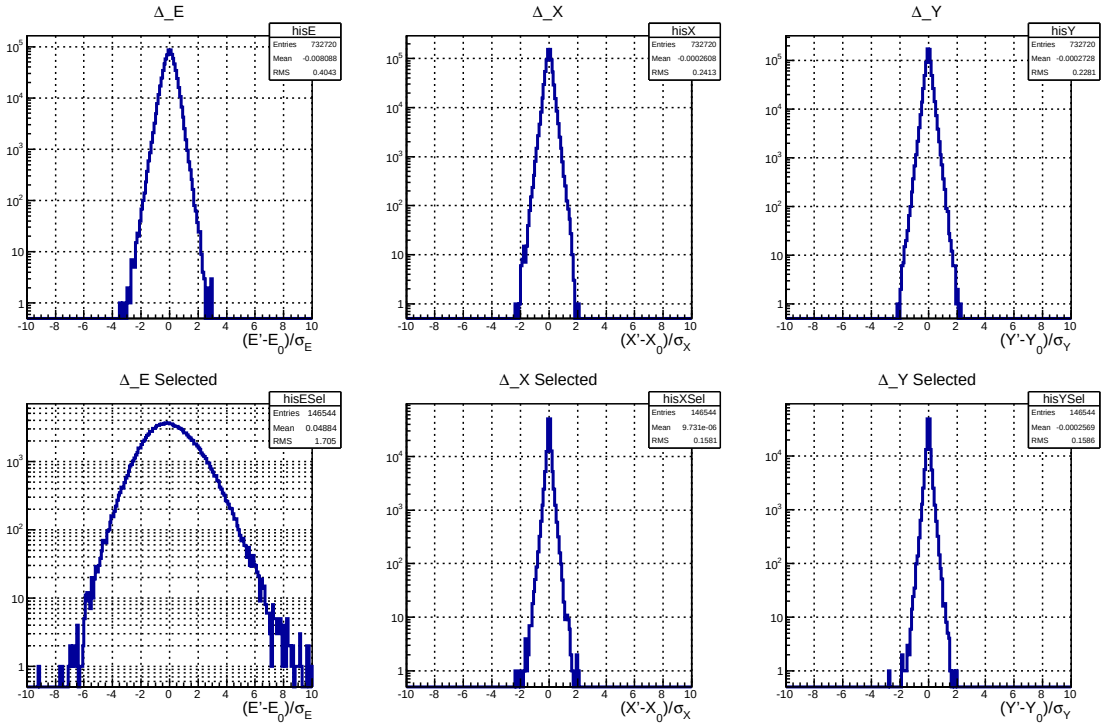

Figure 5.2: Changes of the measured parameters in the fitting. [Top, Left]Δ distributions for gamma energies. [Top, Middle]Δ distributions for gamma x position. [Top, Right]Δ distributions for gamma y position. [Bottom, Left]Δ distributions for the selected gamma energy. [Bottom, Middle]Δ distributions for x position of the selected gamma. [Bottom, Right]Δ distributions for y position of the selected gamma. The RMSs of Δ distributions were less than 1 for measured parameters, but RMS of the Δ distribution for the selected gamma energy (v(4)) was larger than other parameters.

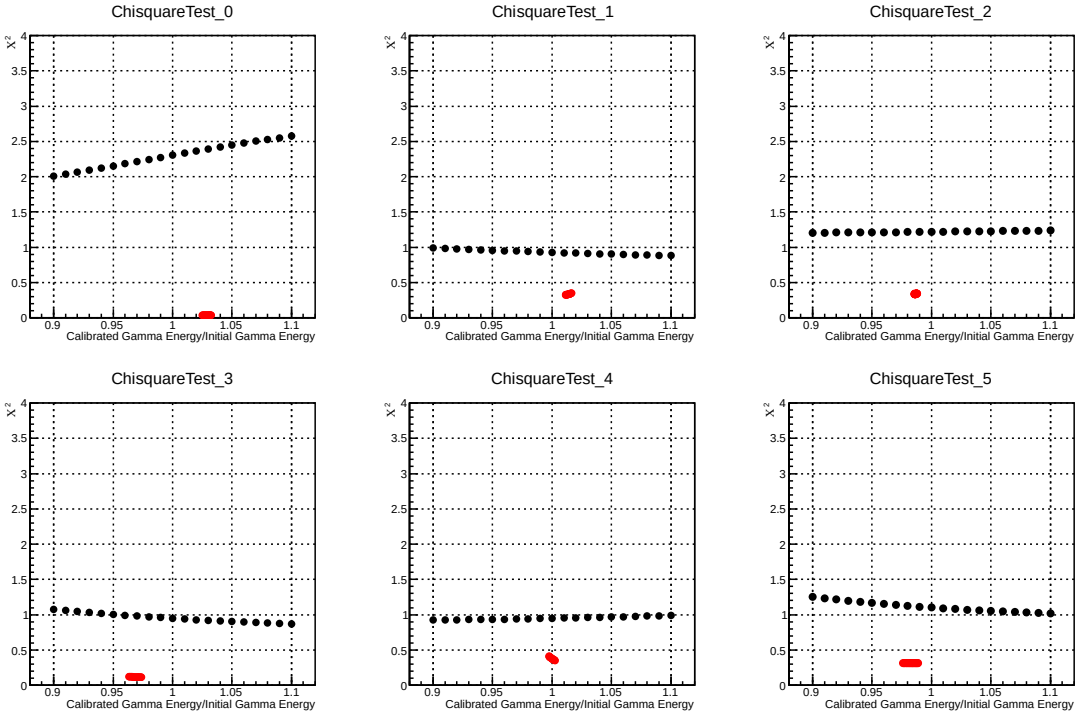

Figure 5.3: Calibration test result with a $K_L \to 3\pi^0$ event. Each plot corresponds to each gamma in the $K_L \to 3\pi^0$ decay. The black dots show the χ^2 before fitting as a function of the ratio between a changed energy and an initial energy of the selected gamma. The red dots show the ratio between a fitted energy and correct energy of a selected gamma.

The cut shown in Eq. 5.33 is applied on the largest energy deposit and other energies in the gamma cluster to restrict effect of other modules on the fitting result.

$$e_1/e_{cl} > 0.25 \ \& \ e_i/e_{cl} < 0.25. \tag{5.33}$$

Here, e_i is the i-th largest energy deposit of the cluster member module, and e_{cl} is the cluster energy. If the gamma cluster passed the cut condition, the ζ is collected into histogram for each module.

After applying the fitting method on all the $K_L \to 3\pi^0$ decay events in the calibration data set, the average of the ζs in the histogram was set as the calibration constant for the module. The relation between the number of events in the histograms and the accuracy of the calibration constant is shown in Fig. 5.4. It was surveyed for various data set sizes with the MC data. If the histogram has more than 144 events, the accuracy of the calibration constant is expected to be better than 1.5%. The calibration constant of a module is updated if its histogram has more than 144 events.

Iteration

The calibration constant of a module is affected by the calibration constants of surrounding modules. The data set level process was thus iterated until the accuracy of the calibration constants converged. The effect of iteration is shown in Fig. 5.5. In the figure, the following features of the iteration method can be found.

- The shape of ζ distribution changes to gaussian-like.

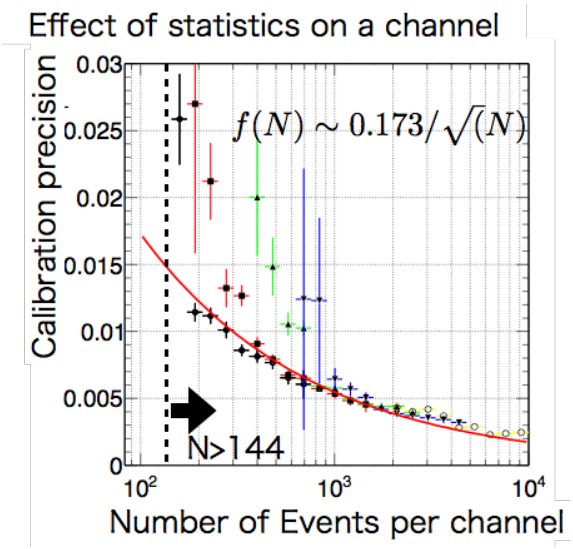

Figure 5.4: The relation between the number of the fitting result on a module and the accuracy of the derived calibration result. The different error bar colors represent different sizes of the data set.

- The change of the calibration constant is reduced by iteration.
- The number of collected ζs used for calibration increases by iteration.
- The derived calibration constant converged to a value slightly different from the true value.

Effect of iteration on the final calibration accuracy

The effect of iteration on the final calibration accuracy is evaluated by comparing the calibration constants after the n-th iteration, $\mathbf{C}^n$, for calibrated modules with the true calibration constants, $\mathbf{C}_{true}$. The RMS of the $\mathbf{C}^n/\mathbf{C}_{true}$ is defined as the accuracy of the n-th iteration. The distributions of $\mathbf{C}^n/\mathbf{C}_{true}$ and the accuracy are shown in Fig. 5.6. The calibration accuracy improved by the first several iterations. I decided to use the calibration constant of the 10th-iteration as the final calibration constant of 3pi0 calibration, $\mathbf{C}_{\mathbf{3\pi^0}}$.

5.4.5 Statistical effect on the calibration accuracy

To study how the calibration accuracy depends on the number of K_L events, I tested five cases of the number of MC K_L decay events. The relation between the number of K_L events and the final calibration accuracy is shown in Fig. 5.7. The result shows that the accuracy of the calibration is strongly related with the number of events used for the calibration. This means that if there is enough statistics, the calibration can be calibrated with accuracy less than 1%.

5.4.6 Effect of the accuracy of the initial calibration method on the final calibration accuracy

The accuracy of the initial calibration method using cosmic ray and the overall energy scale factor can affect the final calibration accuracy.

I studied the effects for various initial calibration accuracy cases, 1%, 3%, 5%, and 10%. The result is shown in Fig. 5.8. The final calibration accuracy increases by 0.35% if the

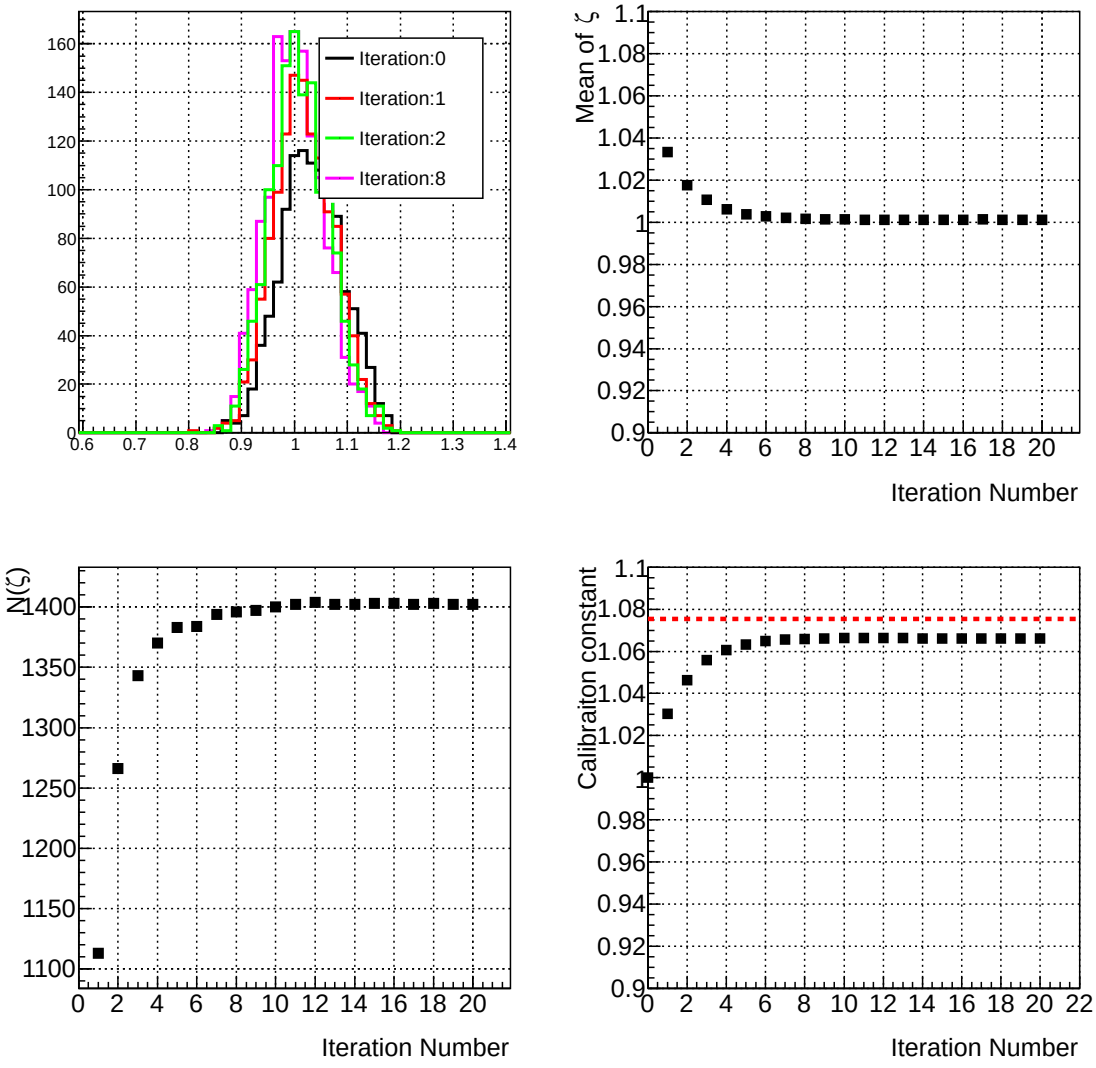

Figure 5.5: The convergence of calibration factor in a specific channel. [Top, Left]Raw distribution of ζ after different numbers of iteration. [Top, Right]The average of ζ vs the number of iterations. [Bottom, Left]The number of collected ζ in a module *vs* the number of iterations. [Bottom, Right]The number of iterations *vs* the derived calibration constant for the module. The calibration constant in the figure is normalized by the initial calibration constant.

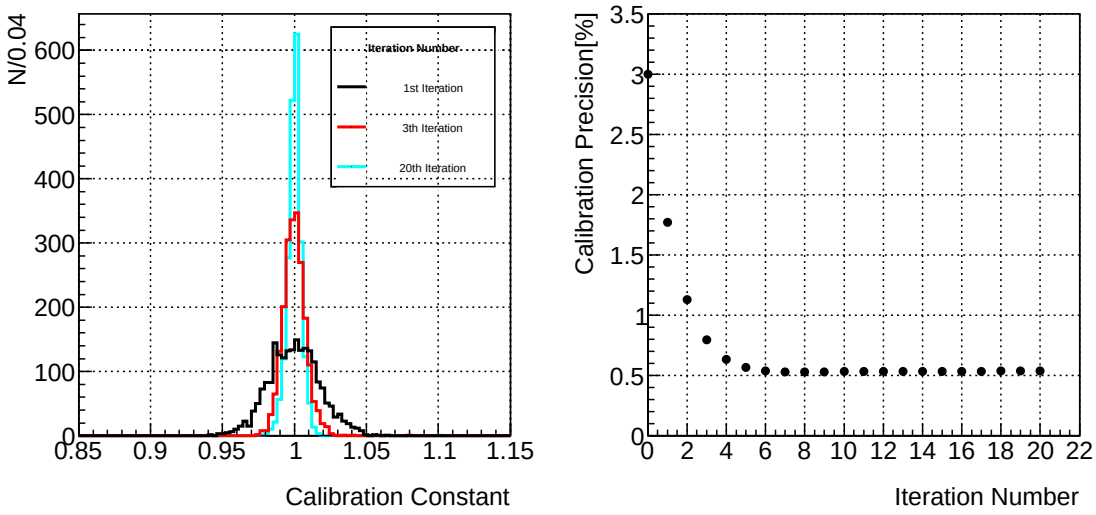

Figure 5.6: Effect of iteration on the final calibration accuracy. [Left]Distributions of the ratio between the calibration result and the ideal calibration constant is shown for different numbers of iterations (black: 1, red: 3, and blue 20). [Right]The relation of the calibration accuracy *vs* and number of iteration. After the 10th iteration, the RMS became stable at 0.54%. 2×10^9 $K_L \to 3\pi^0$ events are used for calibration. The initial calibration constant variation was 3% in RMS.

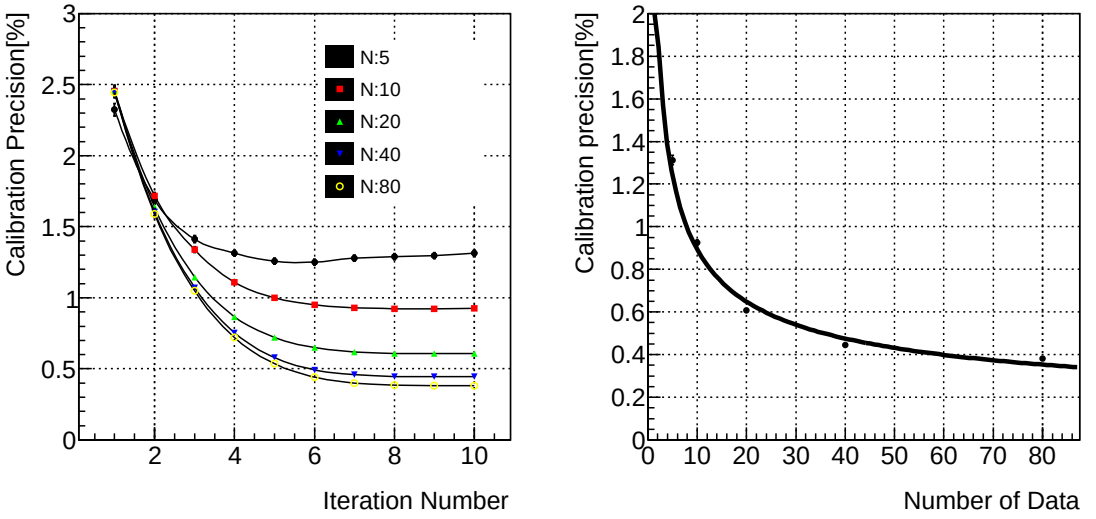

Figure 5.7: Statistical Effect on calibration accuracy. [Left]The changes of accuracy by iteration for various numbers of K_L events. Each color of point means different number of events used for the calibration (Yellow:1×10^{11} K_L, Blue:5×10^{10} K_L, Green:2.5×10^9 K_L, Red:1.3×10^9 K_L, Black:6×10^8 K_L). [Right]The relation between the final calibration result at the 10th iteration and number of K_L events. The fitted function shows that the calibration accuracy is dominated by the statistics of K_L events.

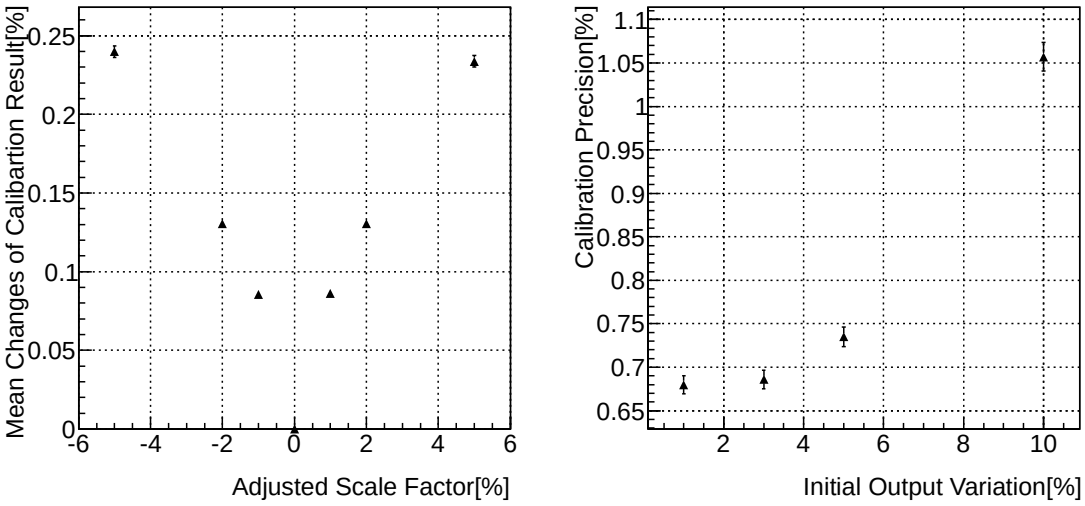

Figure 5.8: Effect of initial condition on the calibration result. [Left]Effect of overall scale factor on the calibration result. [Right]Effect of initial output variation on the calibration result. The x axis shows the RMS of initial output variation, and the y axis shows the finical calibration accuracy.

initial calibration accuracy was changed from 1% to 10%. The result shows that the calibration accuracy is not affected by the initial calibration accuracy, if the initial calibration is done with less then 3% accuracy.

I studied the effect of the energy scale factor, which cannot be calibrated with the relative calibration method. I assumed various cases of energy scale factors, ±1%, ±3%, and ±5%. The effect is evaluated with the RMS of the changes of the calibration result from the neutral case. The effect of the overall energy calibration constant is 0.24% if the overall energy scale was changed by ±5%.

With these results, I confirmed the effect of the initial calibration accuracy on the final calibration result is small compared to the final calibration accuracy.

5.5 Result of the relative calibration method

The reliabilities of the calibration method was confirmed in the previous sections.

The calibration method was applied to the beam event data. I used the data set [A] shown in Table 5.1, for calibrating the beam event data.

The calibration accuracy with the beam data was derived by using the data itself. The calibration data was divided to halves or quarters, and calibrated independently. The calibration constants from a set was divided by those from the other set, and the RMS of the ratios was divided by $\sqrt{2}$ to evaluate the calibration accuracy of a data set. The derived accuracies agreed with the expected accuracy which is derived with the MC data, as shown in Fig. 5.9.

The calibration result has a module position dependence as shown in Fig. 5.10. The calibration constant derived from the relative calibration method is smaller for the modules which is placed in lower positions. I considered that the position dependence comes from the systematic error of the initial calibration method. High energy cosmic rays deposit more energy than low energy cosmic rays above 300 MeV. Because the cosmic ray loses its energy in the calorimeter, the energy spectrum of the cosmic rays slightly depends on the module positions.

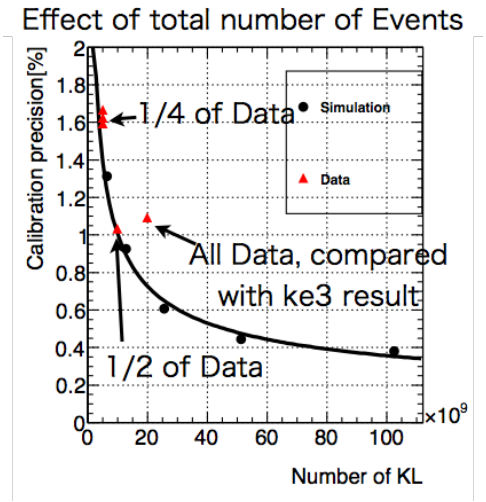

Figure 5.9: Relation between the calibration accuracy and the number of K_Ls of MC (black dots) and beam data (red triangle). The "1/4 of Data" and "1/2 of Data" show the calibration accuracy from the comparison of the calibration constants between divided data set. The "All Data" shows the RMS/$\sqrt{2}$ of the ratio between the result of 3pi0 calibration and the result of Ke3 calibration result (3pi0/Ke3).

In the MC cosmic ray event, the deposit energy on a module has a position dependence of $(1.29 \pm 0.068) \times 10^{-5}$ MeV/mm. This position dependence of MIP peak height was not considered in the initial calibration method. Therefore, the calibration constant from the relative calibration includes the position dependence. The result of the relative calibration method had $(1.30 \pm 0.29) \times 10^{-5}$ MeV/mm of y position dependence, and it was consistent with the position dependence of cosmic ray energy deposit.

The calibration constants had a module type dependence. The calibration constants of large modules were 3.2% larger than those of small modules on average. The energy deposit of cosmic ray event were also different by 3.9% between the two module types. The difference of the calibration constants by the module size (small/large) comes from systematical effect in the fitting of energy deposit distribution. Because the distribution of energy deposit changed by the thickness of the detector, the peak position of the fitted landau function depends the modules size.

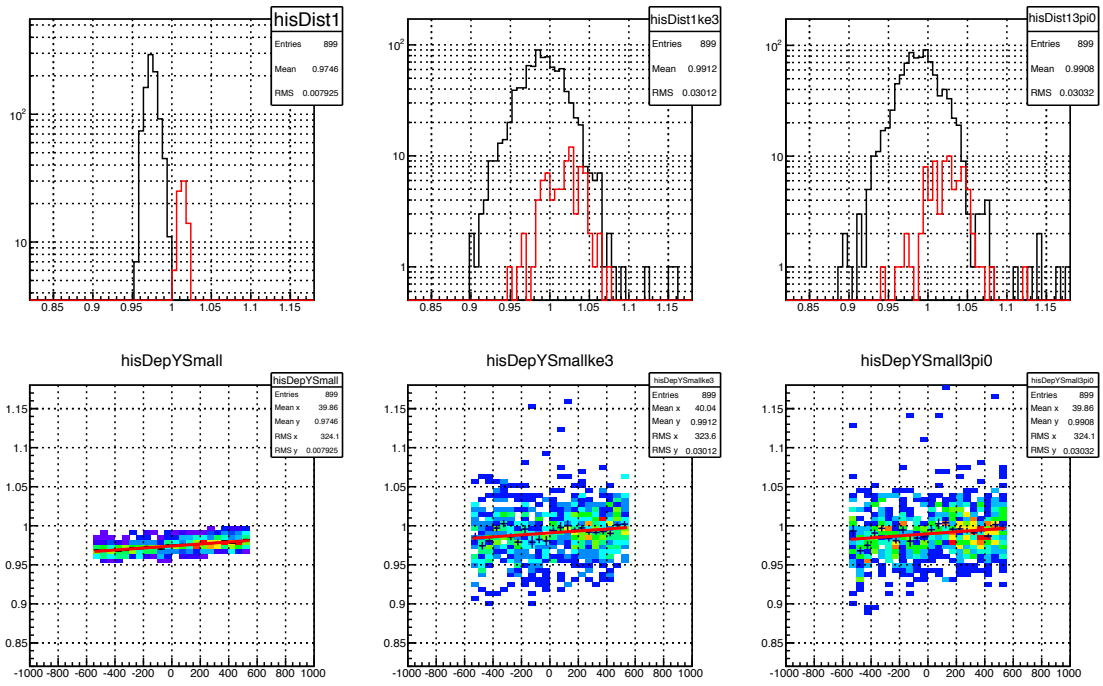

Figure 5.10: Comparison the calibration constant position distribution of small modules with other result. [Top, Left]The peak of MIP energy deposit distribution for small modules (black) and large modules (red). [Top, Middle]The distribution of the calibration constant from the Ke3 calibration method. All calibration constants are normalized by the initial calibration result. [Top, Right]The distribution of calibration constant from the relative calibration method. [Bottom, Left]The peak of MIP energy deposit distribution of modules vs module y position. [Bottom, Middle] The calibration constant from Ke3 calibration method vs module y position. [Bottom, Right]The calibration constant from relative calibration method vs module y position.

5.6 Summary

In this chapter, I confirmed the reliabilities and abilities of the 3pi0 calibration method. The accuracy of the 3pi0 calibration is affected by the accuracy of the initial calibration, but the effect is negligible if the accuracy of the initial calibration is better than 5%. The number of events used for the 3pi0 calibration dominates the accuracy of the 3pi0 calibration. The calibration constant of each channel can be derived with an accuracy less than 1% with 2×10^{10} K_Ls.

Chapter 6

Absolute energy scale calibration

6.1 Purpose and apparatus of the absolute energy scale calibration

Relative differences of the calibration constants for CsI modules are aligned by the 3pi0 calibration. However, the method cannot determine the absolute energy scale of the CsI modules, because the relative calibration method is insensitive to the energy scale as shown in the previous chapter. The reason of the insensitivity comes from the π^0 reconstruction method. In the K_L reconstruction, the π^0 is reconstructed with the equation, $m^2_{\pi^0} = 2E_1E_2(1-\cos\theta_{12})$. The π^0 decay position is determined by the energies and the positions of the two gammas with fixed π^0 mass; 134.966 MeV. If the energy scale Δ_E, which is defined as $\Delta_E \equiv E_{true}/E_{measure}$, is not equal to 1, it changes θ_{12}. In the $K_L \to 3\pi^0$ decay, for all three π^0s, each π^0 reconstruction vertex and thus the K_L decay position are shifted. There is, however, no method to find the correct θ_{12} from the given information. Therefore, as long as θ_{12} is not fixed, the gamma energy scale cannot be determined.

If the π^0 decay position is fixed, the θ_{12} is fixed automatically with gamma positions from the calorimeter. If the material is placed in the K_L beam, then the beam particles, neutrons and K_Ls, react with the nuclei of the material, and π^0 is generated. A $20\times20\times1$ cm^3 sized Al plate with a trigger scintillator was placed in the K_L beam, 2622mm upstream of the calorimeter as shown in Fig. 6.1. The reconstructed π^0 mass, m_{π^0}, can be written using Δ_E as:

$$m^2_{\pi^0} = 2E^0_1E^0_2(1-\cos\theta_{12})/\Delta^2_E \sim M^2_{\pi^0}/\Delta^2_E, \tag{6.1}$$

where E^0_i is true energy of i-th gamma and $M_{\pi^0} = 134.966$ MeV/c^2. Because the m_{π^0} is proportional to the Δ^{-1}_E, the absolute energy scale is calibrated by measuring π^0 mass with the events with 2 gammas in the calorimeter.

6.2 Data

6.2.1 KL beam event

In the trigger, I required at least 2 L1 sections with the energy sum larger than 250 MeV, in coincidence with a signal from a trigger scintillator attached on the downstream side surface of Al target. The data was taken for 3 hours in total, and 1.6×10^5 events were collected. The total P.O.T. for the energy scale calibration was 1.16×10^{15} producing 1.22×10^8 K_L.

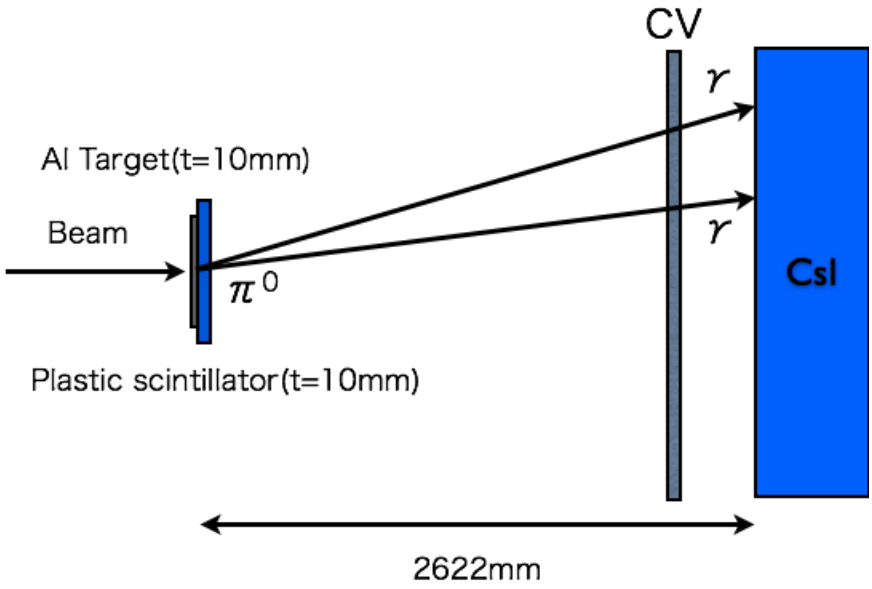

Figure 6.1: Setup of energy scale calibration run

6.2.2 Monte Carlo simulation data

Two types of MC simulation data were generated to test the energy scale calibration. The events originated from neutrons and other beam particles except K_L were generate using the beam seed generated by Geant3 beam line simulation. The K_L origin events were generated based on measured K_L flux and energy spectrum. I generated neutron and K_L MC events equivalent to 6.31×10^{14} P.O.T. and 1.91×10^{15} P.O.T., respectively. The P.O.T ratio between beam data and MC were 1.84 for neutron and 0.607 for K_L, respectively.

6.3 Comparison beam data and MC data

6.3.1 Event selection

Table 6.1: Cut values for the energy scale calibration sanalysis

Cut Parameter	Value
Number of triggered L1 Block	≥ 2
Number of gamma cluster	=2
γ position(Fiducial)	$\lvert x_\gamma \rvert > 150$ mm or $\lvert y_\gamma \rvert > 150$ mm
γ position(Fiducial)	$\sqrt{x_\gamma^2 + y_\gamma^2} < 850$ mm
γ_y	$\lvert y_\gamma \rvert < 550$ mm
E_{γ_1}	>350 MeV
E_{γ_2}	>250 MeV
χ^2_γ	<50

All cut values are listed in Table 6.1. Every cut value was determined with MC data. I required 2 gammas on the calorimeter for a π^0 reconstruction. I required the γ hit position to

be away from the beam hole and outer edge of the calorimeter by more than 10 cm. I required one gamma to have energy larger than 350 MeV, and the other to have energy larger than 250 MeV. These cut values were decided to suppress background. The distribution of the gamma energy and the reconstructed π^0 mass are shown in Fig. 6.2.

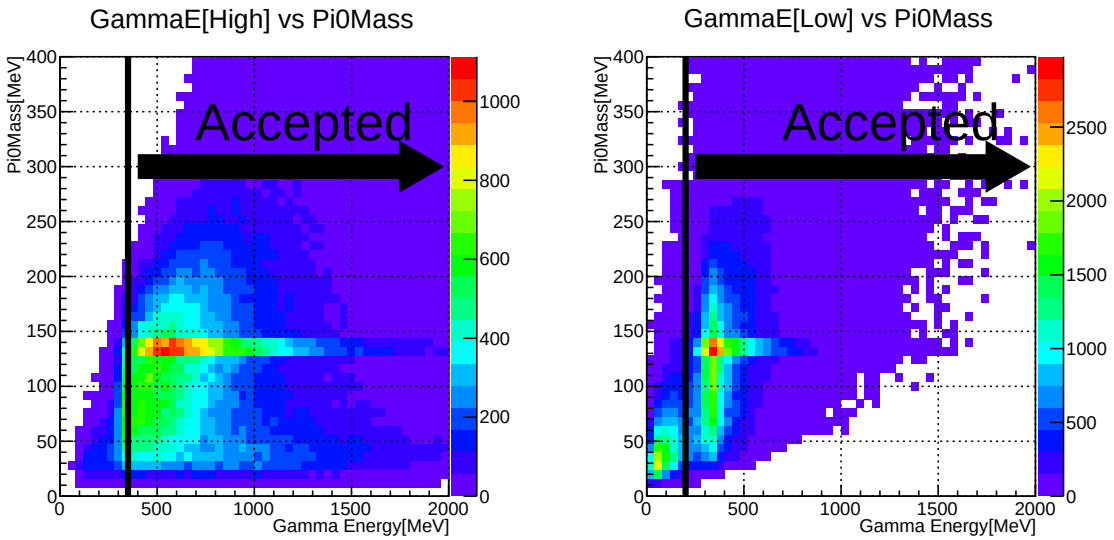

Figure 6.2: The distribution of the reconstructed π^0 mass and the gamma with larger energy (left) and smaller energy (right)

6.3.2 Comparison beam data with simulation data

The parameter distribution were compared to check the consistency between the beam event data and the MC data. For all the parameters, the ratio of the parameter distribution between the beam event and the MC event varied by 10-20%.

The distribution of the L1 section energy sum is shown in Fig. 6.3. The ratio between MC data and the beam event data fluctuates up to 20%.

The distribution of gamma hit position is shown in Fig. 6.4. The consistency between the MC data and the beam event data improved after applying all the cuts, in particular, at the central region of the calorimeter.

In case of the gamma energy distribution, the beam data was suppressed in the high energy region over 1GeV, and was enhanced in the low energy region as shown in Fig. 6.5. In case of the gamma shape χ^2 distribution, the beam data has smaller value than the MC data. This tendency was also found in the $K_L \to 3\pi^0$ event data.

The distribution of the transverse momentum of the reconstructed π^0 is shown in Fig. 6.6. In case of reconstructed π^0 mass distribution, the distributions are similar between the data sets. The ratio between the π^0 mass peak component, $|m_{\pi^0} - 134.966| < 5$ MeV/c^2, and background components, $|m_{\pi^0} - 134.966| \geq 5$ MeV/c^2, were different, but the ratio between the data and MC distributions agree within $\pm 5\%$ in the 100-200 MeV/c^2 region.

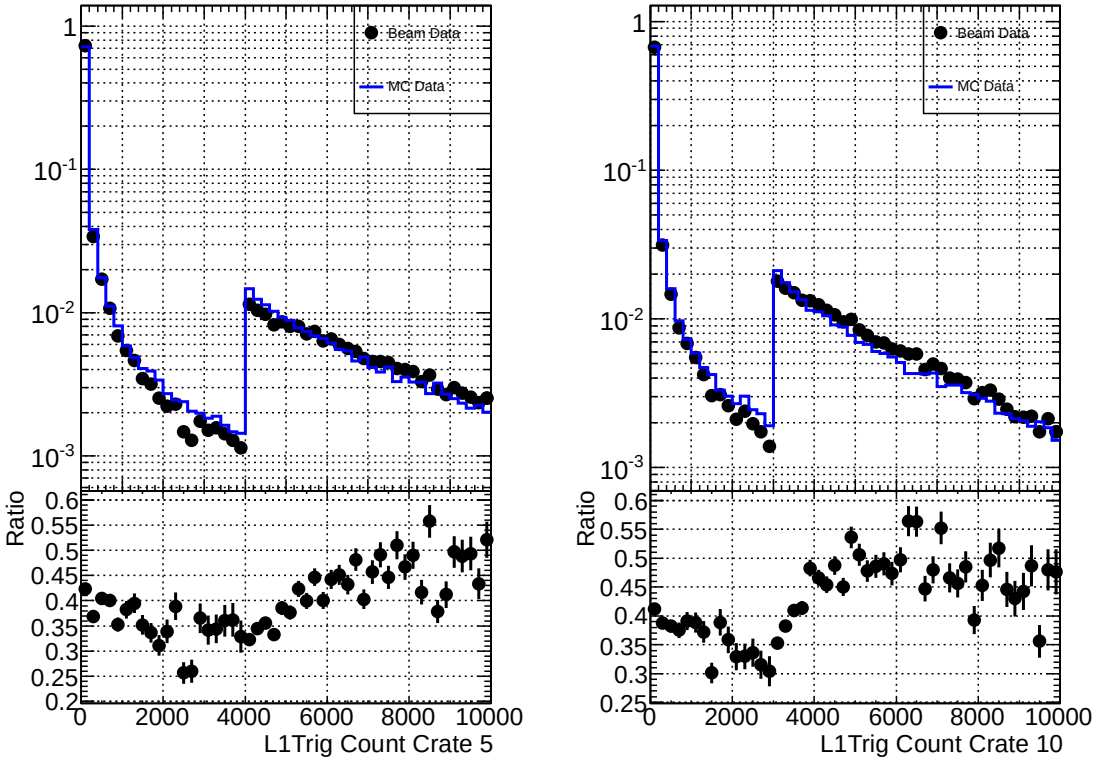

Figure 6.3: The distributions of L1 section energy sum in the energy scale calibration data. The L1 section energy sum was expressed in ADC counts, and the ratios, energy/ADC counts, were different for all sections. Therefore the thresholds for L1 sections were set by different value in ADC counts. The distribution of L1 section energy sum of section #5 (left) and section #10 (right) are shown. Black dots show beam event data, and blue lines show MC data. The section #5 was assigned for nominal small modules, and the section #10 was assigned for cookie-damaged modules.

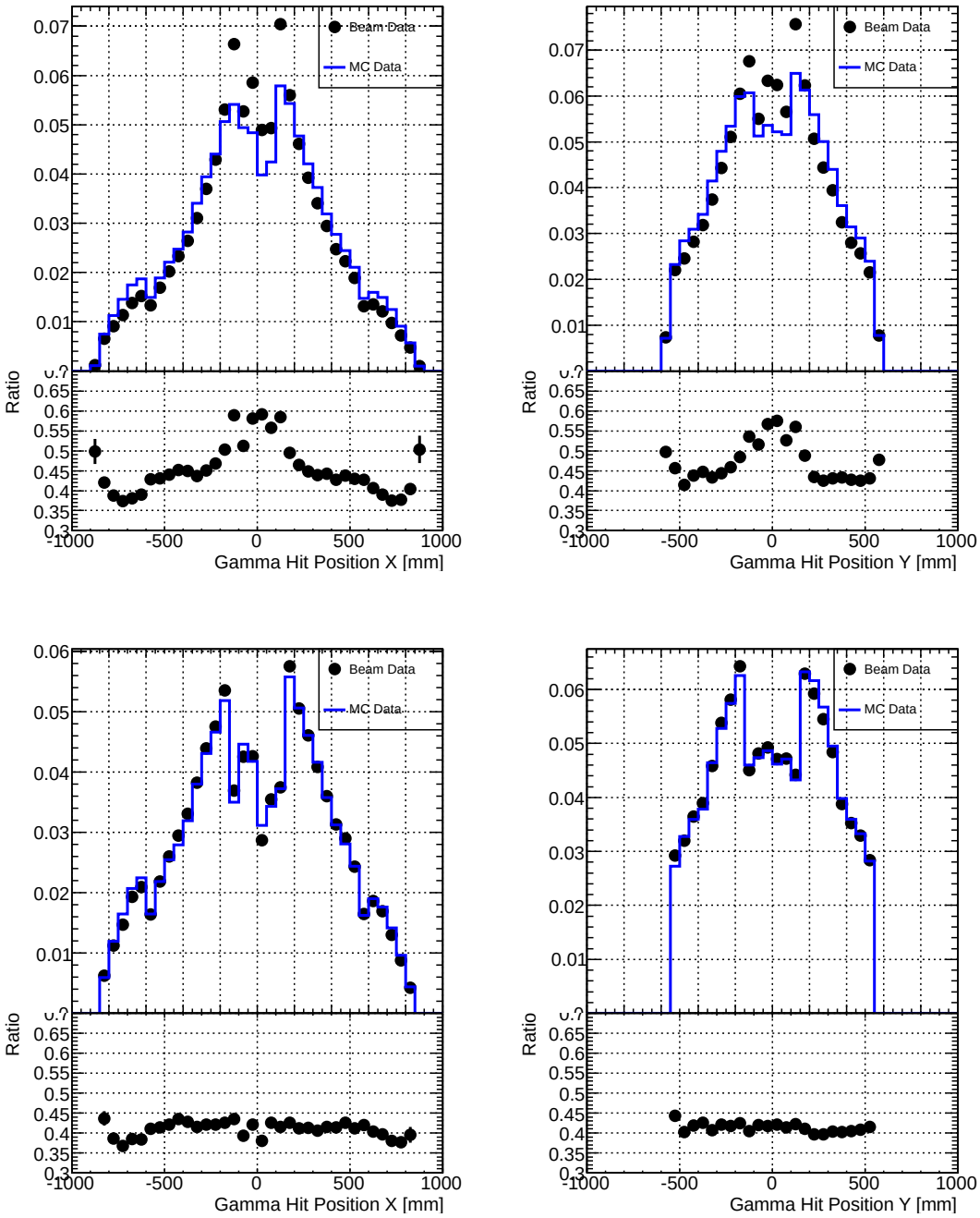

Figure 6.4: Gamma hit position of Al target run data. [Top]x (left) and y (right) distributions before applying cuts. [Bottom] x (left) and y (right) distributions after applying cuts. Black dots show beam event data, and blue lines shows MC data. The dots shown in the lower half shows the ratio between beam event data and MC data.

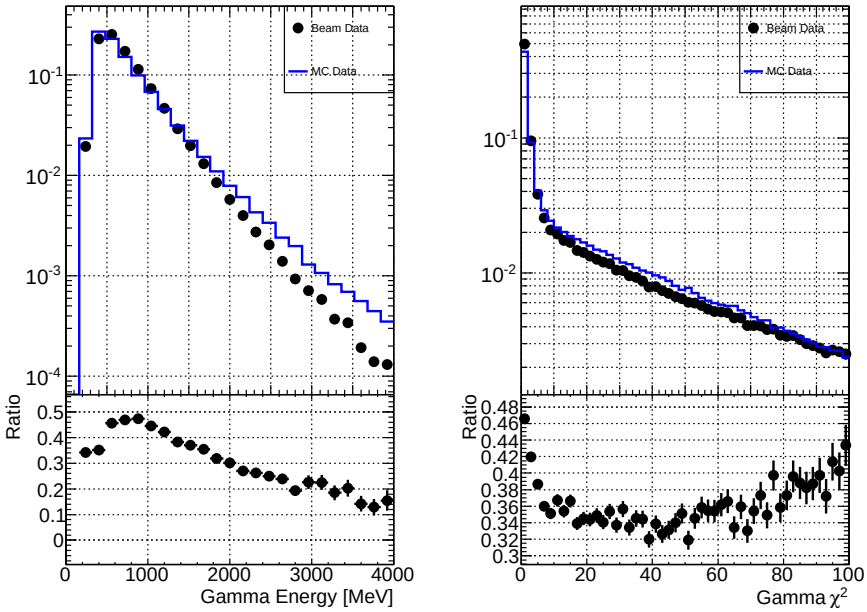

Figure 6.5: Distribution of gamma energy (left) and gamma χ^2 (right; before applying gamma χ^2 cut). Black dots show beam event data, and blue lines shows MC data. Their ratio (Data/MC) are shown in the lower half.

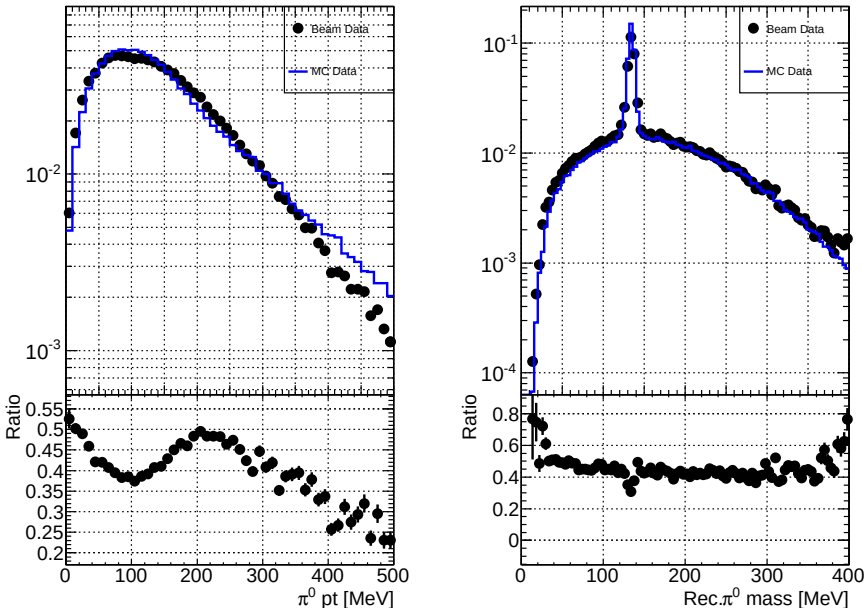

Figure 6.6: Distribution of reconstructed transverse momentum (left) and π^0 mass (right). Black dots show beam event data, and blue lines show MC data, and their ratio (Data/MC) are shown in the lower half.

6.4 Energy scale derivation

The parameter distributions from the MC and the beam events are slightly different, but the difference on the π^0 mass distribution was smaller than other distributions. I, therefore, used the MC data to test the energy scale calibration method, and to derive the energy scale.

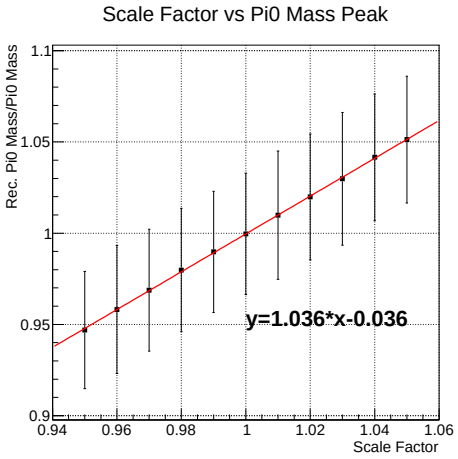

Figure 6.7: Relation between the fitted π^0 mass and the energy scale, $(1/\Delta_E)$. The error bar shows the sigma of the π^0 mass distribution.

I studied the effect of the energy scale on the reconstructed π^0 mass distribution using the MC event data. The π^0 mass was derived by fitting the π^0 mass distribution with a gaussian. The result is shown in Fig. 6.7. The derived relation was,

$$\frac{M_{\pi^0_{rec.}}}{M_{\pi^0_{rec.}|_{\Delta_E=1}}} = 1.036 \times \Delta_E^{-1} - 0.036. \tag{6.2}$$

The error in the Al plate position measurement also affects the reconstructed π^0 mass. In this case, the true value of the θ_{12} and the derived θ_{12} from π^0 reconstruction is different, then it shifts the reconstructed π^0 mass. The effect of the position mis-measurements is surveyed by changing π^0 reconstruction position in the MC data. In the MC data, the 1 cm thick Al plate was located at the 2322 mm upstream of the calorimeter, but the π^0 reconstruction position was changed from 2322-250 mm to 2322+250 mm. The dependence of the reconstructed π^0 mass on the π^0 reconstruction position is shown in Fig. 6.8. The effect of the position measurement error is estimated to be 0.36%/cm on the reconstructed π^0 mass, and the same amount on the energy scale factor. The measurement accuracy of the Al target position is expected to be less than 1 cm, because we used a Laser distance measurement equipment whose accuracy is better than 3 mm. As a result, the effect of the position measurement error on the energy scale factor is limited to less than 0.36%.

6.5 Result

The π^0 mass distribution is fitted with the function :

$$F(x) := p_0 + p_1 \times (x - p_2)^2 + \frac{p_3}{p_5\sqrt{2\pi}} \times \exp\frac{(x - p_4)^2}{2p_5^2}. \tag{6.3}$$

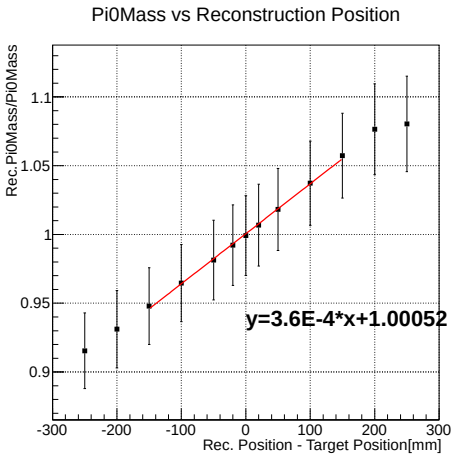

Figure 6.8: Effect of Al target position mis-measurement on π^0 mass peak value. The error var shows the width of the π^0 mass distribution.

In the function, the quadratic term was introduced to fit the background shape. The peak of the gaussian function is used as the reconstructed π^0 mass. The fitting result is shown in Fig. 6.9.

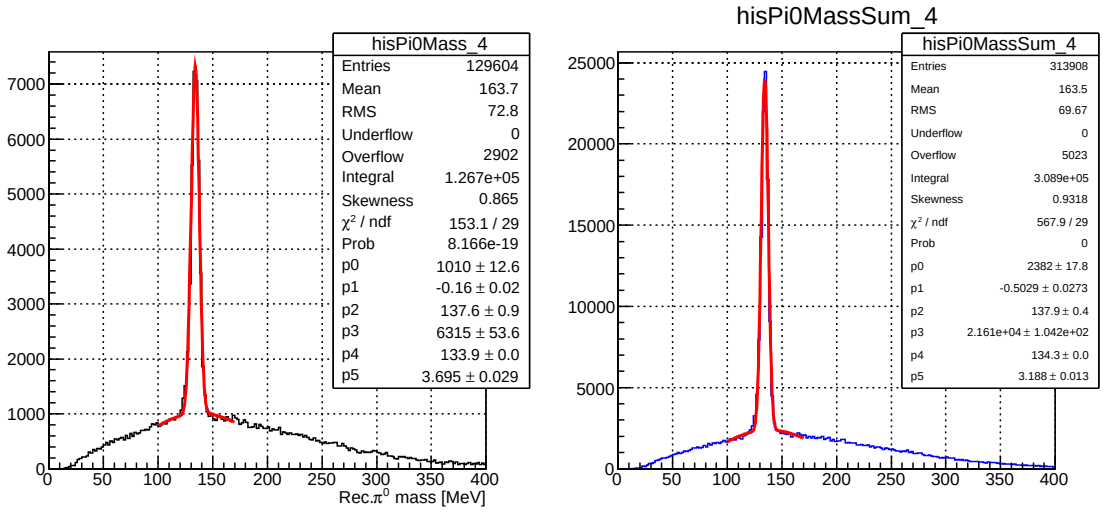

Figure 6.9: π^0 mass fitting result from the beam event data (left) and the MC data (right).

The fitted π^0 masses were 133.9 MeV/c^2 and 134.3 MeV/c^2 for the beam event data and the MC data, respectively. The overall energy scale factor, Δ_E, was derived by using Eq.6.2, and the value was 1.004.

Chapter 7

Nonlinearity correction on signal height

7.1 Nonlinearity of waveform

In the experiment, the modules with their energy deposits between 1 MeV to 2 GeV are used in the analysis. In this wide range, there are nonlinearities in the signal height. Here, the nonlinearity is defined as the ratio between the digitized FADC counts and the energy deposit in the module, and it is normalized by the ratios of low signal height region, less than 2000 counts. Such nonlinearities must be measured to correctly measure the gamma energies. The nonlinearity was measured in the past calorimeter test with a function generator. The result is shown in Fig. 3.5. The derived nonlinearity was $\sim 15\%$ at the maximum FADC counts (16000) in signal height.

The nonlinearity, however, depends on the pulse shape or the VME crate in which FADCs are seated. In this chapter, I will explain the characteristics of the nonlinearity of the calorimeter, and how to measure the nonlinearity with gammas.

7.2 Evidences of nonlinearity

The nonlinearity was determined with several methods.

The first method used the Laser monitoring system. The system can adjust the intensity of the calibration light by a factor of several hundreds for all calorimeter modules at the same time. For the laser events, a different linearity definition is used. The nonlinearity of a module, $\delta(h_i)$, at the pulse height, h_i, is defined as:

$$\delta(h_i) = \frac{h_i'/h_j'}{h_i/h_j}, \tag{7.1}$$

where h_j' and h_j are less than 4000 counts, and subscripts i and j denote module IDs of the calorimeter. The result is shown in Fig. 7.1. From this figure, following points were found.

- The nonlinearity appeared where the signal height is larger than 4000 counts. ($\sim$400 MeV)
- The nonlinearity measured with Laser is different from the nonlinearity measured with a function generator.

- The nonlinearities of small and large modules are different. This result is different from the result measured with a function generator. In the result from the function generator, the difference between modules were negligible.
- The modules whose FADC boards are in a specific crate has larger nonlinearities than other modules.

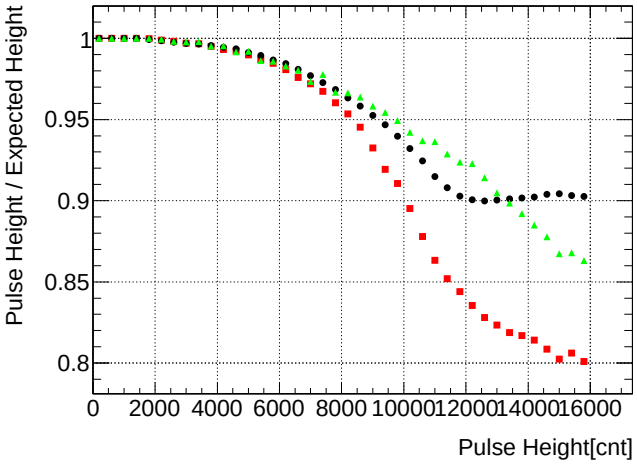

Figure 7.1: Signal height nonlinearity surveyed with the Laser Monitoring System for various modules: small modules (black), small modules where FADC are inserted in a specific VME crate (red), and large modules (green).

The second method uses $K_L \to 3\pi^0$ decays. If a π^0 has an energetic gamma over 1GeV in its decay products and there is a nonlinearity on the gamma energy of the π^0, the reconstructed decay position is shifted from the decay vertex of other π^0s. I set the average position of the two π^0 decay positions to the K_L decay position, and recalculated the mass of π^0 that has an energetic gamma. The concept is shown in Fig. 7.2. If gamma energy is shifted from its true value at high energy, the reconstructed π^0 mass with fixed decay position will be shifted from its true value, 134.966 MeV. The result is shown in Fig. 7.3. The result shows that the

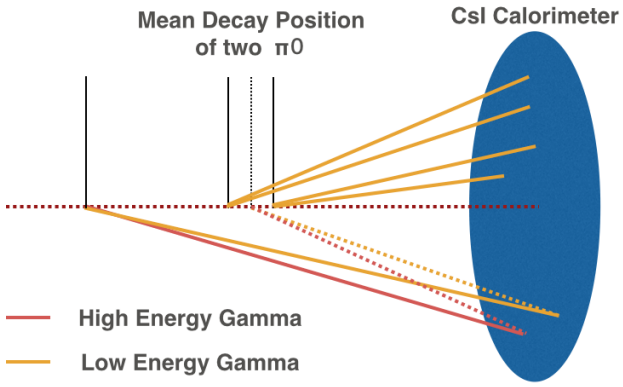

Figure 7.2: Concept of the nonliearity survey using $K_L \to 3\pi^0$ decay.

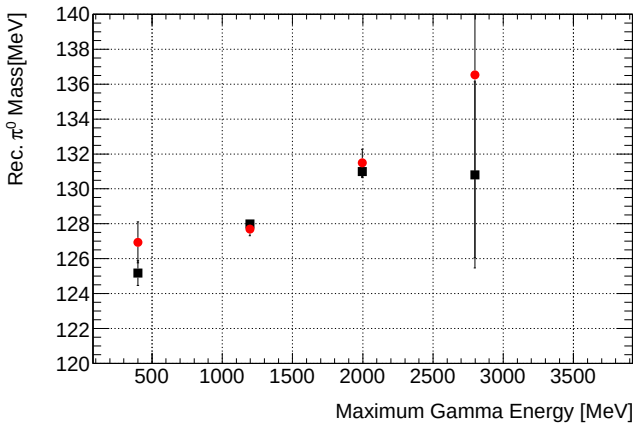

Figure 7.3: The mass of the π^0 with the largest gamma energy calculated with the averaged decay vertexes of other two π^0s, is shown as a function of the maximum gamma energy. Black dots show the MC data with no nonlinearity, and red dots show the beam event data.

nonlinearity of the MC data and the beam event data is slightly different.

The results of these methods cannot be used in the nonlinearity calibration. In case of the Laser event, the nonlinearity is different for the different pulse shape, thus, the nonlinearity from the laser event cannot be applied to the beam event nonlinearity. In case of the method using $3\pi^0$ decays, the performance of the method is not accurate enough for the nonlinearity function derivation. I decided to use the 3pi0 calibration to measure the nonlinearity.

7.2.1 Nonlinearity derivation

I tested the $3\pi^0$ calibration method for nonlinearity derivation. In the $3\pi^0$ calibration method, the calibration factor, ζ, gives the optimum gamma energy for the event. If the ζ depends on the maximum signal height of gamma clusters, it means that there is a nonlinearity in the gamma energy.

Assuming that the difference of two gamma energies only comes from the module with the largest pulse height, and other channels have no nonlinearity because they have low energies ($h_i < 4000$ counts), the nonlinearity $\delta(h)$ can be derived from Eq. 7.5.

$$\zeta = E'/E \tag{7.2}$$

$$E = \beta \times \sum_{i=1}^{n} e_i(h) \sim \beta e_1(h) + \beta \sum_{i=2}^{n} e_i \tag{7.3}$$

$$E' - E = \beta(e_1 - e_1(h)) \tag{7.4}$$

$$\delta(h) := e_1/e_1(h) = 1 + \frac{(\zeta-1)\sum_{i=2}^{n} e_i}{e_1(h)} \tag{7.5}$$

Here, $e_i(h)(e_i)$ denotes the i-th largest energy block in the gamma cluster with (without) nonlinearity, and β is an energy correction constant to convert from cluster energy to gamma energy. The parameter ζ is the calibration factor of the gamma. Event by event, the ζ has large ambiguity of about 6%, but the error on the averaged ζ is reduced by statistics.

The method was tested using a MC data. I applied nonlinearity, $\delta(h) = 1 + p \times (h/10000)^2$, on the MC data. Here, h is the pulse height, p is the nonlinearity at the 10000 counts in pulse height. Two cases of nonlinearities, p=0.02 and p=0.05, were tested. The result is shown in Fig. 7.4. The nonlinearity was derived by fitting the distribution with gaussian in multiple pulse height regions. The derived nonlinearity is shown in Fig. 7.5. The difference between

the reconstructed nonlinearity and the applied nonlinearity was less than 1% for the full height range.

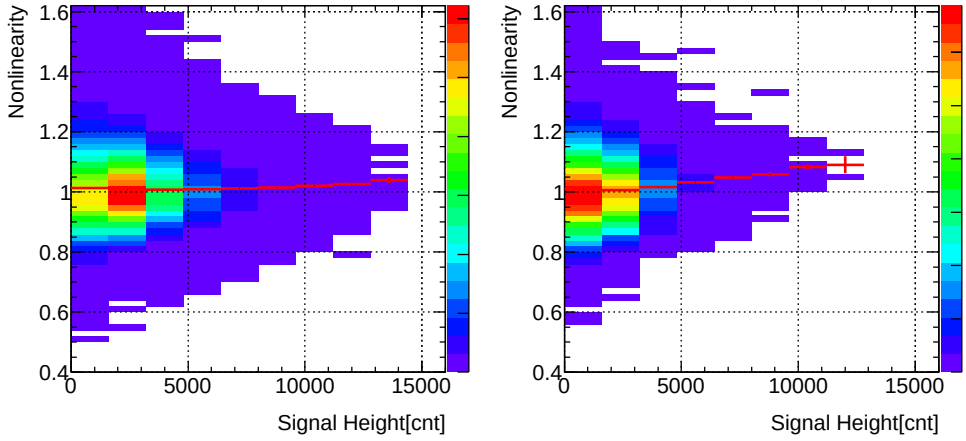

Figure 7.4: The relation of the $\delta(h)$ and the max pulse height with 2% nonlinearity (left) and 5% nonlinearity (right) assumed for all modules. Red line shows the average nonlinearity by pulse height.

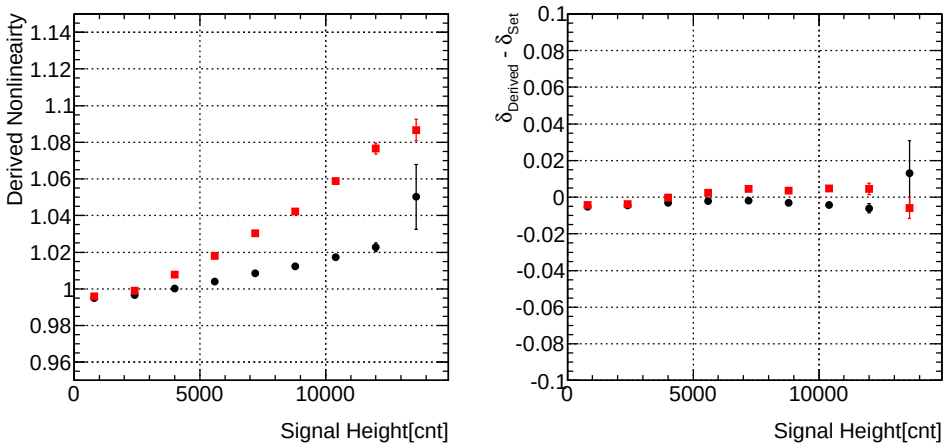

Figure 7.5: The nonlinearity derived from the MC test data for 2% (black dots) and 5% (red) nonlinearities. The left plot shows the derived nonlinearity. The right plot shows the difference between the derived nonlinearity and the applied nonlinearity.

The distributions of the calibration factor and the pulse height for MC without nonlinearity and the beam event data are shown in Fig. 7.6. The nonlinearity function was derived by slicing the distribution in pulse heights, and fitting the peak of the distributions with gaussian function. The result is shown in Fig. 7.7. The nonlinearity between measured points were interpolated with a spline curve, and the result is shown in Fig. 3.5.

The merit of this method to measure the nonlinearity is that the data can be collected simultaneously with the physics trigger. It can monitor nonlinearity during data taking. The method also has a limit. This method cannot be applied to large modules and the part of

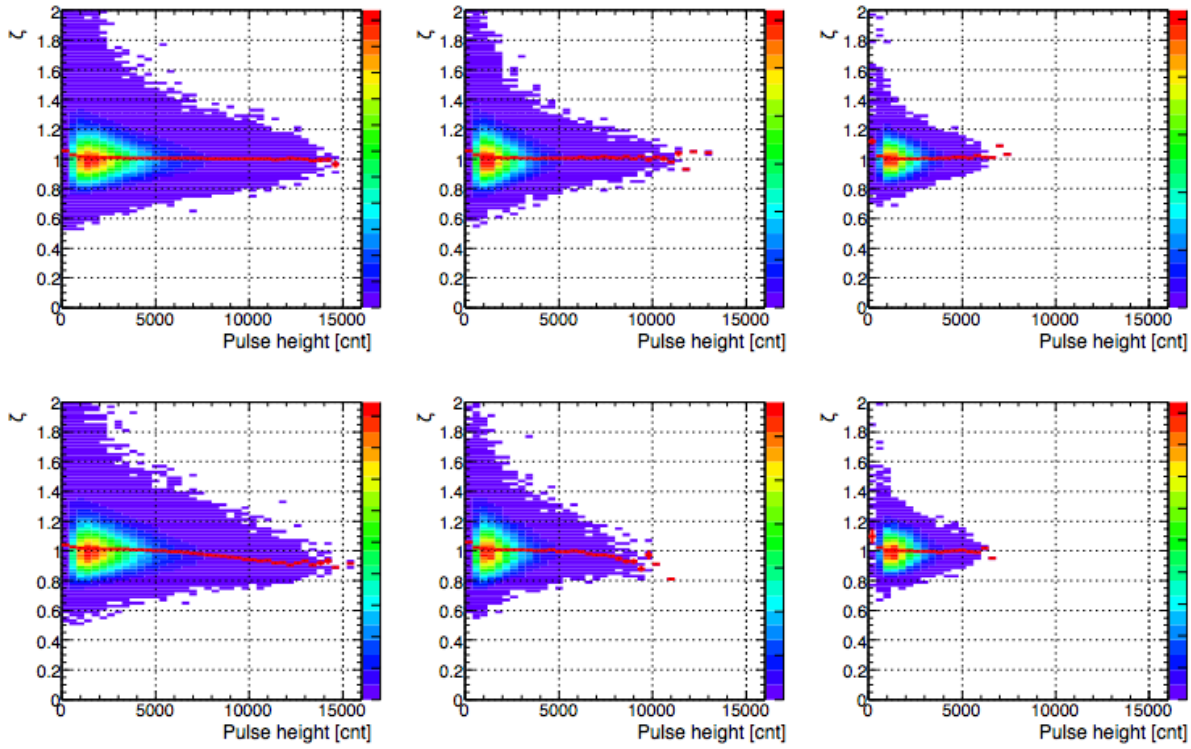

Figure 7.6: Distribution of the calibration factor and the max pulse height. [Top left] Small modules, MC. [Top middle] Small modules in crate #7, MC. [Top right] Large modules, MC. [Bottom left] Small modules, beam data. [Bottom middle] Small modules in crate #7, beam data. [Bottom right] Large modules, beam data. Red dots show the mean values of calibration factor at the pulse height.

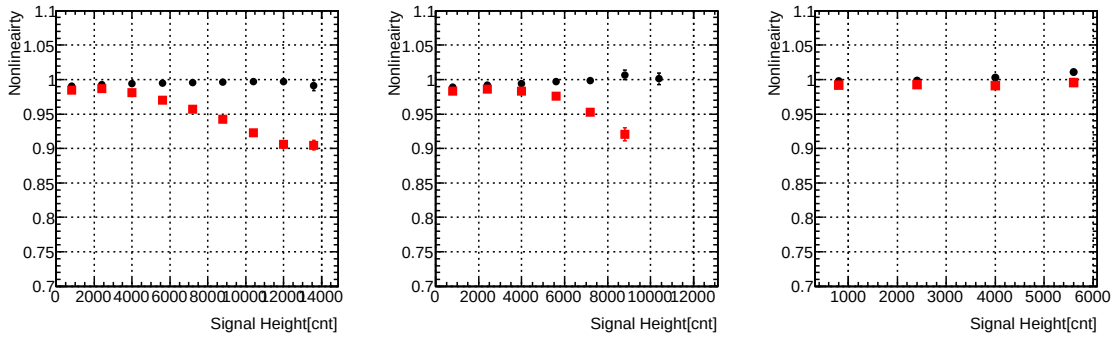

Figure 7.7: Derived nonlinearity from $3\pi^0$ calibration method for common small modules (left), specific small modules (middle), and large modules (right). Red dots represent nonlinearity from the beam data, and black dots represent nonlinearity from the MC.

small modules read out by FADCs in crate #7, because the flux and spectrum of gamma in them are limited. For these modules, the Laser monitoring system can be used to measure the nonlinearities although it gives slightly different nonlinearities from the $3\pi^0$ calibration method.

7.2.2 Nonlinearity correction result

To confirm that the derived nonlinearity function is correct, the π^0 mass peak of the energy scale calibration data was used. Ideally, the π^0 mass peak position should not depend on the signal height of each calorimeter module. The relation between the π^0 mass and the largest pulse height in gamma cluster is shown in Fig. 7.8. The mass of the beam event data has a dependence on the pulse height. In the MC data, there is no large dependence.

After applying the nonlinearity correction functions, the dependence of π^0 mass of the beam event data was reduced to $< 1\%$. For most of small modules, I used the nonlinearity correction function derived with the $3\pi^0$ calibration method. For some small modules with a large nonlinearity, and large modules, I used nonlinearity correction function derived from the Laser monitoring system.

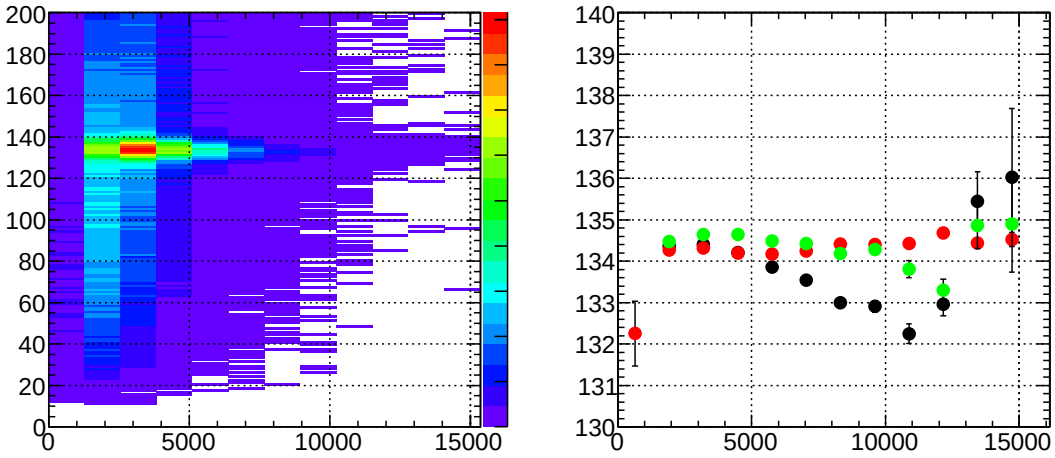

Figure 7.8: Correlation between the reconstructed π^0 mass and the maximum pulse height in the cluster. [Left]2D distribution of π^0 mass and the maximum pulse height. [Right]π^0 peak value *vs* the max pulse heights, using the ordinary nonlinearity correction function (black), the correction function derived with $3\pi^0$ calibration method(green), and MC with no nonlinearity (red).

7.3 Result

In this chapter, I explained the pulse height nonlinearity of the calorimeter module, and how to derive the nonlinearity from the various data. The result using π^0 mass shows that the nonlinearity calibration method using the kinematic fitting method with $3\pi^0$ event can calibrate the pulse height nonlinearity with a precision less than 1%. This method can monitor the nonlinearity of the calorimeter during physics data taking.

Chapter 8

Confirmation of the calibration result

8.1 Comparison beam data and MC

In this section, I will explain the effect of the calibration on the data analysis. I will show the parameter distributions of MC and beam data, and how the energy calibration changed those distributions.

8.1.1 Data

I used the $K_L \to 3\pi^0$ decay data set, which is tagged as [B] in Table 5.1. The total P.O.T. for this data set was 1.75×10^{16}, and the average DAQ acceptance ratio was 0.321. The effective P.O.T. was thus 5.6×10^{15}.

The 4×10^9 K_L decay events have been generated for the MC event data. These events correspond to 3.4 times the data set in effective P.O.T..

8.1.2 Cut conditions

Table 8.1: Cut parameters for distribution comparison.

Cut parameter	Value
Number of triggered L1 Block	> 4
$\lvert T_{event} - T_\gamma \rvert$	$<$ 5ns
The number of gamma	6
ΔT_γ	$<$2 ns
γ position(Fiducial)	$\lvert x_\gamma \rvert > 150$ mm or $\lvert y_\gamma \rvert > 150$ mm
γ position(Fiducial)	$\sqrt{x_\gamma^2 + y_\gamma^2} < 850$ mm
γ Energy	$E_\gamma >$200 MeV
$\pi^0 P_t$	< 140 MeV/c
$\chi^2_{K_L}$	< 50
K_L z position	$1500 < z_{K_L} < 5000$ mm
K_L Mass	$\lvert Rec.K_L Mass - K_L Mass \rvert < 20$ MeV/c^2

The timing of the most energy deposit in an event was defined as the timing of event, T_{event}.

The gamma timing, T_γ, is defined with the energy, e_i, and the timing, t_i, of the modules included in the gamma cluster as:

$$T_\gamma = \frac{\Sigma_i t_i \sqrt{e_i}}{\Sigma_i \sqrt{e_i}}^{1)}. \tag{8.1}$$

The timing difference between gammas is defined as:

$$\Delta T_{\gamma i} = \Sigma_i^{i \neq j} |(T_{\gamma i} - T_{\gamma j})|/5, \tag{8.2}$$

where i and j are indexes of gammas. The cuts listed in Table 8.1 are applied on the T_γ and $\Delta T_{\gamma i}$.

I also applied other cuts listed in Table 8.1 on both data sets. I required the γ hit positions to be away from the beam hole and outer edge of the calorimeter. This is because the γ energy is not reconstructed correctly if the γ hits near the boundaries. I cut on the transverse momentum of the pions, and the $\chi^2_{K_L}$, and the K_L mass.

8.1.3 Parameter distribution comparison between the MC data and the beam even data.

L1 section energy sum

The distribution of energy sum in each L1 section is shown in Fig.8.1 and Fig.8.2. For most sections, the ratios between the beam data and the MC data are flat. From the result, I determined that the hardware trigger scheme was simulated properly in the MC data.

Gamma parameters

The distribution of hit positions and energy spectrum of gammas after applying cuts on the number of triggered L1 sections, and the gamma hit positions are shown in Fig. 8.3. In the distributions, there is no large difference between the beam event data and the MC data.

π^0 parameters

Figure 8.4 shows the transverse momentum of π^0, P_t, after applying all gamma cuts. The difference between the beam data and the MC data is large at the region $P_t > 140$ MeV/c. Due to kinematics, the transverse momentum should be less than 140 MeV/c for $K_L \to 3\pi^0$ decays. However, π^0s which were reconstructed with mis-paired gammas can have higher transverse momenta. I consider that the accidental gamma is the cause of the large difference in high P_t region, because tighter timing cut reduces the high P_t events.

K_L parameters

The reconstructed z position of K_L, z_{K_L}, is shown in Fig. 8.5. The ratio between the beam data and the MC data lies within 0.85-0.95.

The $\chi^2_{K_L}$ and reconstructed K_L mass distributions after applying cuts on the transverse momentum of π^0 are shown in Fig. 8.6. Because $\chi^2_{K_L}$ distribution has a large disagreement between the beam event data and the MC data, a loose cut was applied on the $\chi^2_{K_L}$.

In case of K_L mass, the beam data has more events in the tail region than the MC data. Because the tail region is suppressed by tightening timing differences between gammas, I consider that the excess comes from accidental gammas. For a K_L flux measurement, I required that the reconstructed K_L mass is within $20 MeV/c^2$ of the nominal mass.

[1)] $\sqrt{e}$ is used as a weight to derive gamma timing temporally. To derive correct gamma timing, $\sqrt{e_i}$ should be replaced by the inverse square of the timing resolution of each module.

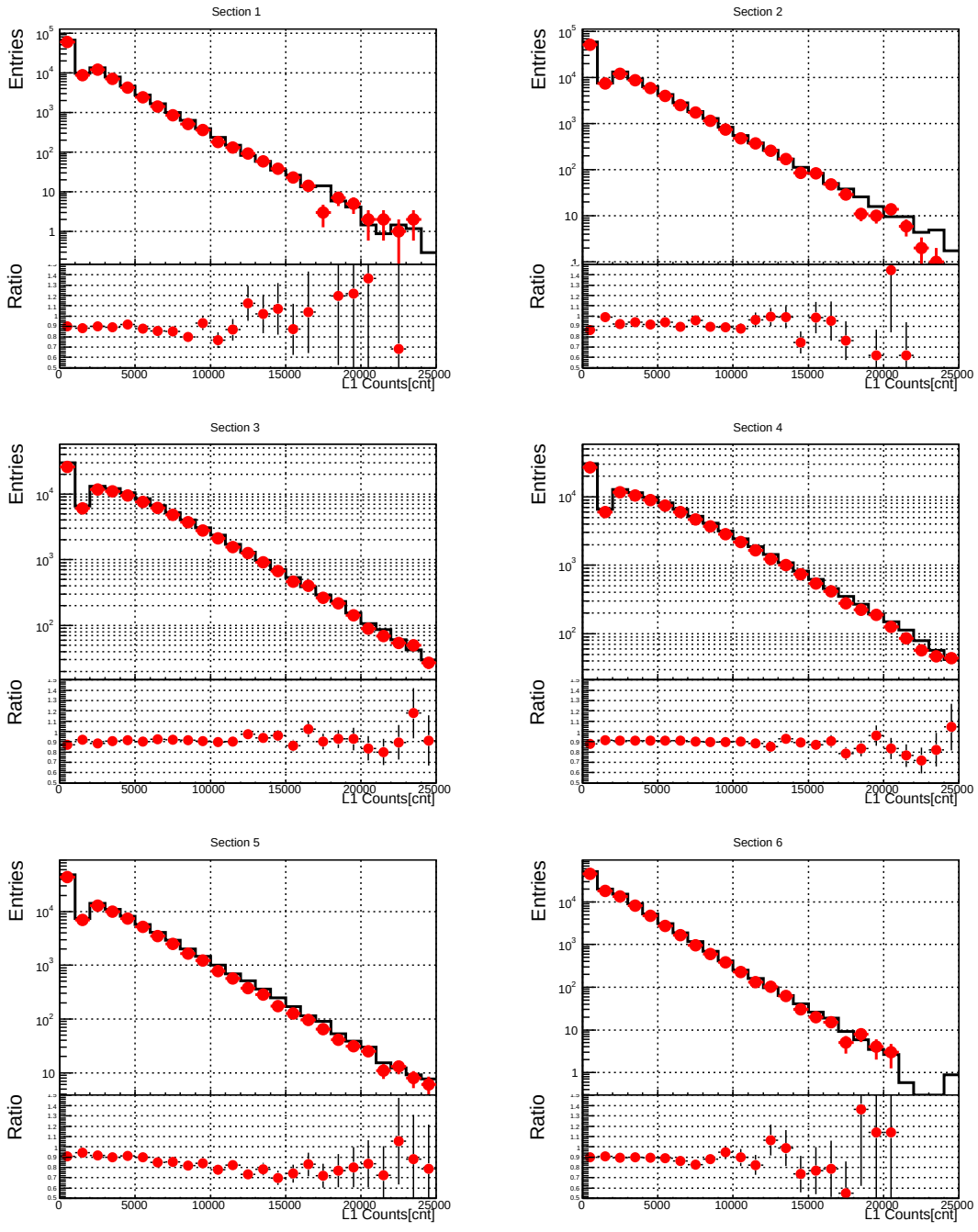

Figure 8.1: Distributions of L1 section count sum for section 1-6. The black line shows MC data, and red dots shows beam event data. The lower half shows the ratio between the two distributions (Beam/MC).

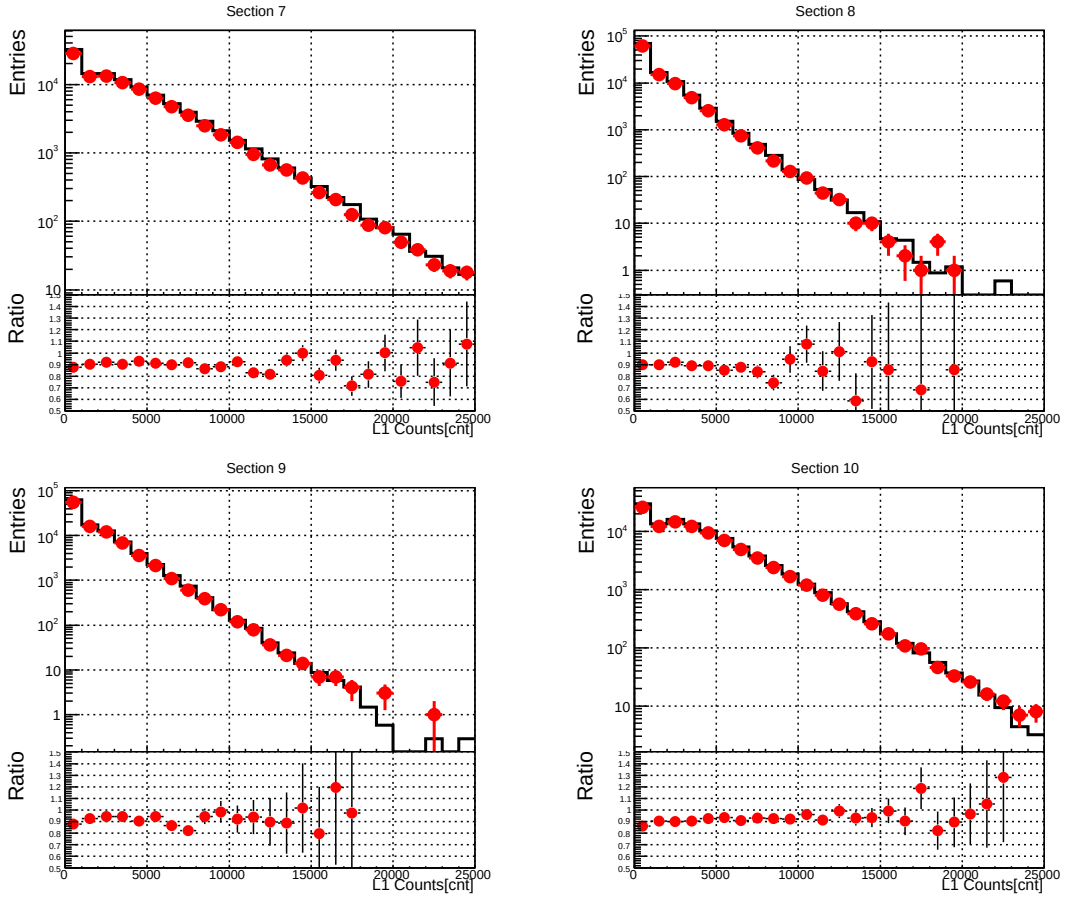

Figure 8.2: Distributions of L1 section count sum for section 7-10. The black line shows MC data, and red dots shows beam event data. The lower half shows the ratio between the two distributions (Beam/MC).

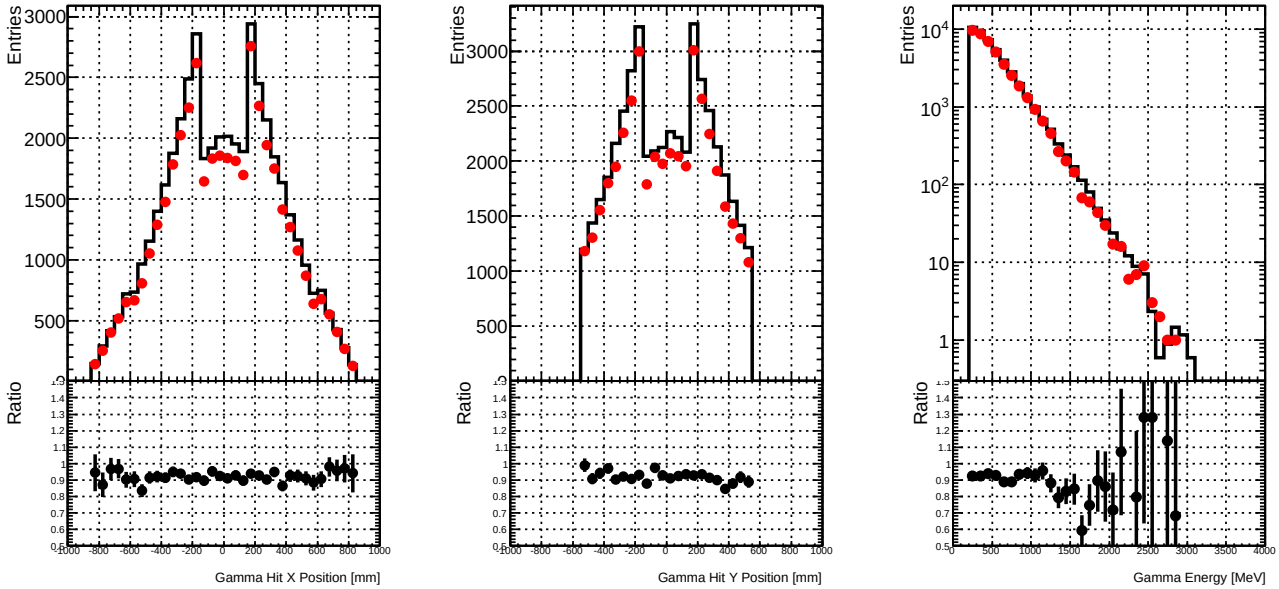

Figure 8.3: Gamma hit distributions in x (left) and y (center). The right plot shows the gamma energy. The black line and the red dots in the distributions shows the MC data and the beam data, respectively. The lower half shows the ratio between the two distributions (Beam/MC).

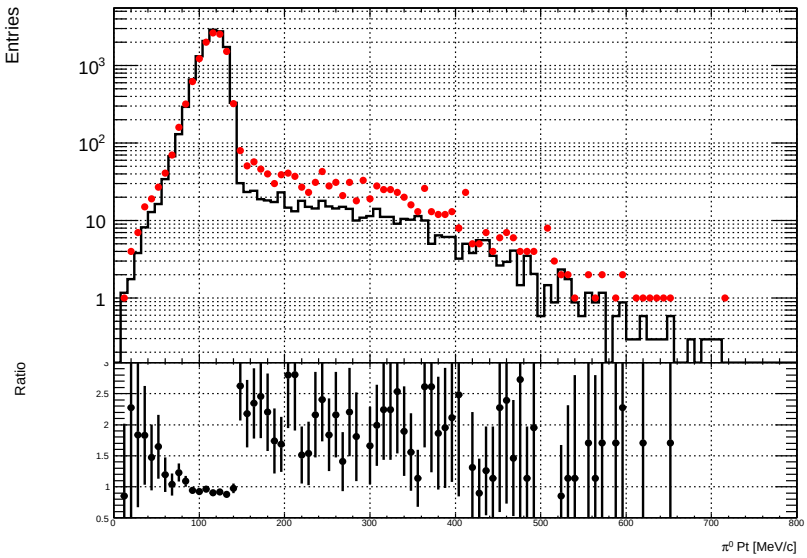

Figure 8.4: Transverse momentum distributions of π^0 after applying all gamma cuts on beam data (red dots) and MC (black solid line). The lower half shows the ratio between two distributions (Beam/MC).

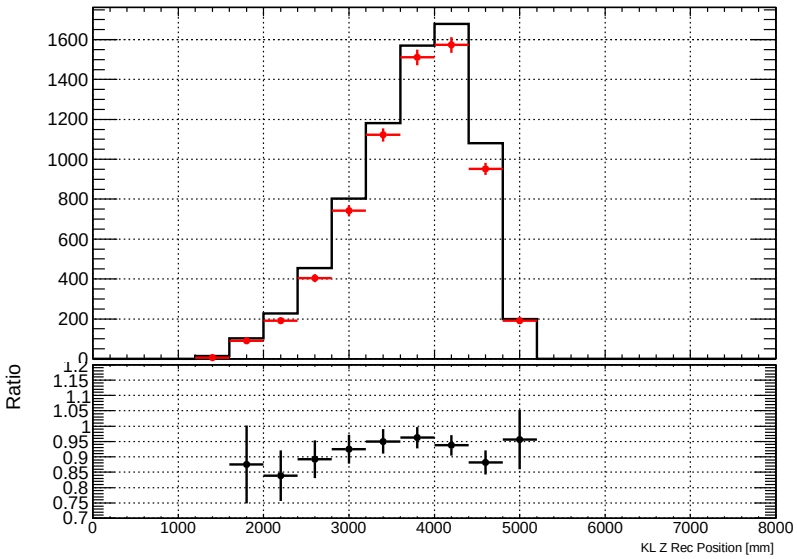

Figure 8.5: Distribution of z_{K_L} after applying all cuts. Red dots represent beam data, and black solid line represents MC. The lower half shows the ratio between two distributions (Beam/MC).

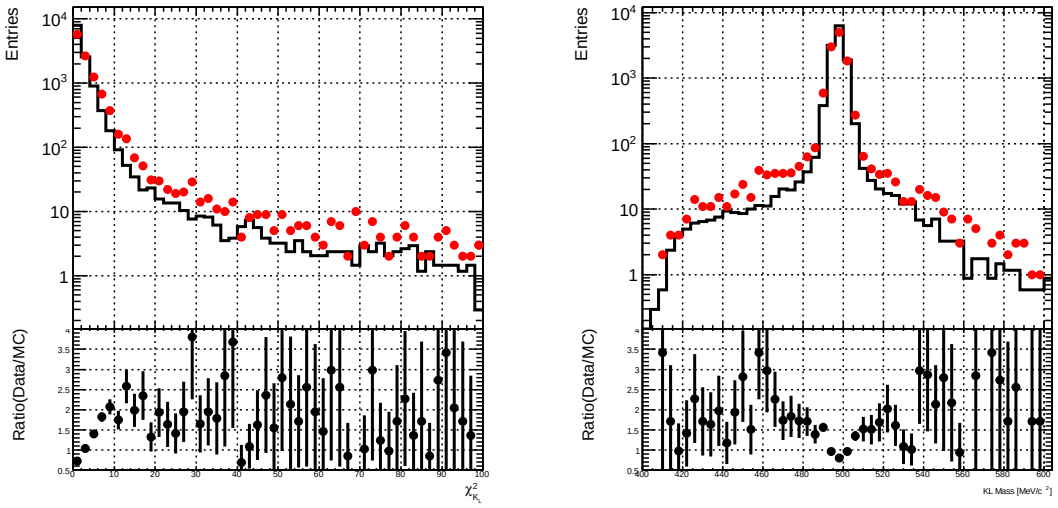

Figure 8.6: Distribution of $\chi^2_{K_L}$ (left) and reconstructed K_L mass before applying cuts on K_L parameters. The data (MC) is shown in red dots (black solid line). The lower half shows the ratio between two distributions (Beam/MC).

8.2 K_L flux

The K_L yield per P.O.T. is derived from a previous beam survey [15]. In this thesis, I used the value to scale MC data distributions. However, the ratio of number of events between the beam events and MC events is 0.277, which is 5.5% smaller than expected value, 0.293.

I consider that the accidental gammas influenced the number of reconstructed the $K_L \to 3\pi^0$ events. The accidental gamma, coming from other K_L decay or generated at the T1 target, may reduce the measured K_L flux in 2 cases. In the first case, an accidental gamma hit calorimeter simultaneously with the 6 gammas from $K_L \to 3\pi^0$ decay. In this case, the event is removed by the cut on the number of gammas. In the second case, only 5 of 6 gammas from the $K_L \to 3\pi^0$ decay and an accidental gamma hit the calorimeter simultaneously. The accidental events can be reduced by tightening the timing cut, but the number of $K_L \to 3\pi^0$ events was also reduced. To evaluate the K_L flux properly, I loosened the timing cut on ΔT_γ to 3 ns. The loose timing cut increased the rate of accidental gamma events, and decreased the number of $K_L \to 3\pi^0$ in the 6 gamma events. The effect is compensated by the number of K_L which is reconstructed with 7 gamma event. The K_L reconstruction method for 7 gammas is basically the same with the case of 6 gammas, but the only difference is that it selects 6 gammas combination from 7 gamma event which gives minimum $\chi^2_{K_L}$.

After applying all cuts, the number of 6 gamma events is 8500 in data and 30739 in MC. In case of 7 gamma event, the cut condition for the number of gamma was changed to 7, and there were 242 data events and 538 MC events. The mass distribution for each case is shown in Fig. 8.7.

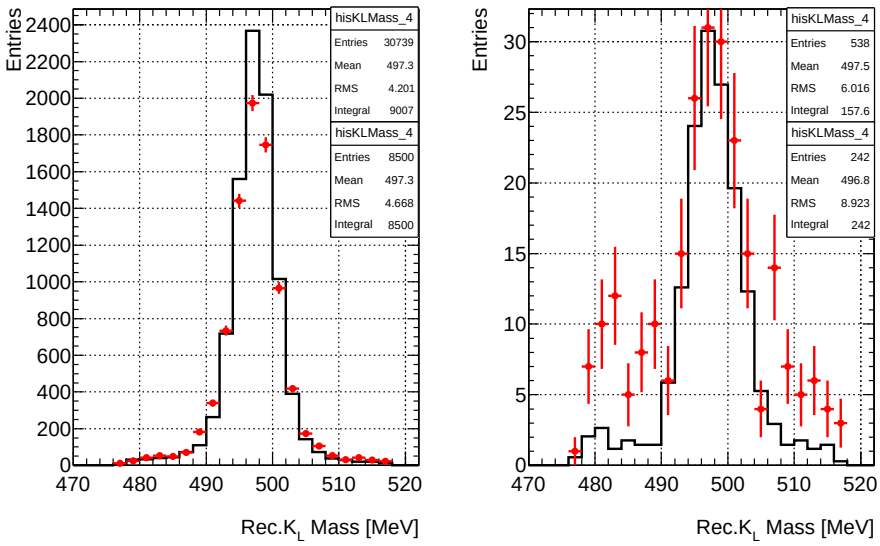

Figure 8.7: K_L mass distributions after cut. [Left]Reconstructed K_L s from 6γ events for MC data (black) and beam data (red). [Right]Reconstructed K_L s from 7 gamma events for Mc data (black) and beam data (red). The distributions from MC data is scaled by 0.293 in integral.

The number of reconstructed K_L is calculated as:

$$N_{data} = N_{data}(6\gamma) + N_{data}(7\gamma) - N_{MC}(7\gamma) \times \frac{N_{data}(6\gamma)}{N_{MC}(6\gamma)}. \tag{8.3}$$

The result was 8593, and the ratio of the number of K_Ls between beam data and MC was

calculated to be 0.280. The K_L flux from this result is $4.01 \times 10^7 K_L/2 \times 10^{14}$ P.O.T.. The derived value was 4% smaller than the measured value. The number of K_L is slightly smaller than expected, but the effects on the calibration precision is negligible.

8.3 Effects of the energy calibration

8.3.1 Effects on the gamma, π^0, and K_L

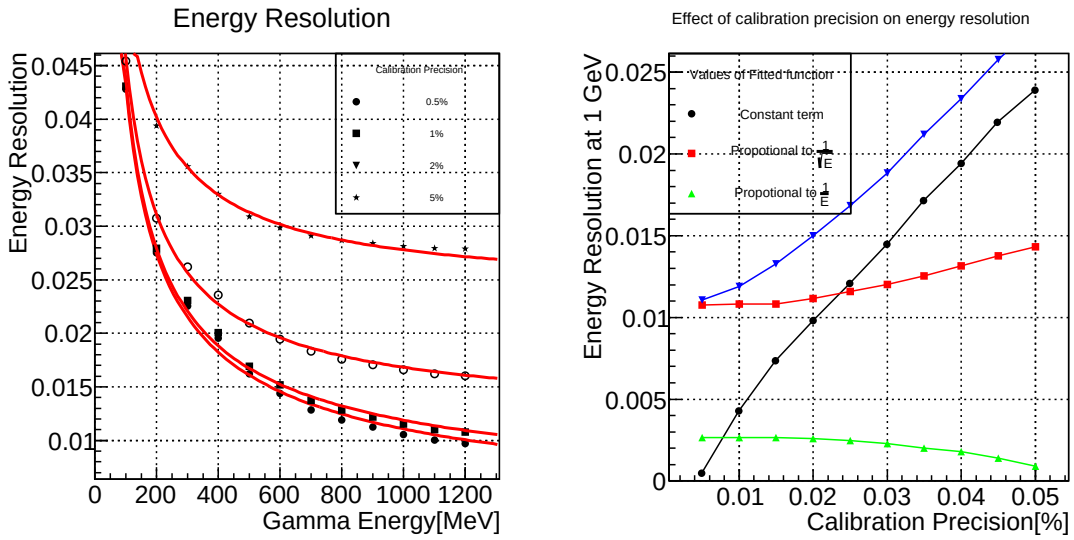

Figure 8.8: Effect of the calibration precision on the gamma energy resolution in the MC. The energy resolutions for 0.5%, 1%, 2%, and 5% of calibration precision for various gamma energies are shown on the left. The energy dependence of the energy resolution was fitted by a function, $f(E) = p_0 \oplus \frac{p_1}{\sqrt{E}} \oplus \frac{p_2}{E}$. The energy resolution at 1GeV for various calibration precision and the contributions of the fitting parameters, p_0 (black line), p_1(red line), p_2 (green line), on the energy resolution are shown on the right. The constant term (p_0) was linear with the calibration precision.

The calibration precision affects the gamma energy resolution as shown in Fig. 8.8. The gamma events were generated for various energies up to 1200 MeV, and their energies were smeared by changing the output of modules with calibration precision from 0.5% to 5%. For the ranges, the energy resolution for the 1GeV gamma changed from 1.1% to 2.7%. If the calibration is properly done, the gamma energy resolution should be improved. It is determined with the reconstructed π^0 and K_L mass distributions. I compared the reconstructed mass distributions in three cases, the MC data, the beam event data before and after applying results of $3\pi^0$ calibration and energy scale calibration. The mass distributions are shown in Fig. 8.9. The results of fitting the mass distribution with gaussian are listed in Table 8.2. The results show that the mass resolution is improved after applying all calibration results.

8.3.2 Effects on the KL beam

The energy calibration affects the reconstructed beam position. The center of energy of 6 gammas, shown in 8.4 and Eq. 8.5 are used to find the KL beam center at the calorimeter

Table 8.2: Fitting result for π^0 and K_L mass distributions with gaussian function. The units of numbers are in MeV/c^2.

Data type	Rec. π^0 mass	$\sigma_{m_{\pi^0}}$	Rec.K_L mass	$\sigma_{m_{K_L}}$
MC	135.06 ± 0.02	2.88 ± 0.03	497.49 ± 0.04	3.09 ± 0.03
Data(Before applying Cal. result)	135.05 ± 0.04	3.63 ± 0.06	497.09 ± 0.05	3.66 ± 0.05
Data(After applying Cal. result)	135.06 ± 0.03	2.94 ± 0.03	497.40 ± 0.04	3.15 ± 0.04

surface.

$$x_{c.o.e} = \frac{\sum_{i=1}^{6} x_{\gamma i} E_{\gamma i}}{\sum_{i=1}^{6} E_{\gamma i}} \tag{8.4}$$

$$y_{c.o.e} = \frac{\sum_{i=1}^{6} y_{\gamma i} E_{\gamma i}}{\sum_{i=1}^{6} E_{\gamma i}} \tag{8.5}$$

Before applying the $3\pi^0$ calibration results, the average value of $x_{c.o.e}$ and $y_{c.o.e}$ of the beam event data were at -3.7 mm and -5.8 mm, respectively. After applying the $3\pi^0$ calibration result, the center of $x_{c.o.e}$ and $y_{c.o.e}$ changed to 0.2 mm and -4.6 mm, respectively. In the data taking, the beam was only shifted to -5 mm in y. This result shows that the beam position can be corrected by the energy calibration.

8.4 Comparison of the calibration constants with Ke3 calibration result

I compared my calibration result and the result of the Ke3 calibration result. The Ke3 calibration result was derived by using a ratio of energies and momenta of electrons from $K_L \to \pi^{\pm} e^{\mp} \nu_e$ decay. The energies are measured by the calorimeter, and the momenta are measured by the spectrometer. The Ke3 calibration method is explained in the Appendix A.

The correlation and the ratio distribution of the calibration results between my calibration using $K_L \to 3\pi^0$ decays and the Ke3 calibration are shown in Fig. 8.11. The two calibration results matched less than 0.2% in the mean value, and 1.6% in width. With this result, I confirmed that the energy scale calibration was done properly.

8.5 Summary

In this chapter, I studied the effects of the energy calibration on the parameter distributions. The parameter distributions of the MC data and the beam event data agreed better after applying calibration result. This result shows that the calibration was successfully done.

In addition, I measured the K_L flux, and showed that it is consistent with the previous measurement result. I also showed that the reconstructed beam position is corrected by the energy calibration.

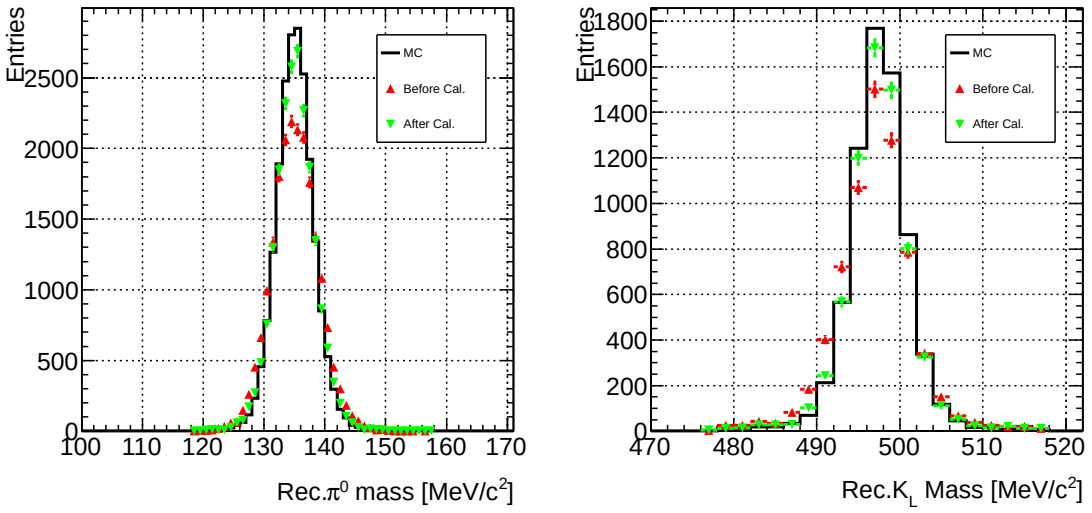

Figure 8.9: Reconstructed mass distribution of π^0 (left) and K_L(right). The distribution from the MC (black solid line), and beam data before (red triangle) and after (green triangle) applying calibration results are shown.

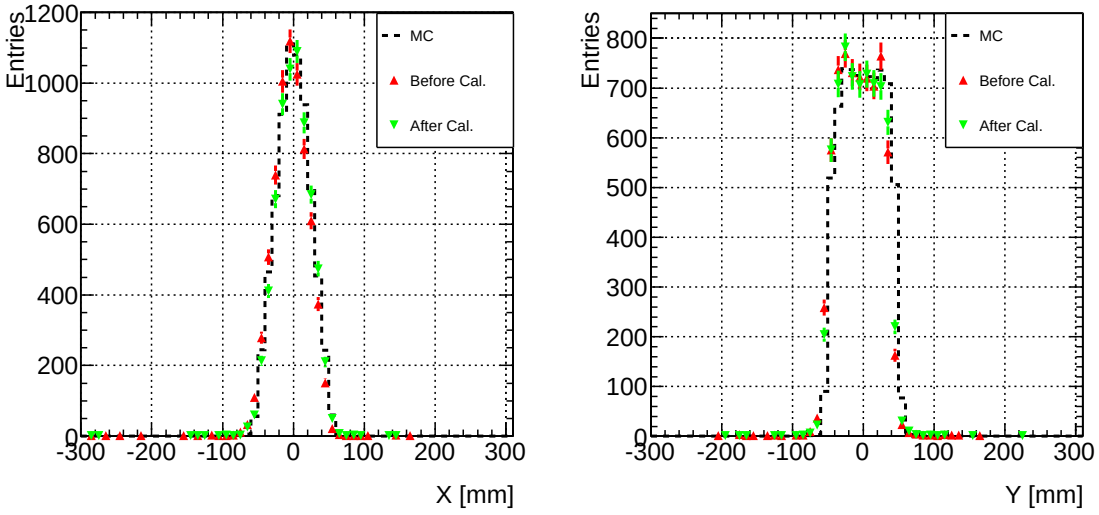

Figure 8.10: Distributions of $x_{c.o.e.}$ (left) and $y_{c.o.e}$ (right). The distribution from the MC (black dashed line), and beam data before (red triangle) and after (green triangle) applying calibration result are shown.

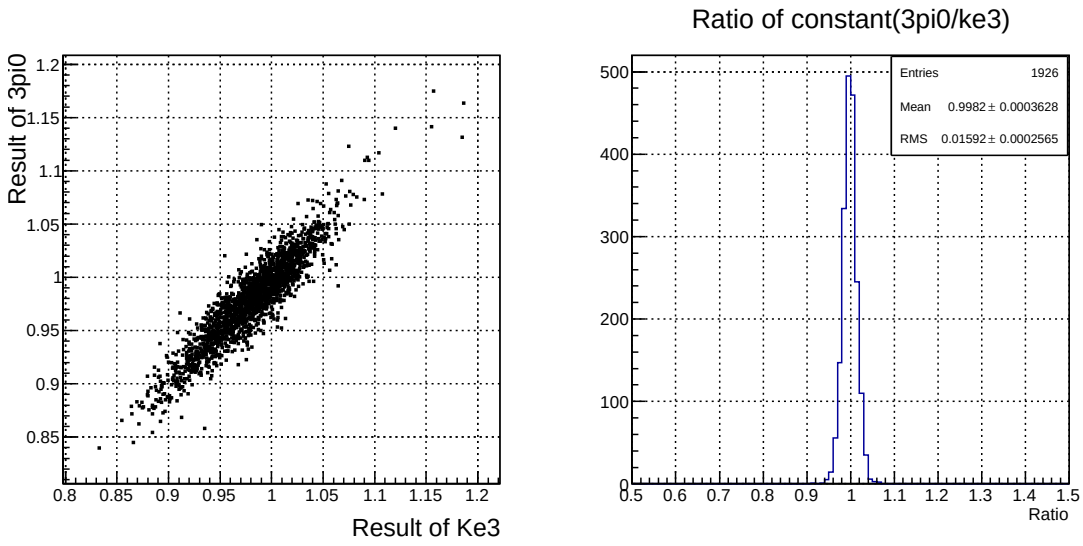

Figure 8.11: Correlation between my calibration result and the Ke3 calibration result [17]. The scatter plot of the results of two calibration methods (left) and their ratio distribution (right) are shown.

Chapter 9

Conclusion

The KOTO experiment at J-PARC aims to observe the $K_L \to \pi^0\nu\bar{\nu}$ decay. To achieve and keep the performance for measuring gamma energy and position, an accurate monitoring system and calibration method are required.

For those requirements, I built a system to monitor temperatures and PMT output of the CsI calorimeter, and I confirmed that they worked properly as required. For the calibration method, I tested the three calibration methods, the initial calibration, $3\pi^0$ calibration, and energy scale calibration. For the initial calibration method using cosmic ray, its calibration precision was determined to 3%. I showed that the result of the initial calibration depends on the module position and size. In the $3\pi^0$ calibration method, I determined its performance and features. I showed that its calibration accuracy is related to the number of $K_L \to 3\pi^0$ decay events, and the calibration accuracy achieved less than 1% with 2×10^{10} K_Ls in the KL beam. With the energy scale calibration using π^0s produced in an Al target in the KL beam, the energy scale was corrected. The calibration result agreed with the Ke3 calibration result less than 0.2% in mean value, and 1.6% in width. With the result, I confirmed the energy scale calibration was properly done.

I also developed a nonlinearity correction method using the $3\pi^0$ calibration method. I showed that the dependence of the reconstructed π^0 mass on the pulse height reduced by applying the nonlinearity reconstruction result on the data. With this method, the nonlinearity can be monitored during physics data taking. These results shows that the calorimeter can be calibrated with its own data including the nonlinearity without other detectors.

I proved that the calibration constant of each channel can be monitored with an accuracy of less than 1% during a long data taking period with the calibration method and monitoring systems. It guarantees that the performance of the calorimeter can keep its performance during several years of data taking.

Appendices

Appendix A

Ke3 calibration

For the performance test of the calorimeter, the spectrometer was set upstream of the calorimeter. The spectrometer consisted of 4 planes of wire tracking chambers and a dipole magnet.

The $K_L \to \pi^{\pm} e^{\mp} \nu_e$ decay events were used for the test. The spectrometer measures the momentum of charged particles from the $K_L \to \pi^{\pm} e^{\mp} \nu_e$ decay event. The momentum is compared with the measured energy by the calorimeter. In case of electron, the ratio between the momentum and energy, E_e/p_e,should be 1, and for other particles, pions and muons, the ratio should not be 1.

The electron events were selected, the calibration constant of each module was derived by χ^2 minimization. The momentum of electrons was can be considered as the true energy of electron, E_{true}. Then the χ^2 can be written as:

$$\chi^2 = \sum_{i}^{All\ event} \frac{(E^i_{cal} - E^i_{true})^2}{\sigma^2_E}. \tag{A.1}$$

Here, i is event index, E^i_{cal} is the energy measured by the calorimeter, and σ_E is energy resolution at the E^i_{cal}. The E^i_{true} and E^i_{cal} can be written with the inverse of calibration constants, $\mathbf{c}(= \mathbf{e}/\mathbf{e}^0)$, measured energy deposit of modules, $\mathbf{e}$, and true energy deposit of modules, $\mathbf{e}^0$.

$$E_{true} = \beta \sum_j e^0_j, \tag{A.2}$$

and

$$E_{cal} = \beta \sum_j e^0_j c_j = \beta \sum_j e_j. \tag{A.3}$$

Here, j is the module index of the cluster member, and β is energy conversion constant which is derived from the energy correction function, Eq. 5.5. Hereafter, the event index, i, is omitted.

The χ^2 is minimized where the its partial derivative of calibration constants meets the condition,

$$\frac{\partial \chi^2}{\partial c_j} = 2 \times \sum_{i}^{All\ event} \frac{e_j \sum_k c_k e_k - e_j E_{true}}{{\sigma_E}^2} = 0. \tag{A.4}$$

Then, it can be expressed as matrix form with definition,

$$D_{jk} = \sum_{i}^{All\ event} \frac{e_j e_k}{\sigma^2_E}, \tag{A.5}$$

and

$$E_j = \sum_{i}^{All\ event} \frac{e_j E_{true}}{\sigma_{E^2}}, \tag{A.6}$$

as:

$$\sum_{k} D_{jk} c_k = E_j, or\ D\mathbf{c} = \mathbf{E} \tag{A.7}$$

The $\mathbf{c}$ is derived as:

$$\mathbf{c} = D^{-1}\mathbf{E}. \tag{A.8}$$

The inverse of $\mathbf{c}$ are set as the calibration constant.

Bibliography

[1] G.C Branco, lecture note, http://gravitation.web.ua.pt/cosmo .

[2] A. D. Sakharov, Pisma Zh. Eksp. Teor. Fiz. 5, 32 (1967).

[3] J.H. Christenson, J.W.Cronin, V.L.Fitch and R. Turlay, Phys. Rev.Lett.13, 138-140 (1964).

[4] L. Wolfenstein (1983), "Parametrization of the Kobayashi-Maskawa Matrix", Physical Review Letters 51 (21): 1945.

[5] J. Beringer et al. (Particle Data Group), Phys. Rev. D86, 010001 (2012).

[6] Joachim Brod et al. Two-loop electroweak corrections for the $K \to \pi\nu\bar{\nu}$ decays. Phys. Rev. D, 83:034030, Feb 2011.arXiv:1009.0947v2 [hep-ph].

[7] J. Comfort et al. Proposal for $K_L \to \pi^0\nu\bar{\nu}$ Experiment at J-Parc.

[8] J. K. Ahn et al. Experimental study of the decay $K_L \to \pi^0\nu\bar{\nu}$.

[9] David M. Straub, New physics correlations in rare decays, arXiv:1012.3893v2 [hep-ph].

[10] E787/E949, Phys.Rev.Lett.101, 191082.

[11] Y.Grossman and Y.Nir, Phys. Lett. B398, 163 (1997).

[12] J-PARC. http://j-parc.jp/Acc/en/layoutE.html .

[13] Rihua Mao, Liyuan Zhang and Ren-Yuan Zhu, IEEE TRANSACTIONS ON NUCLEAR SCIENCE, VOL. 55, NO. 4, AUGUST (2008).

[14] Paul Avery, Fitting Theory [I - VII], web page : www.phys.ufl.edu/ avery/fitting.html

[15] K. Shiomi, Ph.D. thesis (Kyoto University, Jan, 2012).

[16] E. Iwai, Ph.D. thesis (Osaka University, Apr. 2012).

[17] K. Sato, from his analysis result.

[18] A study of E.Iwai for correction gamma energy.